

Modelling laser percussion drilling

Citation for published version (APA):

Verhoeven, J. C. J. (2004). *Modelling laser percussion drilling*. [Phd Thesis 1 (Research TU/e / Graduation TU/e), Mathematics and Computer Science]. Technische Universiteit Eindhoven.
<https://doi.org/10.6100/IR580582>

DOI:

[10.6100/IR580582](https://doi.org/10.6100/IR580582)

Document status and date:

Published: 01/01/2004

Document Version:

Publisher's PDF, also known as Version of Record (includes final page, issue and volume numbers)

Please check the document version of this publication:

- A submitted manuscript is the version of the article upon submission and before peer-review. There can be important differences between the submitted version and the official published version of record. People interested in the research are advised to contact the author for the final version of the publication, or visit the DOI to the publisher's website.
- The final author version and the galley proof are versions of the publication after peer review.
- The final published version features the final layout of the paper including the volume, issue and page numbers.

[Link to publication](#)

General rights

Copyright and moral rights for the publications made accessible in the public portal are retained by the authors and/or other copyright owners and it is a condition of accessing publications that users recognise and abide by the legal requirements associated with these rights.

- Users may download and print one copy of any publication from the public portal for the purpose of private study or research.
- You may not further distribute the material or use it for any profit-making activity or commercial gain
- You may freely distribute the URL identifying the publication in the public portal.

If the publication is distributed under the terms of Article 25fa of the Dutch Copyright Act, indicated by the "Taverne" license above, please follow below link for the End User Agreement:

www.tue.nl/taverne

Take down policy

If you believe that this document breaches copyright please contact us at:

openaccess@tue.nl

providing details and we will investigate your claim.

Modelling Laser Percussion Drilling

Kees Verhoeven

Copyright ©2004 by Kees Verhoeven, Bladel, The Netherlands.

All rights are reserved. No part of this publication may be reproduced, stored in a retrieval system, or transmitted, in any form or by any means, electronic, mechanical, photocopying, recording or otherwise, without prior permission of the author.

This research was supported by Eldim B.V. and Rolls Royce plc.

Printed by Eindhoven University Press

CIP-DATA LIBRARY TECHNISCHE UNIVERSITEIT EINDHOVEN

Verhoeven, J.C.J.

Modelling laser percussion drilling /
by Jan Cornelis Johannes Verhoeven -
Eindhoven : Technische Universiteit Eindhoven, 2004. Proefschrift. -
ISBN 90-386-0942-6

NUR 919

Subject headings: mathematical models / numerical heat transfer / drilling
2000 Mathematics Subject Classification: 65Z05, 80A22, 35R35, 65M60, 76T10

Modelling Laser Percussion Drilling

PROEFSCHRIFT

ter verkrijging van de graad van doctor aan de
Technische Universiteit Eindhoven, op gezag van de
Rector Magnificus, prof.dr. R.A. van Santen, voor een
commissie aangewezen door het College
voor Promoties in het openbaar te verdedigen
op donderdag 4 november 2004 om 16.00 uur

door

Jan Cornelis Johannes Verhoeven

geboren te Eindhoven

Dit proefschrift is goedgekeurd door de promotoren:

prof.dr. R.M.M. Mattheij

en

prof.dr. M. Rumpf

Copromotor:

dr. J.M.L. Maubach

Nomenclature

Vectors are printed boldface, e.g. \mathbf{n} , tensors and matrices are denoted boldface (\mathbf{B}) as well. Furthermore we use grad as well as ∇ for the gradient, and div as well as $\nabla \cdot$ for the divergence.

Constants

ρ	density
c	specific heat capacity
k	thermal conductivity
L_f	latent heat of fusion
L_v	latent heat of vaporisation
λ	wave length
w	waist of a laser beam

Variables

H	enthalpy
I	intensity
T	temperature
θ	dimensionless temperature
η	dimensionless enthalpy

Subscripts

0	initial or leading order
a	ambient
b	boundary
f	fusion
i	incident
l	liquid
liq	liquidus
m	melting
r	reflected
s	solid
t	refracted
sol	solidus
v	vaporisation
ref	reference

Abbreviations

ARTM	Algebraic Ray Trace Method
DOM	Discrete Ordinate Method
EBD	Electron Beam Drilling
ECD	Electro Chemical Drilling
EDM	Electric Discharge Machining
FEM	Finite Element Method
TIT	Turbine Inlet Temperature

Contents

Nomenclature	v
1 Introduction	1
1.1 Background	1
1.2 Laser drilling	4
1.3 Problem setting	7
1.4 Outline of the thesis	9
2 The global model	11
2.1 Introduction	11
2.2 The laser	13
2.3 Melting	15
2.4 Gas Dynamics	17
2.5 Splashing and solidification	22
2.5.1 Parameter régimes	23
2.5.2 Planar solidification	25
2.5.3 Axisymmetric splashing model	27
3 Laser induced melting	31
3.1 Modelling melting	31
3.1.1 The Stefan Problem	32
3.1.2 The Enthalpy Problem	33
3.2 Numerical methods for melting	35
3.2.1 Discretisation of the Stefan Problem	35

3.2.2	Finding suitable initial conditions	39
3.2.3	Discretisation of the Enthalpy Problem	41
3.3	Extension to 2D	43
3.4	Numerical results and discussion	46
4	The effect of the laser beam	51
4.1	Reflections of the incoming beam	51
4.1.1	Background	52
4.1.2	Computational method	56
4.1.3	Results	61
4.2	Wavelength and peak intensity	64
4.3	Spatial pulse shape	66
4.4	Temporal pulse shape	70
4.5	Simulation	71
5	Splashing and solidification	75
5.1	Axisymmetric splashing model	75
5.2	Planar solidification model	79
5.3	Numerical methods for solidification	80
5.3.1	Shocks	82
5.3.2	Enthalpy Method	82
5.3.3	Numerical Method	83
6	Computational platforms	93
6.1	Scientific computing	93
6.2	Example	97
7	Conclusions and Recommendations	101
	Bibliography	105
	Index	109
	Summary	111

Contents

ix

Samenvatting 113

Acknowledgements 115

Curriculum vitae 117

Introduction

1.1 Background

In the gas turbine industry there is ongoing research into making 'better' turbines, resulting in more efficient, safer, more environmentally friendly and more silent engines. Figure 1.1 shows an aero-engine. In Figure 1.2 a schematic overview of such

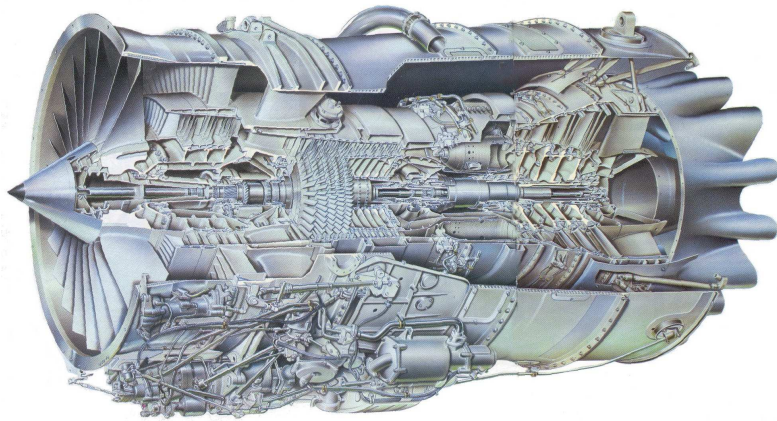
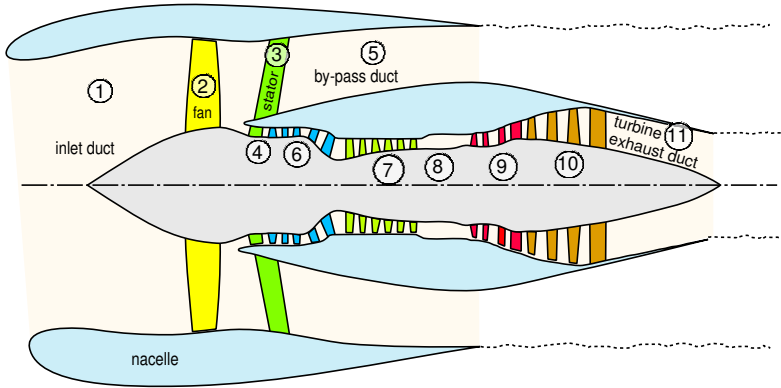


Figure 1.1: *Cross section of a Rolls-Royce Tay aero-engine.*

an aero-engine is depicted. The airfoils at the left are called the *fans*. Air is accelerated by these fans after which it is partly led through the by pass duct and partly into the compressor stages. In this compressor, air is compressed going from the low pressure to the high pressure stage. The compressed air is led into the combustion chamber. The hot air leaving the combustion chamber is led through the turbines, from the high pressure part to the low pressure part.

For thermodynamical reasons the efficiency of a turbine can be greatly enhanced by



- | | | |
|---------------------------|------------------------------|---------------------------|
| 1 = inlet duct | 5 = bypass duct | 9 = high-pressure turbine |
| 2 = fan rotor | 6 = low-pressure compressor | 10 = low-pressure turbine |
| 3 = outlet guide vanes | 7 = high-pressure compressor | 11 = turbine exhaust duct |
| 4 = engine section stator | 8 = combustion chamber | |

Figure 1.2: Schematic overview of an aero-engine.

increasing the temperature in the combustion chamber and the first high pressure turbine stages. Combustion chamber temperatures have increased up to 1600°C over the past decade. This means that the gas turbine components have to cope with these extreme conditions. Figure 1.3 shows the result of what an aero-engine manufacturer wants to avoid: damage through overheating, in this case in overheated turbine blades.

In the development of turbine blades (which rotate) and vanes (which are static) capable of dealing with increasing Turbine Inlet Temperature (TIT) three methods were used. The first is concerned with the material the airfoils are made of and how they are casted. A first aspect is that the airfoils material has resulted in better mechanical and heat resistance properties. Furthermore, better casting techniques made the blades stronger with respect to both mechanical and heat resistance sense. This led from (i) the conventionally cast turbine blade, with good mechanical properties in all directions and an equi-axed crystal structure, via (ii) the directionally solidified turbine blade, with improved mechanical properties in the longitudinal axis and a columnar crystal structure, to (iii) the single crystal turbine blade, with excellent mechanical properties in longitudinal axis and improved heat resistance. A second technique to be able to increase the thermal load on the turbine blades and vanes without damaging them is to cover the airfoil with a coating which creates a sort of thermal barrier. The third method used is to cool the blades. This cooling is done both internally and through film cooling. In both techniques relatively cold air takes care of the cooling. In the sixties the blades were cooled only internally through either drilled longitudinal holes or through cavities created during the casting procedure. Because the TIT increased ever further, this internal cooling technique was

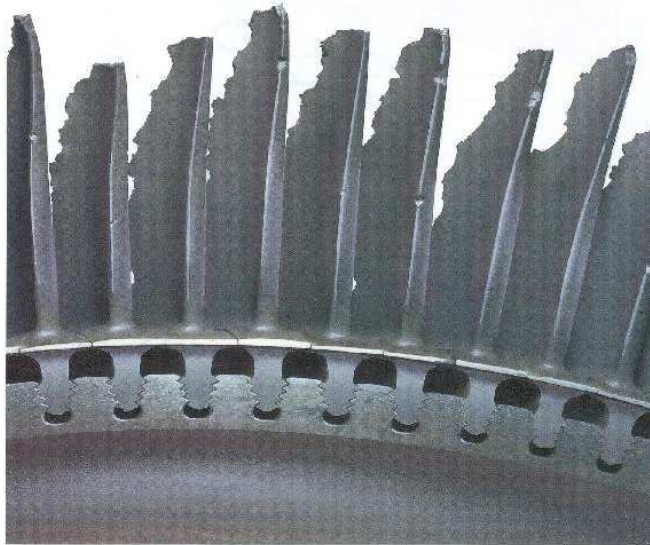


Figure 1.3: *Overheated turbine blades.*

not sufficient. In the seventies film cooling was introduced on top of the internal cooling. In film cooling, air flowing through holes drilled from the exterior to the interior cavities creates a cold air film layer across the surface of the blades. This film layer prevents the hot combustion gases to get into direct contact with the blade. Nowadays this film cooling is used, together with improved internal cooling. This development in turbine blade cooling techniques is shown in Figure 1.4.

Usually the cooling holes are produced by some form of drilling. There are several techniques to drill these holes in metal, the biggest drawback of most of them being the speed of the process. Mechanical drilling is not suited for superalloys; mechanical punching is fast but is limited to holes with a diameter larger than 3mm. Electro Chemical Drilling (ECD) is also slow and, as a side effect, produces a lot of waste, however, it does give neat holes. The procedure of ECD has been modelled in [30]. Electric Discharge Machining (EDM), or spark erosion, is also slow and cannot be used for coated materials. ECD and EDM have typically drilling speeds of 1–10 mm/min, but several holes can be drilled at the same time, using multiple electrodes. Electron Beam Drilling (EBD) is fast, but needs a vacuum chamber. Holes can also be drilled using a laser, which is of great potential because it delivers its energy in a contactless and concentrated way, thereby drilling fast, typically 1–10 mm/sec.

To increase the TIT several parts have to be cooled and, as mentioned, one way to achieve this is to drill cooling holes in the components. There are roughly four groups of components that need to be provided with cooling holes. These are the blades, the vanes, the inserts and the combustion chambers. In blades, approximately 300 film cooling holes per blade need to be drilled, both of cylindrical and of fan

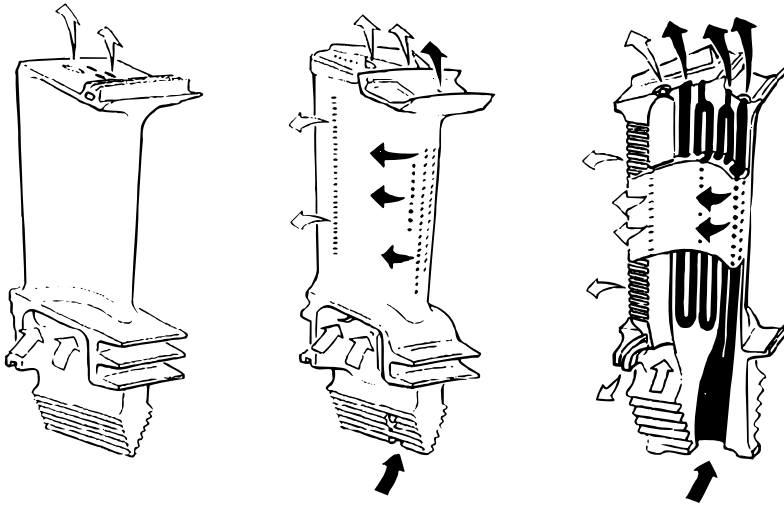


Figure 1.4: *Development of turbine blade cooling. In the 1960's only single pass internal cooling (left), in the 1970's both single pass and multi-feed internal cooling together with film cooling (middle). Nowadays, quintuple pass and multi-feed internal cooling together with extensive film cooling (right). The filled arrows denote the flow of high pressure cooling air, the others of low pressure cooling air.*

shaped form. The diameter of these holes ranges from 0.5 to 1.0 mm and their depths vary between 3 and 10 mm. For the cylindrical holes a laser is often used, whereas for the fan shaped holes EDM is better suited. For the vanes, the same more or less holds. Approximately 500 holes per part need to be drilled, both cylindrical and fan shaped. Again the laser is favoured for the cylindrical holes and EDM for the fan shaped ones. In the inserts on average around 300 holes need to be drilled. The holes are cylindrical, 0.3 – 3 mm in diameter. For these parts a laser gives the best results. For the drilling of holes in the combustion chambers, where more than 100,000 holes per part need to be drilled, drilling speed is essential. The diameter of the holes varies from 0.3 – 3 mm and the depth from 6 – 20 mm. As one can see, laser drilling can be used extensively for drilling cooling holes in gas turbine components. The actual laser drilling techniques will be outlined in the next section, with special focus on laser percussion drilling.

1.2 Laser drilling

Since the first demonstrations of a ruby laser by Theodore Maiman in 1960, the laser has always fascinated people. In its short life the laser has gained a popular image that has more in common with science fiction than science. In fact, lasers have become very important and commonplace tools. Lasers are nowadays applied in a variety of fields, from reading bar codes at the local supermarket and CD-ROMs to eye surgery applications. The main reason for its success is that the laser delivers

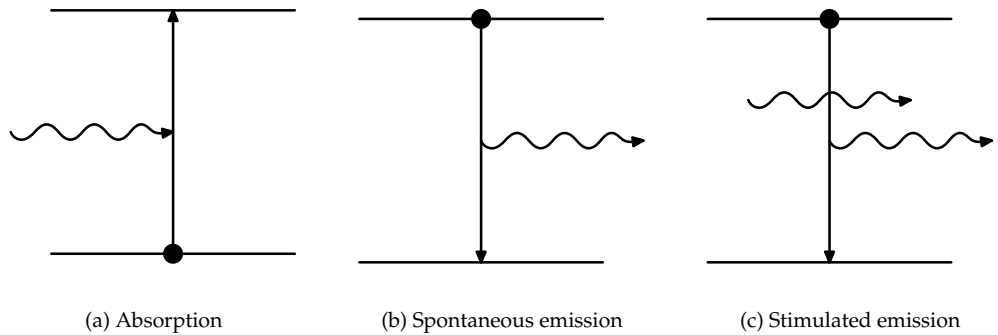


Figure 1.5: *Absorption and emission processes between two energy levels.*

concentrated energy, where, when and in any desired quantity and furthermore, it does so in a contactless and pure way. Because of this significant industrial potential of the laser, it rapidly found its way into the field of processing materials through an immense and still expanding number of applications. In the case of metals, the applications are for instance surface hardening, welding, cutting and drilling.

Let us explain the working of a laser briefly. The basic laser consists of two mirrors which are placed in parallel to each other to form an optical resonator, that is a chamber in which light would oscillate back and forth between the mirrors forever, if not prevented by some mechanism such as absorption. One of the two mirrors is partially transparent to allow some of the oscillating power to emerge as the operating beam. The other mirror is totally reflecting. Between the mirrors an active medium resides which is capable of amplifying the light oscillations by the mechanism of stimulated emission (the process after which the laser is named - **L**ight **A**mplification by **S**timulated **E**mission of **R**adiation). When an atom in its “ground” state absorbs a photon, it is excited, or raised to a higher energy state (Fig. 1.5(a)). The excited atom may then radiate energy spontaneously, emitting a photon and reverting to its ground state (Fig. 1.5(b)). An excited atom can also be stimulated to emit a photon when it is struck by an outside photon reverting it to its ground state again (Fig. 1.5(c)). Thus in addition to the stimulating photon there is now a second photon of the same wavelength, thereby amplifying the radiation. The laser system can only operate if it has enough energy to become active and therefore needs a pumping mechanism. There are several techniques to pump the active medium. A DC or RF power supply is used in for instance CO₂ and He/Ne lasers. A focussed pulse of light was used in the first ruby laser and is used in for example the Nd:YAG lasers. A schematic diagram of a laser is given in Figure 1.6.

When laser light, which is an electromagnetic wave, is incident on a metal surface, electrons within the metal are driven into harmonic oscillation by this harmonic wave. These conduction electrons undergo collisions with the thermally agitated lattice or with imperfections and in doing so irreversibly convert electromagnetic energy into joule heat. Evidently, the absorption of radiant energy by a material is a

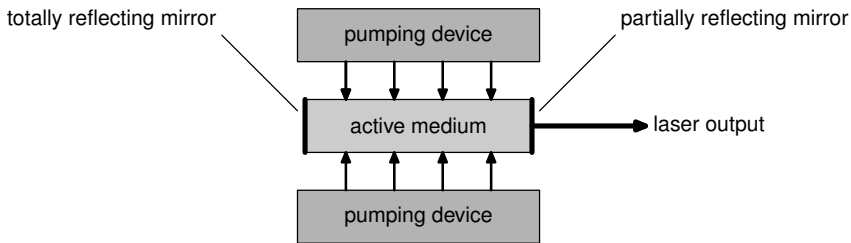


Figure 1.6: A schematic diagram of a laser.

function of its conductivity.

In laser drilling the laser must be reasonably powerfull and this reduces the number to only a few lasers currently, essentially the CO_2 , the Nd:YAG of Nd-glass and the excimer lasers, see e.g. [39].

There are roughly three techniques to drill with a laser. The simplest way is to remove material through a single laser pulse. This technique is mainly used for drilling narrow (< 1 mm) holes through thin (< 1 mm) plates. Another method, used to drill wider (< 3 mm) holes in plates (< 10 mm), is to cut a contour out of the plate. This technique is called *laser trepanning drilling*. The drilling process in which the laser op-

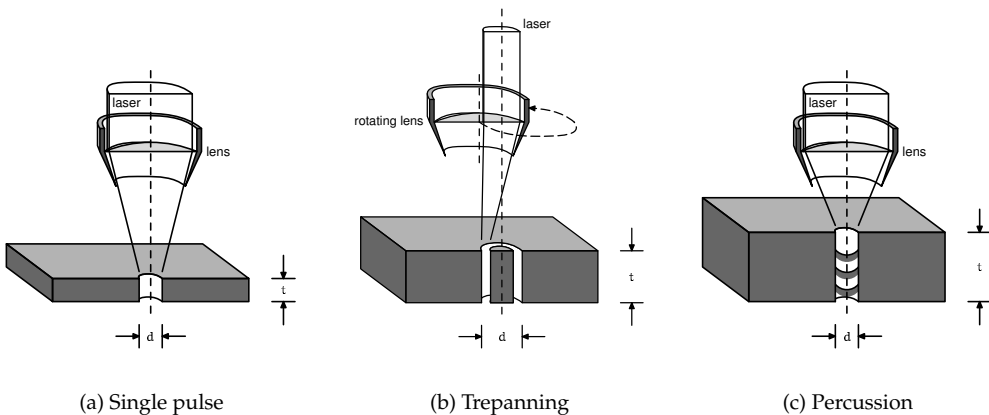


Figure 1.7: Laser drilling methods. For single pulses the drilling depths t are limited to 3 mm, for trepanning to 10 mm. For percussion drilling, holes up to 20 mm deep can be drilled. The diameter d of the holes drilled is typically 1 mm for single pulse and percussion drilling and 0.5 – 3 mm for trepanning.

erates in a repeated manner, with short pulses, ranging from 10^{-12} to 10^{-3} s, which are separated by longer time periods, is called *laser percussion drilling*. In this way the laser builds up energy and operation in this manner allows for large bursts of energy.

With this technique narrow (< 1 mm) holes up to 20 mm deep can be drilled. The three techniques of laser drilling are depicted schematically in Figure 1.7. Figure 1.8 shows a laser trepanning drilling process in action.



Figure 1.8: A photograph of a laser drilling process. (Courtesy Eldim B.V.)

1.3 Problem setting

Laser percussion drilling is favoured over the older drilling techniques and the other laser drilling techniques because it is by far the quickest. However, it still suffers from some drawbacks. The first drawback is that a so called *recast layer*, that is, resolidified material remains at the wall of the hole. Some resolidified material can normally also be found at the entrance and exit of the hole, in which cases it is called *spatter* and *dross*, respectively. Furthermore, the holes normally show some *tapering*: the decrease of hole diameter with depth. Nowadays, one does not necessarily see this tapering as a disadvantage any more, however, control of the taper angle and reproducibility is needed. Finally, occasionally the hole resulting from a laser percussion drilling process shows *barreling* or a *bellow shape*; the local increase of hole diameter. These terms are illustrated in Figure 1.9.

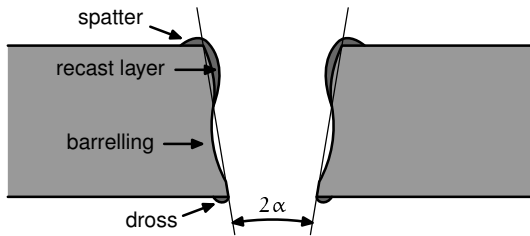


Figure 1.9: Explanation of terms for the results of a laser percussion drilling process. The taper angle is given by α .

A series of photographs of holes machined by laser percussion drilling can be seen in Figure 1.10. The number denotes the number of pulses used to create the particular hole. The growth rate of the hole is initially linear with the number of pulses but slows down in later photographs. The eleventh hole appears not to be as deep as the tenth, because melt has resolidified at the bottom. We note that from the seventh photograph on, one can see the recast layer at the walls of the hole. This resolidification may be in the form of very thin layers or clumps, the latter form can be seen in the eleventh photograph. In the last three photographs molten metal may have escaped via the bottom exit.

It is because of the drawbacks mentioned and illustrated above that many tests have to be performed to find the optimal settings for the laser to produce the desired hole. If a simulation model can be used this would have two huge benefits. First: it would save a lot of costs because the number of tests on expensive material can be brought down tremendously. Secondly, within a simulation model one is not limited to practical issues such as for instance wave length or power limitations. This means that one can try to find the 'ideal' laser and settings to drill a particular hole. Furthermore, in the process of modelling a deep insight is gained with respect to what the key variables in the process are.

In laser percussion drilling the metal is removed by a combination of evaporation and melt ejection. The latter mechanism is by far the most important one, the mass fraction extracted by vaporisation is typically one tenth of the total mass loss [1, p. 133]. Furthermore, it is by far the most efficient one, as evaporation is much more 'expensive' than melting. However, the melting is also the reason for the resolidification, the main drawback of laser drilling. Evidently, in order to thoroughly model laser percussion drilling, the modelling of phase changes, as well in laser induced melting as in resolidification, is essential. In laser drilling in metals, it turns out that the actual input of energy at the surface of the material can be considerably different than expected from the output of the laser. This is due to reflections of the incoming laser beam of the walls of the hole. Therefore the modelling of reflections is also essential to be able to predict the outcome of a laser percussion drilling process.

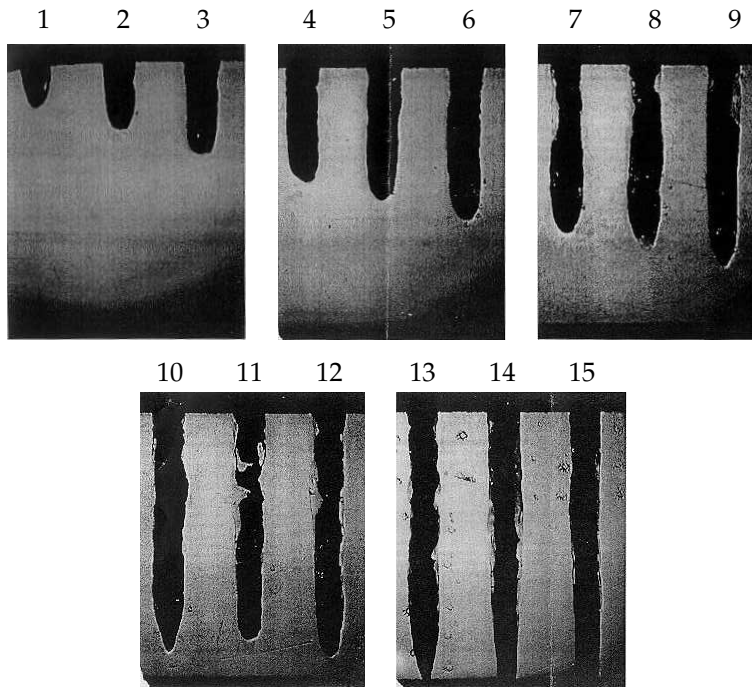


Figure 1.10: *A series of photos of holes produced by laser percussion drilling. The number of pulses to produce each hole is indicated. (Courtesy of ELDIM BV)*

1.4 Outline of the thesis

In laser percussion drilling, several physical phenomenae play a role. All these phenomenae will be studied in Chapter 2. After a short introduction describing the different stages of a laser percussion drilling process in Section 2.1, more detailed information about lasers used in practice is given. Sections 2.3–2.5 then deal with the heat flow problems, (i) the melting, (ii) the gas dynamics, being the driving force for (iii) the splashing and solidification. Laser induced melting is described mathematically and it is shown that a one-dimensional model is adequate. The gas dynamics is modelled in Section 2.4 resulting in a system of equations, which, given the material and beam properties, gives an estimate for the recoil pressure. This recoil pressure is the driving force for the splashing and solidification; these two phenomenae are described mathematically in Section 2.5.

Having treated the basic equations in Chapter 2, it is time to zoom in onto the various subproblems. In Chapter 3 we study the laser induced melting, that is we formulate and solve phase change occurring in the material under influence of the incoming laser energy. We extensively investigate the two ways to formulate the phase change, the Stefan problem, which treats the phase change interface as a moving boundary, and the enthalpy problem, which makes use of this physical quantity to simplify the

equations. These two methods are assessed and numerical solving techniques are derived. Although Chapter 2 shows that a one-dimensional model is sufficient for laser induced melting, some attention will be paid in Section 3.3 to the extension of the two formulations to 2D, because the splashing and solidification models, in which phase change occurs as well, do have essentially two spatial dimensions. The results obtained following the numerical procedures as outlined in Section 3.2 are presented and assessed in Section 3.4.

In Chapter 4 the laser comes into the picture again. Section 4.1 deals with the reflections of the incoming beam, which are extremely important to the result of the process. In fact, due to reflections, the actual irradiation distribution at the surface of the material can differ a lot from the distribution supplied by the laser.

In Section 4.1.1 the equations describing the reflection of an electromagnetic wave on a metal are summarized. The procedure to find the actual distribution of irradiation on the metal surface after multiple reflections is outlined in Section 4.1.2. Results obtained following this procedure are presented in Section 4.1.3 and here the need to incorporate a reflection model becomes obvious. Sections 4.2 to 4.4 subsequently deal with the implications the laser beam itself has on the resulting holes. The effects the wave length and peak intensity the laser supplies as well as its temporal and spatial pulse shapes have on the results of the drilling process are studied. The advantage modelling has in this respect is that the mathematical system is not restricted to practical issues. One can freely experiment with changing wavelength, peak intensities, spatial and temporal irradiation distributions without bothering about whether or not these are possible in the state of the art equipment. This aspect shows a huge power of mathematical modelling. One can actually try to find the 'ideal' laser for laser percussion drilling. A complete simulation of a typical laser percussion drilling process is carried out in Section 4.5.

The equations describing splashing and solidification as derived in Chapter 2, are subject of study in Chapter 5. An asymptotic analysis of these equations yields first-order models for axisymmetric splashing and planar solidification in Sections 5.1 and 5.2, respectively. A numerical solution procedure for the solidification model is then outlined in Section 5.3. Within this numerical procedure several techniques are employed. Finite element techniques are used to obtain temperature and enthalpy distributions in both the solid and the liquid and as a result of this the position of the solid-liquid interface is obtained. Coupled with this the movement of the liquid blob follows from equations which are solved by means of slope limiter schemes.

Chapter 6 discusses the computational platform on which the simulation model is based. Section 6.1 shows the benefits a visual programming environment has over non-graphical ones. Furthermore, by adorning existing libraries with a standard interface these can easily be used within a broader framework. The construction of such an interface is outlined in Section 6.2. Finally, in Chapter 7 we give a short overview of findings made in this thesis. Furthermore, some recommendations are made to further enhance the model.

The global model

This chapter is concerned with the modelling issues of the laser percussion drilling process. The process will first be studied from a phenomenological, that is physical, viewpoint in Section 2.1. The next sections deal with the key phenomena: the laser itself, melting, vaporisation, splashing and solidification. In Section 2.2 several different aspects of the laser will be studied. Section 2.3 will look closer at melting, Section 2.4 at the gas dynamics and the last section in this chapter will focus on modelling of splashing and solidification.

2.1 Introduction

Lasers are often used to machine materials when conventional techniques fail. Laser percussion drilling is one of these applications. For instance, this drilling technique is used to drill cooling holes in gas turbine components, which are typically made of super alloys. The term “percussion” refers to the repeated operation of the laser in short pulses (10^{-3} s), which are separated by longer time periods (10^{-2} s). The energy supplied by the laser is bounded, and pulsewise behaviour allows for large bursts of energy. We return to the laser and the laser beam in the next section.

The actual drilling consists of two material removal mechanisms: removal by evaporation and removal by melt ejection. The second mechanism has to be explained further. Because of the vapour pressure (commonly referred to as the *recoil pressure*), the vapour is pushed away from the surface. At the same time, this recoil pressure exerts a force on the melt pool and this melt is being squirted out. These two mechanisms are sketched in Figure 2.1.

Experiments show, see e.g. [1], that using the laser percussion drilling technique in the intensity régimes used at Eldim BV and Rolls Royce plc., most of the material removed is liquid. The energy needed to liquify the material is far less than the energy

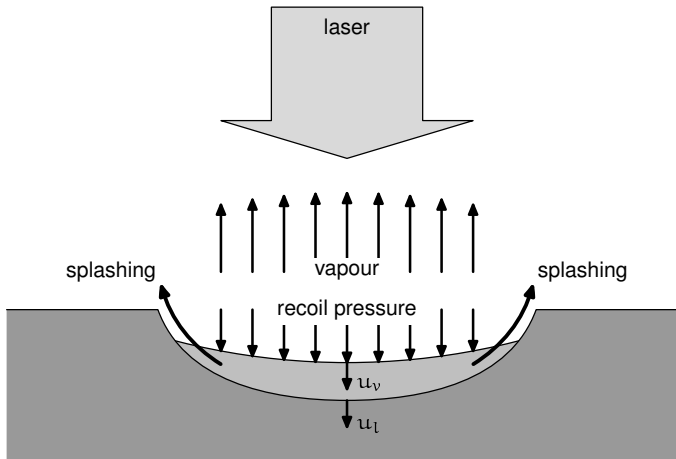


Figure 2.1: Schematic diagram of the material removal mechanisms in laser drilling.

needed to vaporise it and, therefore, this melt ejection is an efficient mechanism to remove material. However, melt ejection also suffers from the important drawback of depositing a resolidified layer, the so called *recast layer*, at the walls of the hole.

A laser percussion drilling process may in fact be split up into three stages. Initially, a thin region of molten material is formed by absorption of laser energy at the target surface. After some time, the surface of this melt pool reaches vaporisation temperature. The sudden expansion of the vapour evaporating from the surface leads to the final stage: the melt pool is being pushed out by the recoil pressure. On its way out some part of this molten material may resolidify at the walls. Thus, during these three stages three events occur for which a melting model is needed. These events are depicted in Figure 2.2. A simple melting model can be used to predict the precise dimensions of the melt pool, as generated by the incoming radiation, see Fig 2.2(a). In fact, we can show that a one-dimensional melting model applies for the initial stage. The motivations for this as well as the vices and virtues of existing formulations to model this laser induced melting are studied thoroughly in Section 2.3. More sophisticated models are needed to deal with splashing (Fig 2.2(b)) and with solidification (Fig 2.2(c)). These models will be introduced in Section 2.5.

The physics suggest that the process per pulse behaves in a cyclic manner. That is, the material is heated up due to the laser irradiation. The surface reaches melting temperature and a melt pool starts to form. At a certain moment, the surface of this melt pool reaches vaporisation temperature. A splash occurs in which the molten material is pushed out radially by the pressure gradients caused by the sudden expansion of the vapour evaporating from the surface. The solid metal left exposed after the splash now starts to absorb laser energy and so on. Based upon different parameters, a typical number of cycles per pulse can be determined. As will become clear in subsequent sections, for different materials, the time scales for these three stages are between 10^{-5} s and 10^{-4} s for melting and between 10^{-6} s and 10^{-5} s for

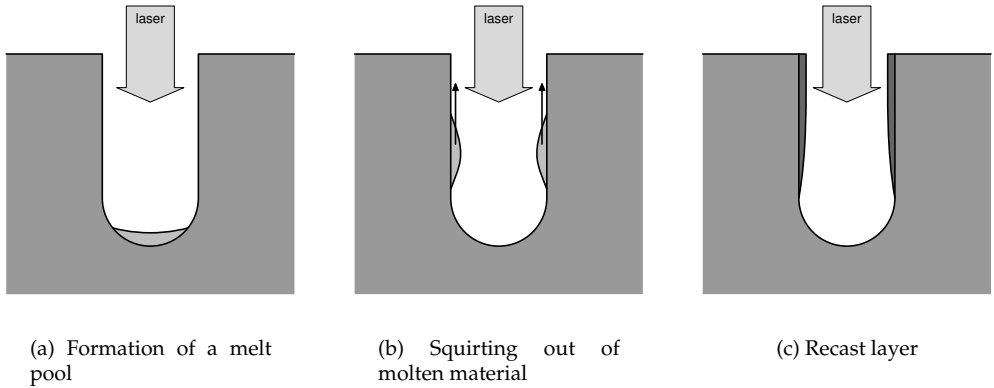


Figure 2.2: The three stages in a laser percussion drilling process: (a) melting, (b) splashing and (c) resolidification.

splashing and solidification. The gas dynamics are assumed to be instantaneous or at least on a much smaller time scale than the other processes. We therefore expect between 10 and 100 splashes within a millisecond pulse.

2.2 The laser

The laser used is of big importance to the process. Those who want to know more about the basics of the laser are referred to [40]. The specifications of the laser used at Eldim B.V. are the following. The laser used is a Nd:YAG (Neodymium in a Yttrium Aluminium Garnet crystal) laser which emits light at a wavelength of 1064 nm. The laser operates at an average power P_{av} [W], and emits its energy in sinusoidal pulses as shown schematically in Figure 2.3. The pulse length t_p is in the order of 1–4 msec and the total amount of energy per pulse is given by E_p [J]. From this we can obtain a lower bound for the *relaxation time* t_r as follows:

$$t_r \geq \frac{E_p}{P_{av}} - t_p. \quad (2.1)$$

Ideally, the laser produces a Gaussian beam, also known as the TEM_{00} -mode, see Figure 2.4(a). Although this will not be exactly the case in practice it is a reasonable assumption. As an even better approximation one could use a superposition of the TEM_{00} -mode with higher order modes. This is studied in more detail in [47].

Knowing the *waist* w , i.e. the radius at which the intensity at the surface has dropped by a factor e^{-2} , and the maximum intensity I_{max} , see Figure 2.4(b), the intensity at any point on the surface at any time within a pulse is given by

$$I(r, t) = I_{max} e^{-\frac{2r^2}{w^2}} \sin\left(\frac{\pi t}{t_p}\right). \quad (2.2)$$

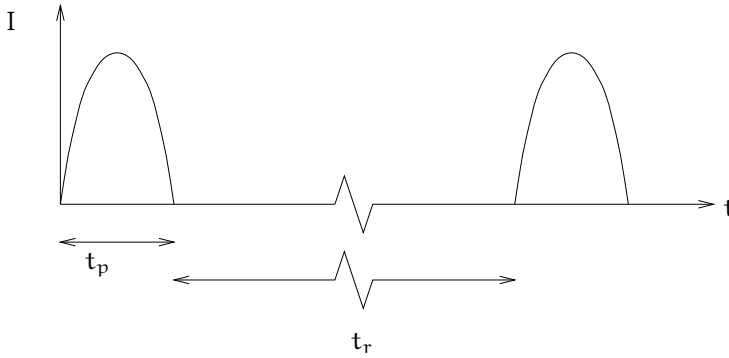


Figure 2.3: The time dependent irradiation distributions of the laser beam. The vertical axis depicts the irradiation whereas the horizontal axis depicts the time. The Nd:YAG used at Eldim operates in sinusoidal pulses.

The constant I_{\max} can, if the waist w is known, be derived from

$$2\pi I_{\max} \int_0^{t_p} \int_0^{\infty} e^{-\frac{2r^2}{w^2}} \sin\left(\frac{\pi t}{t_p}\right) r dr dt = E_p. \quad (2.3)$$

Solving (2.3) for I_{\max} gives

$$I_{\max} = \frac{E_p}{t_p w^2}. \quad (2.4)$$

The waist w of a Gaussian laser beam at the surface can be derived using optics. The laser beam emitted is focussed by a lens with a focal length f (normally 254 mm (i.e., 10")) and the waist of the beam w_0 is given at the lens. A first approximation of the waist at the surface can be obtained using linear optics giving

$$w = \frac{z}{f} w_0, \quad (2.5)$$

where z denotes the distance of the focal point to the surface. A more accurate calculation of the waist at the surface can be done using the principles of Gaussian beam focussing, see [40, Chapter 17]. We note that the *VSM-number*, denoting twice the waist spot size w_0 , of the lens used is known. From this we can derive the waist at the surface. Another important aspect concerning the laser beam is its incidence at the surface. Part of the incident laser light is absorbed at the surface and transformed into heat, the rest is reflected. These reflected rays may again impinge on the surface, where again part is absorbed and so on. In most models, these reflections are completely ignored. We will use a distribution of incident intensities in our model. Thus, we can incorporate reflections easily. The modelling of these reflections and its implications on the process will be studied in Section 4.1.

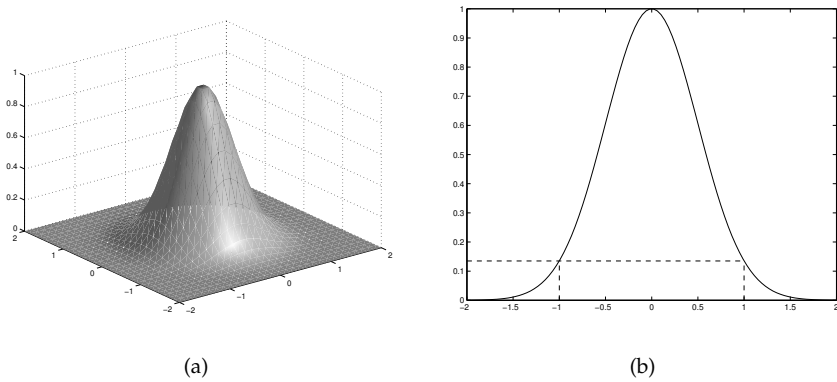


Figure 2.4: The spatial intensity distribution of a Gaussian (TEM_{00}) beam. Figure (a) depicts this distribution and in Figure (b) a cross section is shown to visualise the meaning of the waist w of a beam.

2.3 Melting

The lasers used in practice to drill holes typically produce a Gaussian intensity distribution, which is, ideally, axisymmetric. Moreover, further examination shows that radial diffusion is negligible, which can be seen as follows: take an axi-symmetric coordinate system, where $z = 0$ denotes the surface of the irradiated material, see Figure 2.5. The density ρ , the specific heat capacity c and the thermal conductivity k

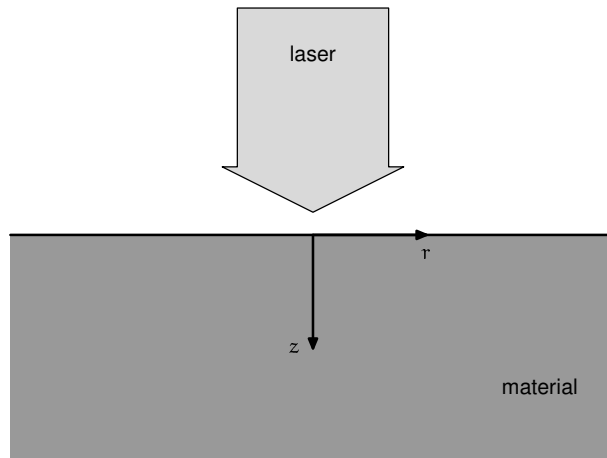


Figure 2.5: Geometry of the model.

of the material are known and assumed to be constant. The temperature T in the material is governed by the heat equation in cylindrical coordinates, which, employing

Symbol	Definition	Value	
		Al	W
ρ	density	$2.7 \times 10^3 \text{ kg m}^{-3}$	$19.3 \times 10^3 \text{ kg m}^{-3}$
L_f	latent heat of fusion	$3.6 \times 10^5 \text{ J kg}^{-1}$	$2.5 \times 10^5 \text{ J kg}^{-1}$
k	thermal conductivity	$2.3 \times 10^2 \text{ W m}^{-1} \text{ K}^{-1}$	$1.5 \times 10^2 \text{ W m}^{-1} \text{ K}^{-1}$
c	specific heat capacity	$9.0 \times 10^2 \text{ J kg}^{-1} \text{ K}^{-1}$	$1.34 \times 10^2 \text{ J kg}^{-1} \text{ K}^{-1}$
T_m	melting temperature	$9.3 \times 10^2 \text{ K}$	$3.65 \times 10^3 \text{ K}$
T_v	vaporisation temperature	$2.5 \times 10^3 \text{ K}$	$5.27 \times 10^3 \text{ K}$
μ	viscosity	$2.7 \times 10^{-3} \text{ Pa s}$	
σ	surface tension	1 kg s^{-2}	

Table 2.1: Physical data for drilling aluminium (Al) and tungsten (W).

Symbol	Definition	Value
λ	wave length	$1.064 \times 10^{-6} \text{ m}$
I_{ref}	energy input	$1.5 \times 10^{10} \text{ W m}^{-2}$
w	waist	$1 \times 10^{-3} \text{ m}$

Table 2.2: Physical data for the Nd:YAG laser beam.

the axisymmetry, is given by

$$\rho c \frac{\partial T}{\partial t} = \frac{k}{r} \frac{\partial}{\partial r} \left(r \frac{\partial T}{\partial r} \right) + k \frac{\partial^2 T}{\partial z^2}. \quad (2.6)$$

The intensity distribution of the laser beam is given by $I = I(r, t)$. The laser energy is supplied at the surface $z = 0$, yielding

$$k \frac{\partial T}{\partial z} = -I. \quad (2.7)$$

Before nondimensionalising we introduce some typical numbers. For the temperature we need the vaporisation temperature T_v and the melting temperature T_m . (In Table 2.1 we give typical parameters for aluminium and tungsten.) For the radial coordinate the *waist*, denoted by w , of the (Gaussian) laser beam is used as a typical length scale. Furthermore, let I_{ref} be a typical intensity. Some data for a Nd:YAG laser used in drilling can be found in Table 2.2. From this we can define the dimensionless variables (indicated by a superbar) by

$$z =: \frac{k(T_v - T_m)}{I_{\text{ref}}} \bar{z}, \quad (2.8)$$

$$r =: w \bar{r}, \quad (2.9)$$

$$t =: \frac{\rho c k (T_v - T_m)^2}{I_{\text{ref}}^2} \bar{t}, \quad (2.10)$$

$$T =: T_m + (T_v - T_m) \theta. \quad (2.11)$$

Symbol	Definition	Value	
		Al	W
ε	$k^2(T_v - T_m)^2 / (w^2 I_{\text{ref}}^2)$	6.1×10^{-4}	2.6×10^{-4}
θ_a	$(T_a - T_m) / (T_v - T_m)$	-0.4	-2.1
λ_f	$L_f / c(T_v - T_m)$	0.25	1.16

Table 2.3: Dimensionless parameters for typical laser percussion drilling processes in aluminium and tungsten.

The dimensionless length scale in z -direction comes from balancing the two terms in the boundary condition (2.7). The dimensionless time scale \bar{t} as introduced in (2.10) is the corresponding diffusive time scale, as follows from (2.6). Writing (2.6) together with the influx of energy (2.7) in dimensionless form we obtain

$$\frac{\partial \theta}{\partial \bar{t}} = \varepsilon \frac{1}{\bar{r}} \frac{\partial}{\partial \bar{r}} \left(\bar{r} \frac{\partial \theta}{\partial \bar{r}} \right) + \frac{\partial^2 \theta}{\partial \bar{z}^2}, \quad (2.12)$$

where

$$\varepsilon = \frac{k^2(T_v - T_m)^2}{w^2 I_{\text{ref}}^2}, \quad (2.13)$$

and

$$\frac{\partial \theta}{\partial \bar{z}} = -\frac{I}{I_{\text{ref}}}, \quad \bar{z} = 0. \quad (2.14)$$

For typical laser percussion drilling parameters, $\varepsilon \ll 1$, see Table 2.3. Thus, radial diffusion can be neglected on the typical scales and our model for the initial stage of the laser percussion drilling process degenerates to a one-dimensional model. This one-dimensional model will therefore be studied in the next chapter and we will only use results of 2-D \bar{r} computations to validate this. Note that we will address phase transitions in two spatial dimensions in the solidification and splashing models.

2.4 Gas Dynamics

In this section we consider the mathematical model of the gas dynamics of a metal vapour. The model is used to predict the recoil pressure of the vapour on the molten metal in the process of laser drilling. This recoil pressure is the driving force of the so called splashing mechanism which is an important mechanism for the removal of material in the drilling process. The high recoil pressures involved also cause significant variation in the vaporisation temperature. A one-dimensional model will be derived and results will be presented.

The following assumptions will be made:

- (i) the time-scale of the gas dynamics is much smaller than the time-scale of the intensity variations,
- (ii) there is no substantial interaction between the laser beam and the vapour (the absorption coefficient of aluminium vapour is 0.5 cm^{-1} at 5000 K [17] and a coaxial jet is employed to remove the vapour from the laser path),
- (iii) the vapour and air behave as ideal gasses,
- (iv) there is no mixing between the vapour and compressed air,
- (v) the liquid-vapour interface has negligible width,
- (vi) all the incoming laser energy is used to vaporise the melt,
- (vii) the three-dimensional problem can be viewed as an infinite set of one-dimensional problems parameterised by the intensity and
- (viii) the compression waves have coalesced to form discontinuities leaving the vapour and compressed air at constant pressure [25].

Through these assumptions, the gas dynamics for this problem is similar to the well-known model of a shock tube. For more detailed information on the shock tube model see e.g. [25, 31]. The gas dynamics for this particular problem has been investigated by several other authors. The two papers that are referred to most are the papers by Anisimov [3] and Knight [23]. Here, the modelling is done in a similar way to the one used in these papers except for the conditions on the liquid-vapour interface.

A schematic representation of the physical situation is shown in Fig. 2.6, in which four regions can be distinguished, as in [23]. The four regions are:

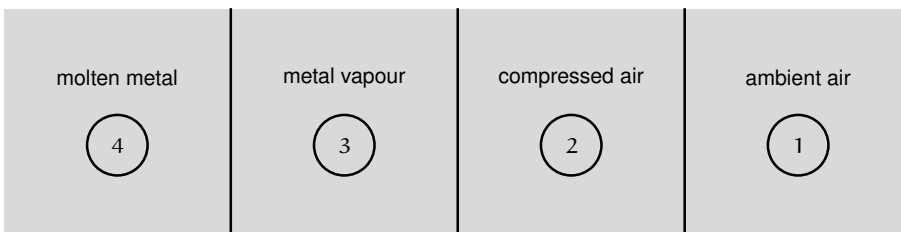


Figure 2.6: *The geometry of the gas dynamics model.*

- ① the ambient air
- ② the compressed air
- ③ the metal vapour

④ the molten metal

These regions are separated by three interfaces: a shockwave between the ambient air ① and the compressed air ②, a contact surface between the compressed air ② and the metal vapour ③, and the liquid-vapour interface between the metal vapour ③ and the molten metal ④. Within these regions the variables are taken to be constant, which is a normal procedure in the literature, see [25]. Across the shockwave we have got the following *Rankine-Hugoniot* shock relations, see for instance [31, p. 83]

$$\rho_1(U - u_1) = \rho_2(U - u_2), \quad (2.15)$$

$$p_1 + \rho_1(U - u_1)^2 = p_2 + \rho_2(U - u_2)^2, \quad (2.16)$$

$$c_1 T_1 + \frac{1}{2}(U - u_1)^2 = c_2 T_2 + \frac{1}{2}(U - u_2)^2, \quad (2.17)$$

where U is the speed of the shock, p the pressure, ρ the density, u the velocity, T the temperature, c the specific heat capacity at constant pressure and the subscripts denote the region of interest. These three equations are a consequence of conservation of mass, conservation of momentum and conservation of energy, respectively. Across the contact surface we have, see [25, p. 81]

$$p_2 = p_3, \quad (2.18)$$

$$u_2 = u_3. \quad (2.19)$$

Let L_v denote the latent heat of vaporisation, I the laser intensity and c_v the specific heat capacity at constant volume of the melt. Across the liquid-vapour interface we have

$$\rho_4 u_4 = \rho_3 u_3 \quad (2.20)$$

$$p_4 + \rho_4 u_4^2 = p_3 + \rho_3 u_3^2, \quad (2.21)$$

$$\rho_4 u_4 \left(c_v T_4 + \frac{1}{2} u_4^2 + \frac{p_4}{\rho_4} \right) + I = \rho_3 u_3 \left(c_3 T_3 + L_v + \frac{1}{2} u_3^2 \right). \quad (2.22)$$

These equations again represent conservation of mass, conservation of momentum and conservation of energy, respectively. We note that

$$\frac{\rho_3}{\rho_4} \ll 1,$$

so that from Equation (2.20) follows that

$$\frac{u_4}{u_3} \ll 1,$$

furthermore,

$$\rho_4 u_4^2 \ll \rho_3 u_3^2, \quad \frac{1}{2} u_4^2 \ll \frac{1}{2} u_3^2, \quad \frac{p_4}{\rho_4} \ll \frac{p_3}{\rho_3}.$$

Together with the assumption that all the energy is used to vaporise the material,

$$I = \rho_4 u_4 L_v,$$

we arrive at the following set of equations

$$\rho_3 u_3 = \frac{I}{L_v}, \quad (2.23)$$

$$p_3 + \rho_3 u_3^2 = p_4, \quad (2.24)$$

$$c_3 T_3 + \frac{1}{2} u_3^2 = c_v T_4. \quad (2.25)$$

To close the system of equations, we must add three constitutive laws. We assumed the metal vapour ② and the compressed air ③ to be ideal gasses. This yields

$$p_2 = R_2 \rho_2 T_2, \quad (2.26)$$

$$p_3 = R_3 \rho_3 T_3, \quad (2.27)$$

where R_i for $i = 2, 3$ is the universal gas constant in the appropriate region. Across the liquid-vapour interface we use the *Rankine-Kirchhoff equation*

$$p_4(T_4) = p_4(T_{\text{ref}}) \left(\frac{T_4}{T_{\text{ref}}} \right)^{\frac{c_3 - c_4}{R_3}} \exp \left\{ \frac{L_0}{R_3} \left(\frac{1}{T_{\text{ref}}} - \frac{1}{T_4} \right) \right\}, \quad (2.28)$$

where the subscript 'ref' refers to an arbitrary reference state and $L_v = L_0 + (c_3 - c_4)T_4$. This Rankine-Kirchhoff equation is a first integral of the *Clausius-Clapeyron equation*, see e.g. [24]. Because the quantities c_* , R_* , L , p_1 , u_1 , $\rho_{1,4}$, T_1 and $p_4(T_{\text{ref}})$ are known, we can solve the system consisting of equations (2.15)-(2.19) and (2.23)-(2.28) with respect to the intensity I .

The system of equations is rewritten as

$$\mathbf{f} = \mathbf{0}, \quad (2.29)$$

where \mathbf{f} is defined by

$$\mathbf{f} := \begin{pmatrix} \rho_1(u - u_1) - \rho_2(u - u_2) \\ p_1 + \rho_1(u - u_1)^2 - R_2 \rho_2 T_2 - \rho_2(u - u_2)^2 \\ c_1 T_1 + \frac{1}{2}(u - u_1)^2 - c_2 T_2 - \frac{1}{2}(u - u_2)^2 \\ R_2 \rho_2 T_2 - R_3 \rho_3 T_3 \\ \rho_3 u_2 - \frac{I}{L_v} \\ \rho_3 u_2^2 + R_2 \rho_2 T_2 - p_4 \\ c_3 T_3 + \frac{1}{2} u_2^2 - c_v T_4 \\ p_4 - p_4(T_{\text{ref}}) \left(\frac{T_4}{T_{\text{ref}}} \right)^{\frac{c_3 - c_4}{R_3}} \exp \left[\frac{L_0}{R_3} \left(\frac{1}{T_{\text{ref}}} - \frac{1}{T_4} \right) \right] \end{pmatrix}. \quad (2.30)$$

This set is then, depending on I , solved with respect to \mathbf{x} , defined as

$$\mathbf{x} := \begin{pmatrix} u_2 \\ u \\ T_2 \\ \rho_2 \\ \rho_3 \\ p_4 \\ T_3 \\ T_4 \end{pmatrix}. \quad (2.31)$$

With the parameters as given in Table 2.4 we get the results as shown in Figures 2.7 to 2.10. In Figure 2.7 the different velocities as a function of intensity are sketched.

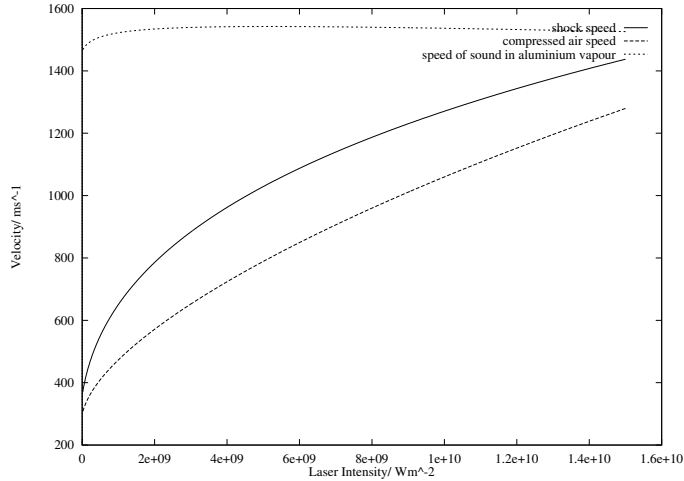


Figure 2.7: *The different velocities as a function of intensity.*

The speed of sound in aluminium vapour is included to show that the shock speed is subsonic in our regime of laser intensities. Note that this is in contradiction with the assumption that the shock speed is sonic, made in [18, 19]. The magnitude of these velocities with the typical length-scale (~ 1 mm) allows us to determine the time-scale for the gas dynamics ($\sim 10^{-6}$ s). In Figure 2.8 the different densities as a function of

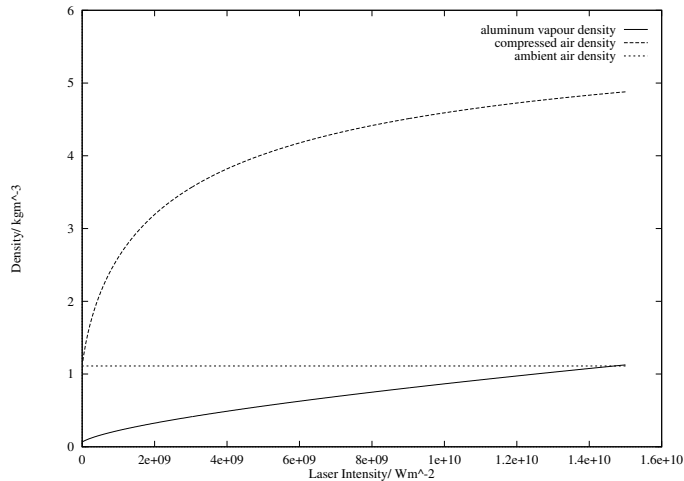


Figure 2.8: *The different densities as a function of intensity.*

intensities are plotted. The ambient air density is included as a reference. One can see that the compressed air density is much higher than the density of the metal vapour. Figure 2.10 shows the pressures as a function of intensity. One can see that

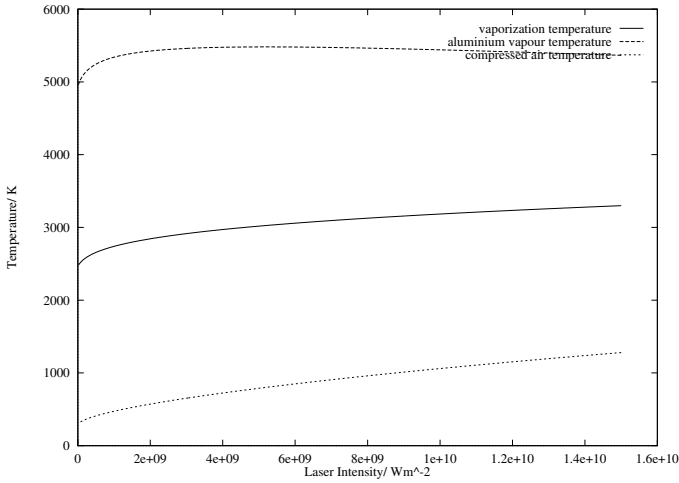


Figure 2.9: *The different temperatures as a function of intensity.*

the difference between the recoil pressure and the compressed air pressure becomes larger with intensity. The radial pressure gradient can now be deduced from the known variation of intensity with radius. This is a necessary input to the splashing model. The high recoil pressure (p_4) also causes the vaporisation temperature to vary considerably over the intensity régime (shown in Figure 2.9). This also has to serve as an input for the splashing model in which the vaporisation is included. A first order approximation of the velocity with which the melt gets splashed out can be found as follows. If we use the value for the recoil pressure as the driving force for the splashing mechanism, we get the velocity by simply balancing the forces,

$$u = \left(\frac{2p}{\rho} \right)^{\frac{1}{2}}. \quad (2.32)$$

The velocities found with this approximation are sketched in Figure 2.11. Note that this order of magnitude is also mentioned by Von Allmen [1, p. 132].

2.5 Splashing and solidification

The mathematical modelling of splashing and solidification is considered in this section. To see which physical phenomena play an important role in these processes we first look at the parameter régimes in Section 2.5.1. As the mathematical model of solidification is less complex than the splashing model we consider this first (Section 2.5.2). The mathematical model of splashing is presented in Section 2.5.3. These mathematical models will be studied further, both analytically and numerically, in Chapter 5.

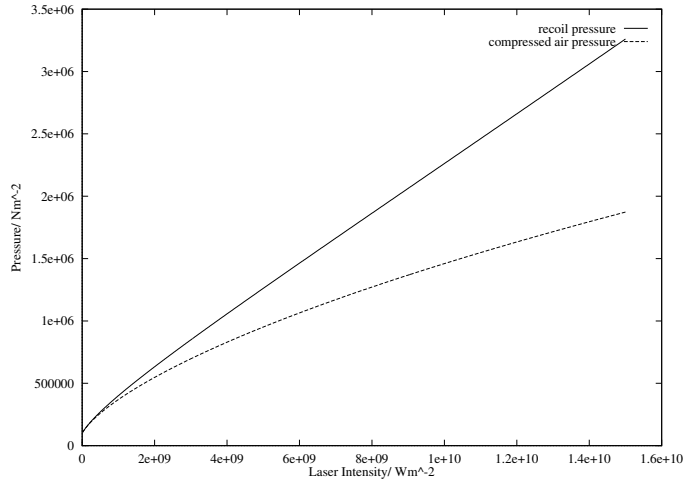


Figure 2.10: The different pressures as a function of intensity.

2.5.1 Parameter régimes

The different parameters in the model depend on laser set-up, the material to be drilled and the temperature, which for aluminium may vary from 300K to 2500K. For the drilling of aluminium the parameters are given in Table 2.2 (see, for example, [34]). With a length-scale of $L \sim 10^{-3}$ m and thickness $d \sim 10^{-4}$ m, a typical aspect ratio is given by $\delta = d/L \sim 0.1$. Of course the aspect ratio changes considerably during the ejection of the melt and the variation in viscosity can result in deviation in the Reynolds number. With a typical maximum velocity given by $U \sim 50\text{ms}^{-1}$ (see [1, p. 132]), we have the following dimensionless numbers. The *Reynolds number*, which compares the effects of inertia and viscosity, is given by

$$\text{Re} := \frac{\rho U L}{\mu} \sim 5 \cdot 10^4. \quad (2.33)$$

The *Froude number*, which compares inertia and gravity,

$$\text{Fr} := \frac{U^2}{Lg} \sim 2.5 \cdot 10^5, \quad (2.34)$$

where g is the acceleration due to gravity. The *Prandtl number*, which compares the viscous time scale with that of heat conduction,

$$\text{Pr} := \frac{\mu c}{k} \sim 10^{-2}. \quad (2.35)$$

The *Peclet number*, which compares the inertial time scale with that of conduction,

$$\text{Pe} := \text{Re} \cdot \text{Pr} = 5 \cdot 10^2. \quad (2.36)$$

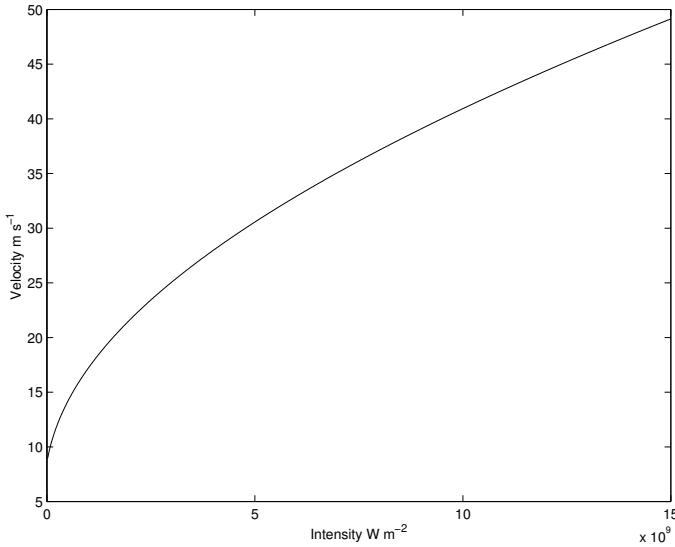


Figure 2.11: The first-order estimate according to Eq. (2.32) of the velocity of the expelled melt as a function of intensity.

The *Brinkman number*, which compares viscous dissipation of heat with heat conduction,

$$\text{Br} := \frac{\mu U^2}{k(T_v - T_m)} \sim 3 \times 10^{-5}. \quad (2.37)$$

Finally, we give the *Weber number* of the problem, which, if it is large, rules out surface tension

$$\text{We} := \frac{\rho U^2 L}{\sigma} \sim 7 \times 10^3, \quad (2.38)$$

where σ is the surface tension. The magnitude of the parameters motivates us to consider the flow as inviscid with heat convection and conduction, neglecting viscous boundary layers and gravity. Moreover, we assume that the vorticity is initially zero, so that we may consider the flow as irrotational.

The melt ejection is considered axisymmetric. Because the radius of curvature of the geometry is so much larger than the melt thickness, we adopt an axisymmetric representation for the splashing and a planar representation for the solidification. In the splashing model, we make the simplifying assumption that the entire fluid interface is vaporising. However, it may very well be the case that only a fraction is at vaporisation temperature and a mixed boundary value problem needs to be studied. As the splashing model is more complex, we derive the solidification model first.

Parameter	Value
R_1	$3.0 \times 10^2 \text{ N m kg}^{-1} \text{ K}^{-1}$
R_2	$3.0 \times 10^2 \text{ N m kg}^{-1} \text{ K}^{-1}$
R_3	$3.1 \times 10^2 \text{ N m kg}^{-1} \text{ K}^{-1}$
c_1	$1.0 \times 10^3 \text{ J kg}^{-1} \text{ K}^{-1}$
c_2	$1.0 \times 10^3 \text{ J kg}^{-1} \text{ K}^{-1}$
c_3	$5.0 \times 10^2 \text{ J kg}^{-1} \text{ K}^{-1}$
c_{p4}	$1.0 \times 10^3 \text{ J kg}^{-1} \text{ K}^{-1}$
c_v	$1.0 \times 10^3 \text{ J kg}^{-1} \text{ K}^{-1}$
L_v	$1.2 \times 10^7 \text{ J kg}^{-1}$
T_{ref}	$2.5 \times 10^3 \text{ K}$
$p_4(T_{\text{ref}})$	$1.2 \times 10^5 \text{ N m}^{-2}$
u_1	0.0 m s^{-1}
p_1	$1.0 \times 10^5 \text{ N m}^{-2}$
T_1	$3.0 \times 10^2 \text{ K}$

Table 2.4: The data for the gas dynamics.

2.5.2 Planar solidification

We consider an incompressible fluid contained in the vertical direction by a bottom defined by $y = s(x, t)$ and a top defined by $y = h(x, t)$ as indicated in Figure 2.12, where x and y are the coordinates in the horizontal (along the side wall) and vertical (perpendicular to this side wall) directions, respectively, and t is time. We denote this liquid by Ω_l .

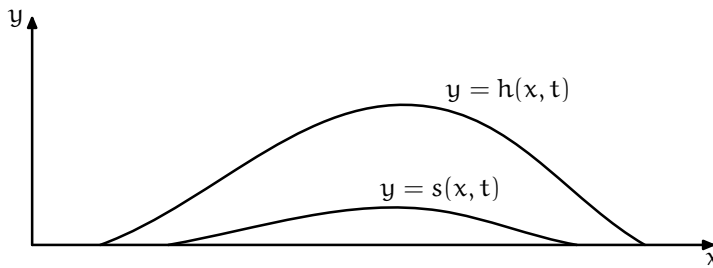


Figure 2.12: Planar representation of solidification. The horizontal direction (along the side wall) is denoted by x and the vertical direction (perpendicular to this side wall) by y . The incompressible fluid is in the region $s(x, t) < y < h(x, t)$ and the solid is in the region $y < s(x, t)$.

Solidified material is present in the region $\Omega_s := y < s(x, t)$. The initial boundary value problem for the velocity potential $\phi(x, y, t)$, temperature $T(x, y, t)$ and unknown free surfaces $y = s(x, t)$ and $y = h(x, t)$ is stated in the following. We have

conservation of mass

$$\nabla^2 \phi = 0, \quad (2.39a)$$

conservation of energy

$$\frac{\partial T}{\partial t} + \nabla \phi \cdot \nabla T = \frac{k}{\rho c} \nabla^2 T, \quad (2.39b)$$

in the liquid. Conservation of energy in the solid leads to

$$\frac{\partial T}{\partial t} = \frac{k}{\rho c} \nabla^2 T \quad \text{in } \Omega_s. \quad (2.40)$$

On the solid-liquid interface, we have the melting isotherm

$$T = T_m, \quad (2.41a)$$

conservation of mass

$$\nabla \phi \cdot \nabla (y - s) = 0, \quad (2.41b)$$

and the Stefan condition

$$\rho L_f \frac{\partial s}{\partial t} + k [\nabla T]_{s^-}^{s^+} \cdot \nabla (y - s) = 0 \quad \text{on } y = s(x, t), \quad (2.41c)$$

At infinity we have ambient temperature

$$T \rightarrow T_a \quad \text{as } y \rightarrow -\infty. \quad (2.42)$$

The boundary conditions on the top surface are given by

$$\frac{D}{Dt} (y - h) = 0, \quad (2.43a)$$

$$\frac{\partial \phi}{\partial t} + \frac{1}{2} |\nabla \phi|^2 = 0, \quad (2.43b)$$

$$\nabla T \cdot \nabla (y - h) = 0 \quad \text{on } y = h(x, t). \quad (2.43c)$$

The boundary conditions in (2.43) represent conservation. Eq. 2.43a is conservation of mass, 2.43b of momentum and 2.43c of energy. For the general formulations of the conservation of mass and energy boundary conditions, see [12].

We transform the system of equations (2.39)- (2.43) to the dimensionless variables via $\phi = U L \hat{\phi}$, $T = T_m + (T_v - T_m) \theta$, $s = d \hat{s}$, $h = d \hat{h}$, $x = L \hat{x}$, $y = d \hat{y}$ and $t = L \hat{t} / U$, where T_v is the vaporisation temperature at one atmosphere pressure. The solidification model then becomes (and without ambiguity the hats on the non-dimensional variables can be omitted)

$$\frac{\partial^2 \phi}{\partial x^2} + \frac{1}{\delta^2} \frac{\partial^2 \phi}{\partial y^2} = 0, \quad (2.44a)$$

Symbol	Definition	Typical Value
δ	d/L	0.1
D	$k/\rho c U L \delta^2$	0.2
λ_f	$L_f/c(T_v - T_m)$	0.3
λ_v	$L_v(T_v)/c(T_v - T_m)$	8
θ_a	$(T_a - T_m)/(T_v - T_m)$	-0.4

Table 2.5: Dimensionless parameters for a typical laser percussion drilling process on aluminium.

$$\frac{\partial T}{\partial t} + \frac{\partial \phi}{\partial x} \frac{\partial T}{\partial x} + \frac{1}{\delta^2} \frac{\partial \phi}{\partial y} \frac{\partial T}{\partial y} = D \left(\delta^2 \frac{\partial^2 T}{\partial x^2} + \frac{\partial^2 T}{\partial y^2} \right), \quad \text{in } \Omega_l, \quad (2.44b)$$

$$\frac{\partial T}{\partial t} = D \left(\delta^2 \frac{\partial^2 T}{\partial x^2} + \frac{\partial^2 T}{\partial y^2} \right), \quad \text{in } \Omega_s, \quad (2.45)$$

$$\frac{1}{\delta^2} \frac{\partial \phi}{\partial y} = \frac{\partial h}{\partial t} + \frac{\partial \phi}{\partial x} \frac{\partial h}{\partial x}, \quad (2.46a)$$

$$\frac{\partial \phi}{\partial t} + \frac{1}{2} \left(\left(\frac{\partial \phi}{\partial x} \right)^2 + \frac{1}{\delta^2} \left(\frac{\partial \phi}{\partial y} \right)^2 \right) = 0, \quad (2.46b)$$

$$\frac{\partial \theta}{\partial y} = \delta^2 \frac{\partial h}{\partial x} \frac{\partial \theta}{\partial x} \quad \text{on } y = h(x, t), \quad (2.46c)$$

$$\theta = 0, \quad (2.47a)$$

$$\frac{1}{\delta^2} \frac{\partial \phi}{\partial y} = \frac{\partial \phi}{\partial x} \frac{\partial s}{\partial x}, \quad (2.47b)$$

$$\lambda_f \frac{\partial s}{\partial t} + D \left[\frac{\partial \theta}{\partial y} - \delta^2 \frac{\partial s}{\partial x} \frac{\partial \theta}{\partial x} \right]_{s^-}^{s^+} = 0, \quad \text{on } y = s(x, t), \quad (2.47c)$$

$$\theta \rightarrow \theta_a \quad \text{as } y \rightarrow -\infty. \quad (2.48)$$

The dimensionless constants δ , D , λ_f and θ_a are defined, and typical values for aluminium given in Table 2.5. For the parameter δ , representing the aspect ratio, the constraint $\delta^2 \ll 1$ typically holds in practice. The solidification model is regularly perturbed in this small parameter and this fact will be exploited in Chapter 5.

2.5.3 Axisymmetric splashing model

Again, we consider an incompressible fluid contained in the vertical direction by a bottom defined by $z = s(r, t)$ and a top defined by $z = h(r, t)$ as indicated in Figure 2.13, where r and z are the coordinates in the axial and vertical directions, respectively, and t is time. We denote this region by Ω_l .

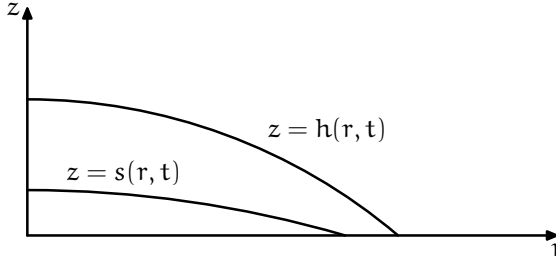


Figure 2.13: Axisymmetric representation of splashing. The axial direction is denoted by r and the vertical direction by z . The incompressible fluid is in the region $s(r, t) < z < h(r, t)$ and the solid is in the region $z < s(r, t)$.

Solidified material is present in the region $\Omega_s := z < s(r, t)$. The initial boundary value problem for the potential $\phi(r, z, t)$, temperature $T(r, z, t)$ and unknown free surfaces $z = s(r, t)$ and $z = h(r, t)$ is stated in the following.

We have conservation of mass

$$\nabla^2 \phi = 0, \quad (2.49a)$$

and energy

$$\frac{\partial T}{\partial t} + \nabla \phi \cdot \nabla T = \frac{k}{\rho c} \Delta T, \quad \text{in } \Omega_l, \quad (2.49b)$$

in the liquid. Conservation of energy in the solid

$$\frac{\partial T}{\partial t} = \frac{k}{\rho c} \nabla^2 T \quad \text{in } \Omega_s. \quad (2.50)$$

On the vaporising surface, we have the vaporisation isotherm

$$T = T_v(p), \quad (2.51a)$$

conservation of momentum,

$$\frac{\partial \phi}{\partial t} + \frac{1}{2} |\nabla \phi|^2 + \frac{p}{\rho} = 0, \quad (2.51b)$$

and conservation of energy

$$-I + k \left(\frac{\partial T}{\partial z} - \frac{\partial h}{\partial r} \frac{\partial T}{\partial r} \right) + \rho L_v(T_v(p)) \left(-\frac{\partial h}{\partial t} - \frac{\partial h}{\partial r} \frac{\partial \phi}{\partial r} + \frac{\partial \phi}{\partial z} \right) = 0. \quad (2.51c)$$

Here p is the recoil pressure, I is the influx of laser energy, $T_v(p)$ is the vaporisation temperature as a function of recoil pressure, $L_v(T_v(p))$ is the latent heat of vaporisation. The solid-liquid interface is at melting temperature,

$$T = T_m. \quad (2.52a)$$

Furthermore, conservation of mass holds

$$\frac{\partial \phi}{\partial z} = \frac{\partial s}{\partial r} \frac{\partial \phi}{\partial r}, \quad (2.52b)$$

and we have the Stefan condition

$$\rho L_f \frac{\partial s}{\partial t} + k \left[\frac{\partial T}{\partial z} - \frac{\partial s}{\partial r} \frac{\partial T}{\partial r} \right]_{s^-}^{s^+} = 0. \quad (2.52c)$$

At infinity we have ambient conditions

$$T \rightarrow T_a \quad \text{as } z \rightarrow -\infty, \quad (2.53)$$

where T_a is the ambient temperature.

The recoil pressure, the input of laser energy and the vaporisation temperature are required to complete the mathematical model for splashing. The recoil pressure is obtained via the shocktube approach, which is outlined in the previous section.

We transform to dimensionless variables via $\phi = UL\hat{\phi}$, $T = T_m + (T_v - T_m)\theta$, $s = d\hat{s}$, $h = d\hat{h}$, $r = L\hat{r}$, $z = d\hat{z}$ and $t = L\hat{t}/U$. By again omitting the hats on the non-dimensional variables the axisymmetric splashing model then becomes

$$\frac{\partial^2 \phi}{\partial r^2} + \frac{1}{r} \frac{\partial \phi}{\partial r} + \frac{1}{\delta^2} \frac{\partial^2 \phi}{\partial z^2} = 0, \quad (2.54a)$$

$$\frac{\partial \theta}{\partial t} + \frac{\partial \phi}{\partial r} \frac{\partial \theta}{\partial r} + \frac{1}{\delta^2} \frac{\partial \phi}{\partial z} \frac{\partial \theta}{\partial z} = D \left\{ \delta^2 \left(\frac{\partial^2 \theta}{\partial r^2} + \frac{1}{r} \frac{\partial \theta}{\partial r} \right) + \frac{\partial^2 \theta}{\partial z^2} \right\}, \quad \text{in } \Omega_l, \quad (2.54b)$$

$$\frac{\partial \theta}{\partial t} = D \left\{ \delta^2 \left(\frac{\partial^2 \theta}{\partial r^2} + \frac{1}{r} \frac{\partial \theta}{\partial r} \right) + \frac{\partial^2 \theta}{\partial z^2} \right\}, \quad \text{in } \Omega_s, \quad (2.55)$$

$$\theta = \theta_v(\bar{p}), \quad (2.56a)$$

$$\frac{\partial \phi}{\partial t} + \frac{1}{2} \left(\left(\frac{\partial \phi}{\partial r} \right)^2 + \frac{1}{\delta^2} \left(\frac{\partial \phi}{\partial z} \right)^2 \right) + \bar{p} = 0, \quad (2.56b)$$

$$\frac{1}{\delta^2} \frac{\partial \phi}{\partial z} - \frac{\partial \phi}{\partial r} \frac{\partial h}{\partial r} - \frac{\partial h}{\partial t} = \bar{I} - \frac{D}{\lambda_v \bar{L}_v} \left(\frac{\partial \theta}{\partial z} - \delta^2 \frac{\partial h}{\partial r} \frac{\partial \theta}{\partial r} \right) \quad \text{on } z = h(r, t), \quad (2.56c)$$

$$\theta = 0, \quad (2.57a)$$

$$\frac{1}{\delta^2} \frac{\partial \phi}{\partial z} = \frac{\partial \phi}{\partial r} \frac{\partial s}{\partial r}, \quad (2.57b)$$

$$\lambda_f \frac{\partial s}{\partial t} + D \left[\frac{\partial \theta}{\partial z} - \delta^2 \frac{\partial s}{\partial r} \frac{\partial \theta}{\partial r} \right]_{s^-}^{s^+} = 0 \quad \text{on } z = s(r, t), \quad (2.57c)$$

$$\theta \rightarrow \theta_a \quad \text{as } z \rightarrow -\infty, \quad (2.58)$$

where $\bar{p} = p/\rho U^2$, $\bar{I} = IL/\rho dUL_v$ (where typically $\bar{I} \sim 0.1$) and $\bar{L}_v = L_v/L_v(T_v)$ are specified functions. The dimensionless constants δ , D , λ_f , λ_v and θ_a are defined, and typical values for aluminium given in Table 2.5. For the parameters δ , representing the aspect ratio and λ_v , the Stefan number for vaporisation, the constraints $\delta^2 \ll 1$ and $1/\lambda_v \ll 1$ typically hold in practice. The model is a regular perturbation in these small parameters. This fact will be exploited in Chapter 5 to derive an asymptotic splashing model which will be solved numerically.

Laser induced melting

In this chapter we will focus on the laser induced melting. Melting problems are commonly known as *Stefan problems* named after J. Stefan, who wrote his famous article about the building up of ice in polar seas in 1891, see [43]. Several formulations of melting problems have been studied in literature so far; extensive overviews can be found in [6, 7, 52]. We will focus on the formulation using the original Stefan condition (see e.g. [4]) and the enthalpy method (see for instance [44, 48, 49]). Furthermore, we will pay attention to finding suitable initial conditions for the formulation using the Stefan condition in applying this method to the laser percussion drilling process. To be able to deal with superalloys, we will assess the problems both for materials having a melting range and for materials with a discrete melting point. Furthermore, in the last section of this chapter the numerical issues related to modelling of melting in two spatial variables will be addressed. This is not of key importance to modelling of melting as such, but will be important in modelling splashing and solidification.

3.1 Modelling melting

In this section we will outline two different ways to formulate the melting problem. Each formulation will give rise to a numerical scheme with its own vices and virtues. As shown in the previous chapter the importance of radial diffusion in laser induced melting is negligible. Therefore, we will study the one-dimensional model. That is, the axisymmetric model can be viewed as an infinite set of one-dimensional problems parameterised by the intensity, which is a function of the radial coordinate.

We shall consider two models. One is based on use of the Stefan condition; this will therefore be referred to as the *Stefan problem*. The other is employing an enthalpy formulation, and will be referred to as the *enthalpy problem*.

3.1.1 The Stefan Problem

Let Ω_l denote the liquid region $0 \leq z < s(t)$ and Ω_s the solid region $s(t) < z < \infty$. Furthermore, let $s(t)$ be the position of the solid-liquid interface. The geometry is sketched in Figure 3.1. The temperature in both the liquid and the solid region is

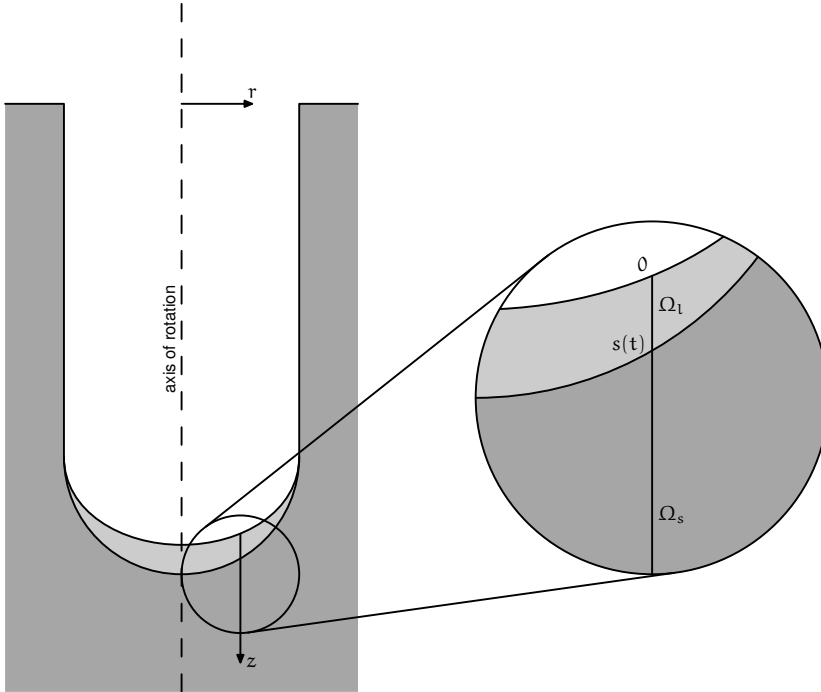


Figure 3.1: The geometry of the laser induced melting problem.

governed by the heat equation, which in dimensionless form reads

$$\frac{\partial \theta_i}{\partial t} = \frac{\partial^2 \theta_i}{\partial z^2} \quad \text{in } \Omega_i \quad \text{for } i = s, l. \quad (3.1)$$

Here the subscripts s and l refer to solid and liquid, respectively. At the boundary $z = 0$ the laser supplies an intensity $I = I(r, t)$,

$$\frac{\partial \theta_l}{\partial z} = -\frac{I}{I_{\text{ref}}}, \quad z = 0. \quad (3.2)$$

For a material to melt, an extra amount of energy has to be supplied, the *latent heat of fusion*, which, in dimensionless form, is defined as

$$\lambda_f := \frac{L_f}{c(T_v - T_m)}. \quad (3.3)$$

At the solid-liquid interface we need an equation that expresses this absorption of heat needed for phase change. This equation is commonly known as the *Stefan condition* and is given by

$$\frac{\partial \theta_l}{\partial z} \Big|_{z \uparrow s} - \frac{\partial \theta_s}{\partial z} \Big|_{z \downarrow s} = -\lambda_f \frac{ds}{dt}, \quad z = s(t). \quad (3.4)$$

Moreover, the temperature is assumed to be continuous across the interface

$$\theta_s = \theta_l = 0 \quad z = s(t). \quad (3.5)$$

At infinity, the boundary condition

$$\theta_s \rightarrow \theta_\alpha, \quad z \rightarrow \infty \quad (3.6)$$

holds, where θ_α is the dimensionless ambient temperature of the material. We start with a known temperature distribution

$$\theta(z, 0) = \theta_0(z). \quad (3.7)$$

3.1.2 The Enthalpy Problem

The enthalpy H is defined as the sum of the sensible and the latent heat in a substance. If a material is liquid it contains latent heat of fusion per unit mass L_f , in addition to the sensible heat $\rho c T$. Figure 3.2 shows the relation between the temperature and the enthalpy for two different materials. Figure 3.2(a) shows this relation for pure substances with a single melting-point temperature, whereas figure 3.2(b) illustrates this relation for a material where the phase change takes place over an extended temperature range from the solidus temperature T_{sol} to the liquidus temperature T_{liq} . The region with temperature between the solidus and the liquidus temperature is referred to as the *mushy region*. We define the dimensionless enthalpy, η , by

$$\eta = \begin{cases} \theta & \theta < 0, \\ [0, \lambda_f], & \theta = 0, \\ \theta + \lambda_f & \theta > 0. \end{cases} \quad (3.8)$$

Vice versa, we have

$$\theta = \begin{cases} \eta, & \eta < 0, \\ 0, & 0 < \eta < \lambda_f, \\ \eta - \lambda_f & \eta > \lambda_f. \end{cases} \quad (3.9)$$

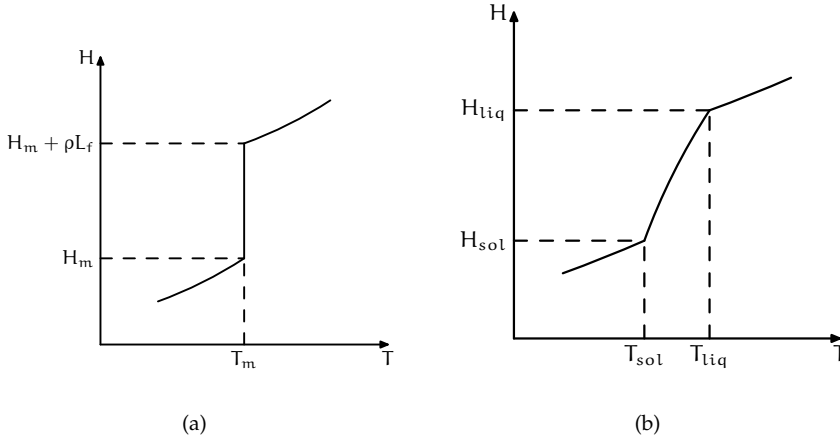


Figure 3.2: Relation of enthalpy and temperature for (a) pure crystalline substances and (b) glassy substances and alloys.

Likewise, the relationship between the dimensionless enthalpy and temperatures for materials with a melting range is given by

$$\eta = \begin{cases} \theta & \theta \leq 0, \\ \theta + \lambda_f \frac{\theta}{\theta_{liq}} & 0 \leq \theta \leq \theta_{liq}, \\ \theta + \lambda_f & \theta \geq \theta_{liq}. \end{cases} \quad (3.10)$$

Note that θ_{liq} denotes the dimensionless liquidus temperature and that $\lambda_f = \frac{L_f}{c(T_v - T_{sol})}$ now. The inverse relation between temperature and enthalpy in this case is

$$\theta = \begin{cases} \eta & \eta \leq 0, \\ \frac{\theta_{liq}}{\theta_{liq} + \lambda_f} \eta & 0 \leq \eta \leq \theta_{liq} + \lambda_f, \\ \eta - \lambda_f & \eta > \theta_{liq} + \lambda_f. \end{cases} \quad (3.11)$$

As has been shown in the previous chapter, the laser induced melting problem degenerates to a one-dimensional problem. Like in the previous subsection we take the material to be in $z \geq 0$ with the surface at $z = 0$. The enthalpy and temperature of the material in this region are governed by the energy equation in enthalpy form, which, in dimensionless form, is given by

$$\frac{\partial \eta}{\partial t} = \frac{\partial^2 \theta}{\partial z^2}, \quad z > 0, \quad (3.12)$$

for materials with a discrete melting point. The boundary and initial conditions are the same as in the previous subsection. The influx of energy is represented by

$$\frac{\partial \theta}{\partial z} = -\frac{I}{I_{\text{ref}}}, \quad z = 0. \quad (3.13)$$

We assume an ambient temperature infinity

$$\theta \rightarrow \theta_a, \quad z \rightarrow \infty, \quad (3.14)$$

and we begin with a known initial temperature (and hence enthalpy) distribution

$$\theta = \theta_0, \quad t = 0. \quad (3.15)$$

3.2 Numerical methods for melting

In this section we will consider the numerical techniques used to solve the Stefan problem. These numerical methods relate to the various formulations of the melting problem we saw in the previous section. Section 3.2.1 deals with a discretisation of the formulation using the Stefan condition, in Section 3.2.3 a discretisation based on the enthalpy method is dealt with. The PDE's are numerically solved by the finite element method. The finite element method is preferred to other methods such as the finite difference method because of its versatility in dealing with complex boundaries. Though we saw that the melting problem degenerates to a one-dimensional one, the procedure used to solve the enthalpy method can easily be generalised to 2D and 3D, which will be needed for the splashing and solidification models. This procedure will be outlined in the next section.

3.2.1 Discretisation of the Stefan Problem

Finite element methods are a powerful tool in the solution of partial differential equations, also when moving boundaries are involved cf. [6, 15]. One way to handle such a moving boundary is to use subdomains that change with time. Another way to deal with the moving boundary is to use a transformation, see e.g. [29]. The latter method, however, is not applicable to problems where no liquid is present initially.

The derivation consists of the following steps: (i) a Galerkin formulation, (ii) a discretisation method and (iii) the solution of the resulting initial value problems with (iv) suitable initial conditions. The last step involves some subtleties in our problem and will be considered separately in the next subsection.

The problem to begin with is given in Section 3.1.1, but we simplify it by cutting off

the domain at $z = z_b$. The problem is then given by

$$\left\{ \begin{array}{ll} \frac{\partial \theta_l}{\partial t} = \frac{\partial^2 \theta_l}{\partial z^2}, & 0 < z < s(t) \\ \frac{\partial \theta_s}{\partial t} = \frac{\partial^2 \theta_s}{\partial z^2}. & s(t) < z < z_b \\ \frac{\partial \theta_l}{\partial z} = -\frac{I}{I_{\text{ref}}}, & z = 0, \\ \theta_l = \theta_s = 0; \quad \frac{\partial \theta_l}{\partial z} \Big|_{z \uparrow s} - \frac{\partial \theta_s}{\partial z} \Big|_{z \downarrow s} = -\lambda_f \frac{ds}{dt}, & z = s(t), \\ \theta_s = \theta_a, & z = z_b, \end{array} \right. \quad (3.16)$$

along with suitable initial conditions for the temperature and the position of the solid-liquid interface s .

If θ_l satisfies the PDE in (3.16), then it also satisfies

$$\int_0^s \left\{ \frac{\partial \theta_l}{\partial t} - \frac{\partial^2 \theta_l}{\partial z^2} \right\} v(z, t) dz = 0, \quad (3.17a)$$

for all suitable weight functions $v(z, t)$. Likewise θ_s satisfies

$$\int_s^{z_b} \left\{ \frac{\partial \theta_s}{\partial t} - \frac{\partial^2 \theta_s}{\partial z^2} \right\} w(z, t) dz = 0, \quad (3.17b)$$

for all suitable weight functions $w(z, t)$. Let the weight functions $v(z, t)$ and $w(z, t)$ satisfy $v(s, t) = w(s, t) = w(z_b, t) = 0$ for all t . Using integration by parts and the first boundary condition of (3.16), (3.17) can be rewritten as

$$\int_0^s \left\{ \frac{\partial \theta_l}{\partial t} v(z, t) + \frac{\partial \theta_l}{\partial z} \frac{\partial v}{\partial z} \right\} dz = \frac{I}{I_{\text{ref}}} v(0, t), \quad (3.18a)$$

and

$$\int_s^{z_b} \left\{ \frac{\partial \theta_s}{\partial t} w(z, t) + \frac{\partial \theta_s}{\partial z} \frac{\partial w}{\partial z} \right\} dz = 0. \quad (3.18b)$$

To solve the Galerkin form (3.18), we compute approximate solutions of the boundary and the temperature distributions. First we fix the time t and divide the domains $0 \leq z \leq s(t)$ and $s(t) \leq z \leq z_b$ into N and M equal subintervals, respectively. Next, at each node in the liquid domain

$$z_{l,j} = j h_l, \quad j = 0, \dots, N; \quad \text{with} \quad h_l = h_l(t) = \frac{s(t)}{N} \quad (3.19)$$

we construct the usual hat function $\varphi_{l,j}(z, t)$. The same is done for each node in the solid part

$$z_{s,j} = s(t) + jh_s, \quad j = 0, \dots, M; \quad \text{with} \quad h_s = h_s(t) = \frac{z_b - s(t)}{M} \quad (3.20)$$

where the hat functions are denoted by $\varphi_{s,j}(z, t)$. Note that in contrast with the usual basis functions used for finite element methods, these basis functions depend on time. For later use we note that

$$\frac{dz_{l,j}}{dt} = j \frac{dh_l}{dt} = \frac{j}{N} \frac{ds}{dt}, \quad (3.21)$$

and

$$\frac{dz_{s,j}}{dt} = \frac{ds}{dt} + j \frac{dh_s}{dt} = \frac{M-j}{M} \frac{ds}{dt}. \quad (3.22)$$

Next we determine approximate solutions of the forms

$$\theta_{h_l}(z, t) = \sum_{j=0}^N \theta_{l,j}(t) \varphi_{l,j}(z, t), \quad \theta_{h_s}(z, t) = \sum_{j=0}^M \theta_{s,j}(t) \varphi_{s,j}(z, t). \quad (3.23)$$

Letting $\theta_{l,N}(t) \equiv 0$, $\theta_{s,0}(t) \equiv 0$ and $\theta_{s,M}(t) \equiv \theta_\alpha$ yields approximations $\theta_{h_l}(z, t)$ and $\theta_{h_s}(z, t)$ that satisfy the Dirichlet boundary conditions at the interface and at $z = z_b$. The computational problem is to obtain the time-dependent coefficients $\theta_{l,j}(t)$ for $j = 0, 1, \dots, N-1$ and $\theta_{s,j}(t)$ for $j = 1, 2, \dots, M-1$. Substituting these approximations in the Galerkin forms for θ_l and θ_s , respectively, and taking the weight functions $v(z, t)$ and $w(z, t)$ to be the hat functions $\varphi_{l,j}$ and $\varphi_{s,j}$, respectively, yields the two systems of equations in matrix form

$$\mathbf{M}_l \frac{d\boldsymbol{\theta}_l}{dt} + \mathbf{N}_l \boldsymbol{\theta}_l = \mathbf{b}_l, \quad (3.24a)$$

$$\mathbf{M}_s \frac{d\boldsymbol{\theta}_s}{dt} + \mathbf{N}_s \boldsymbol{\theta}_s = \mathbf{b}_s, \quad (3.24b)$$

where $\boldsymbol{\theta}_l = (\theta_{l,i})$, $\mathbf{M}_l = (M_{l,ij})$, $\mathbf{N}_l = (N_{l,ij})$, $\mathbf{b}_l = (b_l \ 0 \ \dots \ 0)^T$, $\boldsymbol{\theta}_s = (\theta_{s,i})$, $\mathbf{M}_s = (M_{s,ij})$, $\mathbf{N}_s = (N_{s,ij})$ and $\mathbf{b}_s = (b_{s,i})$.

The nonzero entries of the matrices and the vectors on the right hand side are the following:

$$M_{l,00} = \frac{1}{2} h_l(t), \quad M_{l,i,i} = h_l(t) \quad i = 1, \dots, N-1, \quad (3.25a)$$

$$N_{l,i-1,i} = -\frac{1}{6} \frac{3i-2}{N} \frac{ds}{dt} - \frac{1}{h_l(t)}, \quad (3.25b)$$

$$N_{l,00} = \frac{1}{6N} \frac{ds}{dt} + \frac{1}{h_l(t)}, \quad N_{l,i,i} = \frac{1}{3N} \frac{ds}{dt} + \frac{2}{h_l(t)}, \quad i = 1, \dots, N-1, \quad (3.25c)$$

$$N_{l,i+1} = \frac{1}{6} \frac{3i+2}{N} \frac{ds}{dt} - \frac{1}{h_l(t)}, \quad (3.25d)$$

$$b_{l,0} = \frac{I}{I_{\text{ref}}} \quad (3.25e)$$

$$M_{s,i} = h_s(t), \quad (3.25f)$$

$$N_{s,i-1} = -\frac{1}{6} \frac{3M-3i+2}{M} \frac{ds}{dt} - \frac{1}{h_s(t)} \quad (3.25g)$$

$$N_{s,i} = -\frac{1}{3M} \frac{ds}{dt} + \frac{2}{h_s(t)}, \quad (3.25h)$$

$$N_{s,i+1} = \frac{1}{6} \frac{3M-3i-2}{M} \frac{ds}{dt} - \frac{1}{h_s(t)} \quad (3.25i)$$

$$b_{s,M-1} = T_a \left(\frac{1}{3M} \frac{ds}{dt} + \frac{1}{h_s(t)} \right). \quad (3.25j)$$

On the mass matrices \mathbf{M}_l and \mathbf{M}_s lumping is performed. Note that lumping is $\mathcal{O}(h^2)$ and therefore does not affect the order.

The Stefan condition in (3.16) can be approximated by

$$-\lambda_f \frac{ds}{dt} = \left\{ \sum_{j=0}^{N-1} \theta_{l,j}(t) \left. \frac{\partial \varphi_{l,j}}{\partial z} \right|_{z \uparrow s} - \sum_{j=1}^{M-1} \theta_{s,j}(t) \left. \frac{\partial \varphi_{s,j}}{\partial z} \right|_{z \downarrow s} \right\}. \quad (3.26)$$

Using the properties of the hat functions this simplifies to

$$\frac{ds}{dt} = \frac{1}{\lambda_f} \left\{ \frac{1}{h_l(t)} \theta_{l,N-1}(t) + \frac{1}{h_s(t)} \theta_{s,1}(t) \right\}. \quad (3.27)$$

Thus, the problem (3.16) has been changed to the system of initial-value problems comprising (3.24) and (3.27), with suitable initial conditions. Note that this derivation for two-dimensional problem is not this straightforward because of the Stefan condition.

The discretisation of the time derivatives in (3.24) and (3.27) will be done by the ϑ -method. We will outline the procedure for Euler forward (EF) for the boundary and a ϑ -method for the temperature distributions in the following.

Assume the temperature distributions and the position of the solid-liquid interface are known at time level $t = t^k$. We denote these by θ_l^k , θ_s^k and s^k , respectively. Here $t^k = k\Delta t$, where Δt is the time step. Then, we compute s^{k+1} through the EF-discretized version of (3.27)

$$s^{k+1} = s^k + \frac{\Delta t}{\lambda_f} \left\{ \frac{1}{h_l(t^k)} \theta_{l,N-1}^k + \frac{1}{h_s(t^k)} \theta_{s,1}^k \right\}. \quad (3.28)$$

Now the new mesh can be computed using (3.19) and (3.20). The temperature distributions at time $t = t^{k+1}$ are now computed via the solution of the discretized versions of the matrix equations (3.24).

$$\begin{aligned} \left(\mathbf{I} + \vartheta \Delta t (\mathbf{M}_l^{k+1})^{-1} \mathbf{N}_l^{k+1} \right) \boldsymbol{\theta}_l^{k+1} = \\ \left(\mathbf{I} - (1 - \vartheta) \Delta t (\mathbf{M}_l^k)^{-1} \mathbf{N}_l^k \right) \boldsymbol{\theta}_l^k + \Delta t \left(\vartheta (\mathbf{M}_l^{k+1})^{-1} + (1 - \vartheta) (\mathbf{M}_l^k)^{-1} \right) \mathbf{b}_l \end{aligned} \quad (3.29a)$$

and

$$\begin{aligned} \left(\mathbf{I} + \vartheta \Delta t (\mathbf{M}_s^{k+1})^{-1} \mathbf{N}_s^{k+1} \right) \boldsymbol{\theta}_s^{k+1} = \\ \left(\mathbf{I} - (1 - \vartheta) \Delta t (\mathbf{M}_s^k)^{-1} \mathbf{N}_s^k \right) \boldsymbol{\theta}_s^k + \Delta t \left(\vartheta (\mathbf{M}_s^{k+1})^{-1} \mathbf{b}_s^{k+1} + (1 - \vartheta) (\mathbf{M}_s^k)^{-1} \mathbf{b}_s^k \right) \end{aligned} \quad (3.29b)$$

where the superscripts in the matrix notations denote the time level at which they are evaluated. We know that for $\vartheta = \frac{1}{2}$ (Crank-Nicolson) the time stepping is $\mathcal{O}(\Delta t^2)$.

3.2.2 Finding suitable initial conditions

The major problem that remains is to find suitable initial conditions. This problem will be addressed below by looking at the premelting problem.

In the heating-up stage, the temperature θ in the material is governed by

$$\frac{\partial \theta}{\partial t} = \frac{\partial^2 \theta}{\partial z^2}, \quad z > 0. \quad (3.30)$$

The (dimensionless) energy, which we denote by F , is supplied at the surface:

$$\frac{\partial \theta}{\partial z} = -F, \quad z = 0, \quad (3.31)$$

and we assume an ambient temperature both at infinity

$$\theta \rightarrow \theta_\alpha, \quad z \rightarrow \infty, \quad (3.32)$$

as well as initially

$$\theta = \theta_\alpha, \quad t = 0. \quad (3.33)$$

We can find the analytical solution to (3.30)-(3.33) using Laplace transformations. This yields

$$\theta(z, t) = F \left\{ 2 \left(\frac{t}{\pi} \right)^{\frac{1}{2}} \exp \left(-\frac{z^2}{4t} \right) - z \operatorname{erfc} \left(\frac{z}{2t^{\frac{1}{2}}} \right) \right\} + \theta_\alpha. \quad (3.34)$$

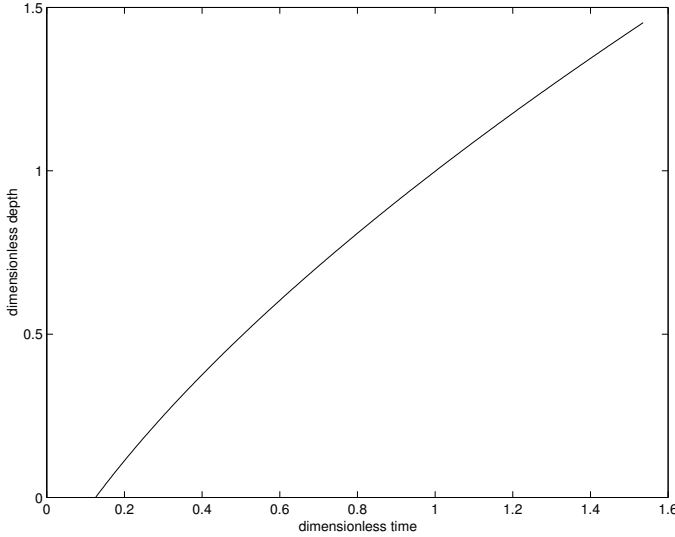


Figure 3.3: The position of the solid-liquid interface where the absorption of latent heat is neglected for the case of aluminium.

Therefore, when latent heat is neglected, the position s of the solid-liquid interface is found from

$$\frac{I}{I_{\text{ref}}} \left\{ 2 \left(\frac{t}{\pi} \right)^{\frac{1}{2}} \exp \left(-\frac{s^2}{4t} \right) - s \operatorname{erfc} \left(\frac{s}{2t^{\frac{1}{2}}} \right) \right\} + \theta_a = 0, \quad (3.35)$$

for all t . In Figure 3.3 this position is sketched for aluminium. This yields the right initial value of $\frac{ds}{dt}$. From this we compute $s(\Delta t)$ by an EF step. Furthermore, from (3.34) it follows that at time $t = t_m$, with

$$t_m = \frac{I_{\text{ref}}^2 \theta_a^2 \pi}{4I^2}, \quad (3.36)$$

the surface starts to melt.

Now we need initial conditions for the temperature distributions. From the Stefan condition (3.16) it follows that

$$\frac{\partial \theta_s}{\partial z} \Big|_{z \downarrow s} = \lambda_f \frac{ds}{dt} - \frac{\partial \theta_l}{\partial z} \Big|_{z \uparrow s} \approx \lambda_f \frac{ds}{dt} - \frac{I}{I_{\text{ref}}}, \quad (3.37)$$

for s small. Therefore we let

$$\theta_{s,j}(\Delta t) = |\theta_a| \exp \left(-\frac{(z_{s,j} - s)^2 F^2}{\theta_a^2 \pi} \right) - F(z_{s,j} - s) \operatorname{erfc} \left(\frac{(z_{s,j} - s)F}{|\theta_a| \sqrt{\pi}} \right) + \theta_a, \quad j = 1, \dots, M-1, \quad (3.38)$$

be the initial temperature distribution in the solid at time level $t = \Delta t$ to our computational problem as sketched in Section 3.2.1, where

$$F = \frac{I}{I_{\text{ref}}} - \lambda_f \frac{ds}{dt}. \quad (3.39)$$

Because $s(\Delta t)$ is small, we take the temperature distribution in the liquid at time level $t = \Delta t$ to be linear

$$\theta_{1,j}(\Delta t) = \frac{I}{I_{\text{ref}}} (s - z_{1,j}), \quad j = 0, \dots, N-1, \quad (3.40)$$

satisfying the boundary conditions at $z = 0$ and $z = s$.

Note that this approach cannot easily be extended to cover problems with variable energy supply.

Now, our numerical method to obtain the depth of the melt pool generated by the laser is solvable.

3.2.3 Discretisation of the Enthalpy Problem

A discretisation of the enthalpy method in one spatial dimension which uses finite differences is described in Tacke [44]. However, the extension of this model to two spatial dimensions is very hard and becomes even harder when moving boundaries (as in the solidification problem) come up. The finite element method again looks promising to handle these kind of problems.

Again, the derivation of the finite element method consists of the following steps: (i) a Galerkin formulation, (ii) a discretizing method and (iii) the solution of the resulting initial value problems with suitable initial conditions.

The problem to begin with is comprised by (3.12)-(3.15) and Eq. (3.8) or (3.10). Again, the domain is bounded at $z = z_b$ and we let $\Omega = (0, z_b)$. We search for a weak solution by solving

$$\int_{\Omega} \frac{\partial \eta}{\partial t} v dz = \frac{I}{I_{\text{ref}}} v(0) - \int_{\Omega} \frac{\partial \theta}{\partial z} \frac{\partial v}{\partial z} dz, \quad (3.41)$$

together with the relationship between η and θ as expressed in Eq. (3.8) or (3.10).

To solve this Galerkin form, we compute approximate solutions of the temperature and enthalpy distributions, from which the position of the solid-liquid interface then follows a posteriori. First we fix the time t and divide the domain $0 \leq z \leq z_b$ into N subintervals. At each node in this domain we construct the hat function $\varphi_i(z)$. Next we determine approximate solutions of the forms

$$\tilde{\eta}(z, t) = \sum_{i=0}^N \eta_i(t) \varphi_i(z), \quad \tilde{\theta}(z, t) = \sum_{i=0}^N \theta_i(t) \varphi_i(z). \quad (3.42)$$

Letting $\eta_N(t) \equiv \eta(\theta_a)$ and $\theta_N(t) \equiv \theta_a$ takes care of the ambient conditions at $z = z_b$. The computational problem is to obtain the time-dependent coefficients $\eta_i(t)$ and $\theta_i(t)$ for $i = 0, \dots, N-1$. Substituting the approximations into the Galerkin form and taking the weight function $v(z)$ to be the hat functions $\varphi_j(z)$ for $j = 0, \dots, N-1$, we obtain the set of equations in matrix form:

$$\mathbf{M} \frac{d\boldsymbol{\eta}}{dt} = \mathbf{b} - \mathbf{N}\boldsymbol{\theta}. \quad (3.43)$$

Here, $\boldsymbol{\eta} = (\eta_0(t), \dots, \eta_{N-1}(t))^T$ and $\boldsymbol{\theta} = (\theta_0(t), \dots, \theta_{N-1}(t))^T$. The entries of the matrices and vector are given by

$$M_{ij} = \int_0^{z_b} \varphi_i \varphi_j dz, \quad i, j = 0, \dots, N-1, \quad (3.44a)$$

$$b_j = \frac{I}{I_{\text{ref}}} \varphi_j(0) - T_a \int_0^{z_b} \frac{d\varphi_N}{dz} \frac{d\varphi_j}{dz} dz, \quad j = 0, \dots, N-1, \quad (3.44b)$$

$$N_{ij} = \int_0^{z_b} \frac{d\varphi_i}{dz} \frac{d\varphi_j}{dz} dz, \quad i, j = 0, \dots, N-1. \quad (3.44c)$$

Thus, we have a set of initial value problems which, together with the relationship between enthalpy and temperature, can be solved numerically.

In order to show how we solve (3.43) by the ϑ -method, we rewrite (3.43) as

$$\mathbf{M} \frac{d\boldsymbol{\eta}}{dt} = \mathcal{F}(\boldsymbol{\eta}, t) := \mathbf{b}(t) - \mathbf{N}\boldsymbol{\theta}(\boldsymbol{\eta}). \quad (3.45)$$

The enthalpy and temperature distributions in the material at time $t = t^{k+1}$ are then computed by the ϑ -method. We obtain

$$\mathcal{G}(\boldsymbol{\eta}^{k+1}) := \mathbf{M}(\boldsymbol{\eta}^{k+1} - \boldsymbol{\eta}^k) - \Delta t (\vartheta \mathcal{F}(\boldsymbol{\eta}^{k+1}, t^{k+1}) + (1 - \vartheta) \mathcal{F}(\boldsymbol{\eta}^k, t^k)) = \mathbf{0}. \quad (3.46)$$

This system can be solved together with the pointwise relationship of enthalpy and temperature as in (3.8) or (3.10).

For $\vartheta = 0$ the procedure is simply the following. Compute the enthalpy distribution in the material at time $t = t^{k+1}$ via

$$\mathbf{M}\boldsymbol{\eta}^{k+1} = \mathbf{M}\boldsymbol{\eta}^k + \Delta t \mathcal{F}(\boldsymbol{\eta}^k, t^k), \quad (3.47)$$

and then update the temperature via the inverse relation of (3.8) or (3.10) to get

$$\theta_i^{k+1} = \theta(\eta_i^{k+1}). \quad (3.48)$$

We note that this discretisation converges to the weak solution for ordinary Stefan problems, see e.g. Elliot and Ockendon [15].

Choosing a $\vartheta \neq 0$ will lead to a system of nonlinear algebraic equations which can be solved by Newton's method. The iteration to obtain the solution at $t = t^{k+1}$ is as follows

$$\begin{cases} \eta^{k+1,l} = \eta^{k+1,l-1} - (\partial \mathcal{G}(\eta^{k+1,l-1}))^{-1} \mathcal{G}(\eta^{k+1,l-1}), & l = 1, 2, \dots, \\ \eta^{k+1,0} = \eta^k. \end{cases} \quad (3.49)$$

Here, the notation $\partial \mathcal{G}(\eta)$ denotes the Jacobian of $\mathcal{G}(\eta)$ and is given by

$$\partial \mathcal{G}(\eta) = \mathbf{M} + \Delta t \vartheta \mathbf{N} \frac{\partial \theta}{\partial \eta}(\eta). \quad (3.50)$$

The iteration in (3.49) is stopped if a given accuracy is reached.

In this time-stepping algorithm we will begin with an initial solution given by the analytical solution (3.34) to the pre-melting problem, as given in the previous subsection. Results will be assessed in Section 3.4.

3.3 Extension to 2D

In the various techniques in modelling the melting for the laser percussion drilling process, we encounter several problems. The main problem is that the splashing and solidification models are essentially 2D. Therefore, our computational model has to cope with that.

The extension to two spatial dimensions is necessary in solving the splashing and solidification models. We will show how this is done by the axisymmetric version of our melting model. The geometry for the formulation using the Stefan condition is sketched in Figure 3.4.

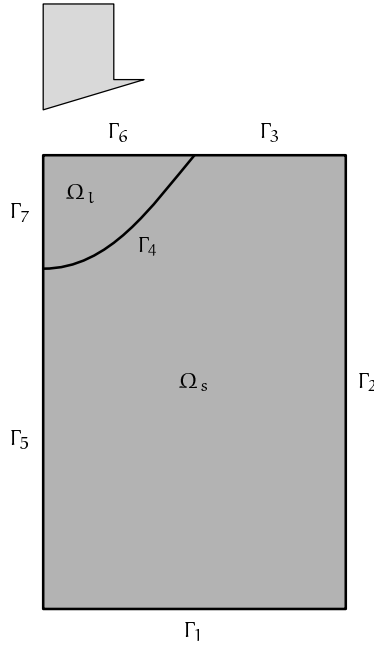


Figure 3.4: The geometry for the Stefan formulation.

The dimensional form of the problem is as follows.

$$\left\{ \begin{array}{ll}
 \rho c \frac{\partial T_i}{\partial t} = \text{div} (k \text{ grad } T_i), & \text{in } \Omega_i, \quad i = s, l, \\
 T_s = T_a, & \text{on } \Gamma_1 \cup \Gamma_2, \\
 k \frac{\partial T_s}{\partial n} = I(r, t), & \text{on } \Gamma_3, \\
 k \frac{\partial T_s}{\partial n} = 0, & \text{on } \Gamma_5, \\
 k \frac{\partial T_l}{\partial n} = I(r, t), & \text{on } \Gamma_6, \\
 k \frac{\partial T_l}{\partial n} = 0, & \text{on } \Gamma_7, \\
 T_s = T_l = T_m, \quad k \frac{\partial T}{\partial n} \Big|_l^s = \rho L_f v_n, & \text{on } \Gamma_4.
 \end{array} \right. \quad (3.51)$$

Here, the normal on Γ_4 points into the solid and v_n is the velocity in normal direction. In this axisymmetric domain, the Stefan condition can be rewritten if we denote the

position of Γ_4 by $z = s(r, t)$. The Stefan condition takes the form, see [33],

$$\left[1 + \left(\frac{\partial s}{\partial r} \right)^2 \right] \left[k \frac{\partial T}{\partial z} \Big|_1^s \right] = \rho L_f \frac{\partial s}{\partial t}. \quad (3.52)$$

The geometry for the enthalpy method is sketched in Figure 3.5.

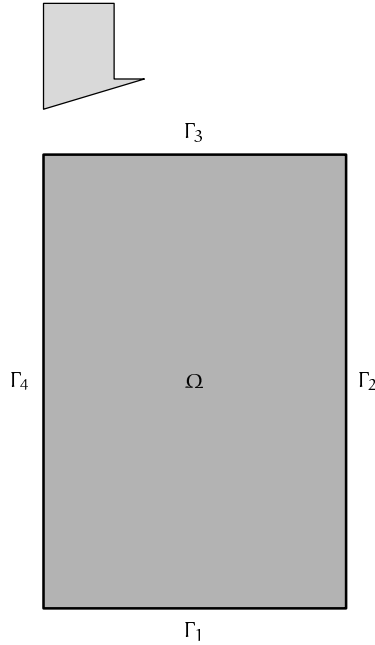


Figure 3.5: *The geometry for the enthalpy method.*

The dimensional form of the problem is now:

$$\left\{ \begin{array}{ll} \frac{\partial H}{\partial t} = \text{div} (k \text{ grad } T), & \text{in } \Omega, \\ T = T_\alpha, & \text{on } \Gamma_1 \cup \Gamma_2, \\ k \frac{\partial T}{\partial n} = I(r, t), & \text{on } \Gamma_3, \\ k \frac{\partial T}{\partial n} = 0, & \text{on } \Gamma_4, \\ T = T_0, & \text{on } t = 0, \end{array} \right. \quad (3.53)$$

together with the relationship between enthalpy and temperature as described in Eq. (3.8) or (3.10).

The numerical procedure of the 2D Stefan formulation is not straightforward because of the difficult interface condition, whereas the numerics of the 2D enthalpy method is a simple extension of the 1D model. This is mainly because of the fact that in the enthalpy method the position of the solid-liquid interface is not needed. Numerical results of the 2D enthalpy method will be presented and discussed in the next section.

3.4 Numerical results and discussion

In this Section we will discuss the results from the numerical models based on FEM for the melting problem as derived in Sections 3.2 and 3.3. The results will be assessed.

Because Eq. (3.27) is already $O(\Delta t)$, we look at the $O(\Delta t)$ time stepping schemes EF and EB. Note that the results for the (explicit) EF-scheme are obtained using variable time steps to ensure the stability of the scheme. For the Stefan condition method, the $(k + 1)$ -th time step Δt^{k+1} is taken to be

$$\Delta t^{k+1} = 0.4 \min((h_l(t^k))^2, (h_s(t^k))^2), \quad (3.54)$$

to ensure that the stability condition

$$\Delta t \leq 0.5h^2 \quad (3.55)$$

holds throughout both regions. Because we need to resolve the temperature in the liquid region h_l will be small and this puts a severe restriction on the time steps used. So if we look at stability, this is in favour of the implicit method. However, for both methods the error is $O(\Delta t) + O(\Delta x^2)$ so to reach the same accuracy we have to take equally small time steps in both methods. In order to get a good estimation for the dimensions of the melt pool, as needed in upcoming splashing and solidification models, we need a high accuracy.

Furthermore, for the explicit method ($\vartheta = 0$), Eqs (3.29) simplify because of the lumped mass matrices. The matrix in front of $\mathbf{T}_{l,s}^{k+1}$ is simply \mathbf{I} . In other words, for this explicit method we do not need to solve a system of equations each time step. The amount of flops to solve a tridiagonal system of n equations is, when one makes use of the sparsity, asymptotically $3n$, see e.g. [8], so here this means an extra amount of calculations of $O(N) + O(M)$. From this we see that the total balance therefore is in favour of using explicit methods after all.

Because the position of the solid-liquid interface is not needed explicitly in the enthalpy method, the restriction on the time step to be used in the enthalpy method is somewhat less severe. The time step Δt (which is constant now) can taken to be

$$\Delta t = 0.4h^2. \quad (3.56)$$

The results for the EB-scheme for $\Delta t = 0.01$ are shown in Figures 3.6 to 3.8. In Fig-

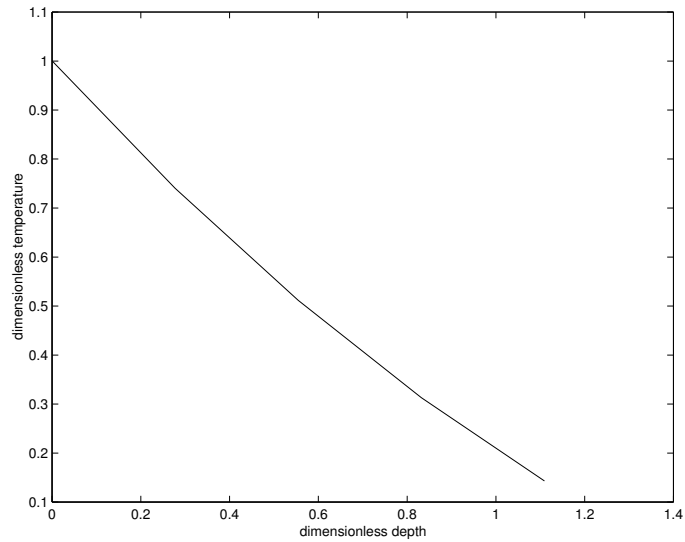


Figure 3.6: *The temperature distribution in the liquid part at the time at which the surface reaches vaporisation temperature.*

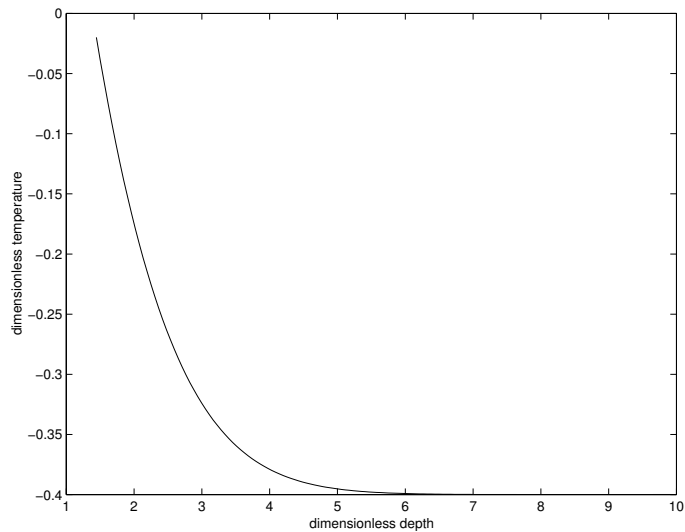


Figure 3.7: *The temperature distribution in the solid part at the time at which the surface reaches vaporisation temperature.*

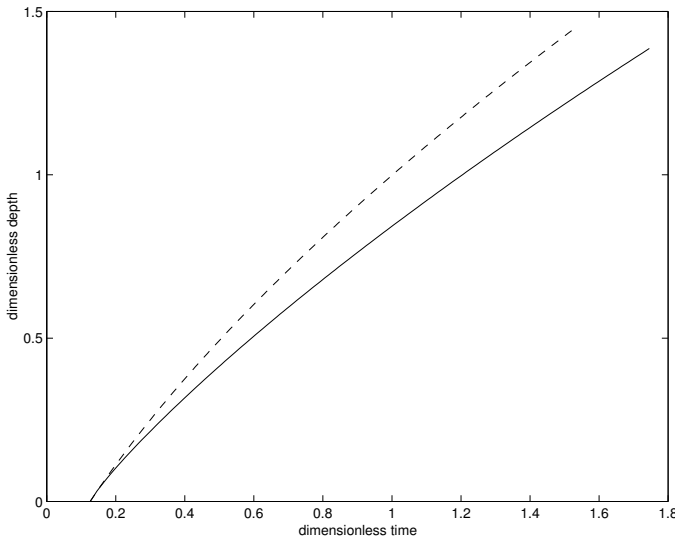


Figure 3.8: *The position of the solid-liquid interface. The numerical (with latent heat) position is denoted by the solid line, whereas the analytical (without latent heat) position is denoted by the dashed line.*

ures 3.6 and 3.7 the temperatures in the liquid and the solid are shown, respectively, at the time at which the surface reaches vaporisation temperature. Figure 3.8 shows the evolution of the solid-liquid boundary. Here, the analytical solution in case of latent heat is included as a reference to show its influence.

In Figure 3.9 the results for the two-dimensional model as derived in the previous section are given compared to the results of the one dimensional analysis. The intensity profile $I(r, t)$ is assumed to be a Gaussian TEM₀₀-mode, constant in time. It is shown that the results for the one-dimensional model indeed give an almost identical estimate of the dimensions of the melt pool.

If no phase change occurs, the numerics derived from the enthalpy problem are satisfactory. For phase change problems, it is correct on average, since heat balances are fulfilled throughout. However, calculated positions of the solid-liquid interface and temperature and enthalpy oscillate with a period corresponding to the time the interface needs to travel through a certain element. This phenomenon can be seen in Figure 3.10. The plateau generated propagates to adjacent elements and smooths out only after the solid-liquid interface has travelled a sufficient distance from the point under consideration.

This staircase-like behaviour has its cause in comparing average enthalpies per element with nodal temperatures. In problems in one spatial dimension this can be overcome by an approach as suggested by Tacke [44]. This method works fairly good, but can't be extended to higher dimensional problems. Another solution is to

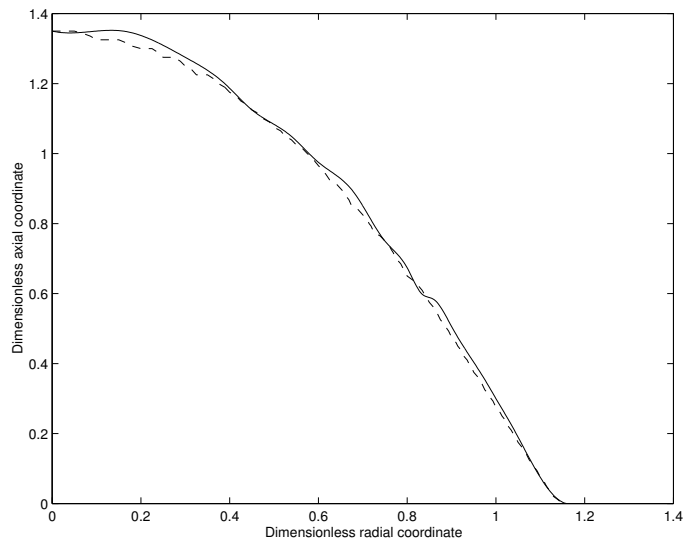


Figure 3.9: *The front at the time at which the surface in the origin reaches vaporization temperature. The one dimensional result is denoted by the solid line, whereas the result of the full two dimensional model is denoted by the dashed line.*

use a finer grid near the front, the advantage of this is that it is easily extended to higher dimensions. This is an important consideration in view of the splashing and solidification models, see Smith [41].

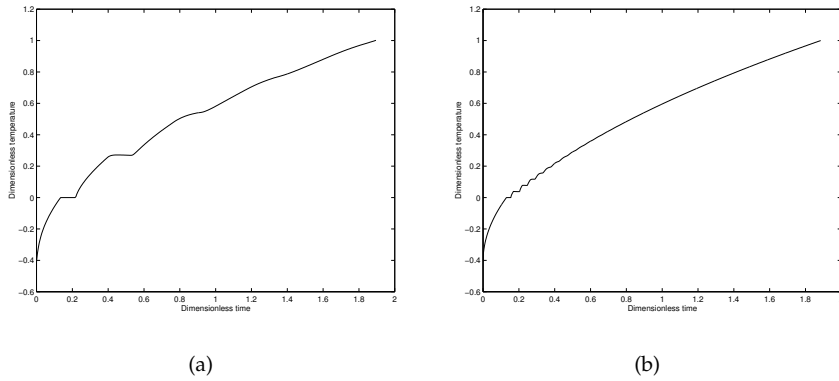


Figure 3.10: Time history plots for temperature in enthalpy problem for (a) 20 elements and (b) for 150.

The effect of the laser beam

In this chapter we consider how the laser beam influences the laser drilling process. We might be able to improve the process by selecting the laser with certain beneficial properties. In order to get an idea of these parameters we can play with, we study them in this chapter. Because the material reflects the incoming laser light to some extent, the reflections of the incoming beam may play a major role in the geometry of the drilled hole. This will be studied and modelled in Section 4.1. Section 4.2 reveals the influence of wavelength and peak intensity to the process. In Sections 4.3 and 4.4 the importance of spatial and temporal pulse shapes of the incident laser beam, respectively, is assessed. Finally, in Section 4.5 an entire drilling simulation consisting of several pulses is performed for one specific set-up of the Nd:YAG laser.

4.1 Reflections of the incoming beam

The knowledge that metals tend to reflect a lot of incoming light dates back to remote antiquity. Early mirrors were made of polished copper and bronze and the word specular originates from *speculum*, a copper alloy rich in tin. Because of this high reflectance of metals, the reflections of the incoming beam play an important role in the resulting hole geometry and therefore have to be taken into account. Because of reflections the actual intensity distribution at the surface of the material may turn out to be quite different than expected. And it is this actual intensity distribution at the surface that is most vital to the outcome of the laser percussion drilling process. In this section we use the Algebraic Ray Trace Method (ARTM), see [45], to find this resulting intensity distribution. The ARTM is implemented and the results for different settings of both laser and geometry are shown.

4.1.1 Background

The parts of the energy of an incoming laser beam that are reflected and absorbed depend on its angle of incidence θ_i , see Figure 4.1. It is exactly this dependence that makes reflection important. When a ray \mathbf{s}_i reaches a material, it is partially reflected

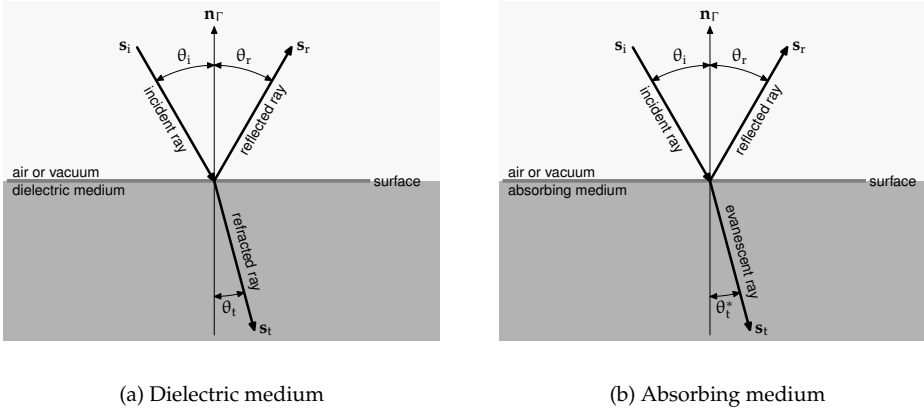


Figure 4.1: Refraction and reflection of radiation at the surface of (a) a dielectric and (b) an absorbing medium.

as \mathbf{s}_r and partially refracted as \mathbf{s}_t , see Figure 4.1. Huygens' law of reflection states that the reflected direction follows the specular reflection defined as:

$$\mathbf{s}_r = \mathbf{s}_i - 2(\mathbf{n}_r \cdot \mathbf{s}_i)\mathbf{n}_r. \quad (4.1)$$

For incidence in air or vacuum on a dielectric we have Snell's Law, which states that

$$\frac{\sin \theta_t}{\sin \theta_i} = \frac{1}{n}, \quad (4.2)$$

where θ_i and θ_t are the angles as defined in Figure 4.1(a) and n is the simple index of refraction of the dielectric medium. For absorbing media such as metals, however, we need to use the complex index of refraction defined by

$$\tilde{n} = n - ik, \quad (4.3)$$

where n is the simple index of refraction, k the extinction coefficient. The simple index of refraction and the extinction coefficient depend on material properties and on the wavelength of the incoming wave in vacuum, λ_0 say. This dependence follows from Maxwell's equations and is given by [38, p. 101]

$$n^2 = \frac{\mu\gamma c_0^2}{2} \left\{ 1 + \left[1 + \left(\frac{\lambda_0}{2\pi c_0 r_e \gamma} \right)^2 \right]^{\frac{1}{2}} \right\} \quad (4.4a)$$

and

$$k^2 = \frac{\mu\gamma c_0^2}{2} \left\{ -1 + \left[1 + \left(\frac{\lambda_0}{2\pi c_0 r_e \gamma} \right)^2 \right]^{\frac{1}{2}} \right\}, \quad (4.4b)$$

respectively. Here, c_0 the speed of the electromagnetic wave in vacuum. Furthermore, μ , γ and r_e are respectively the magnetic permeability, the electrical permittivity and the electrical resistivity of the material. A good recent source of property values for n and k is [32], containing extensive information for metals. For a ray incident in air or vacuum on a metal, Snell's law becomes

$$\frac{\sin \theta_t}{\sin \theta_i} = \frac{1}{\tilde{n}}. \quad (4.5)$$

As a consequence, $\sin \theta_t$ is complex, and the angle θ_t can no longer be interpreted physically as a simple angle of refraction for propagation into the material. Except for the special case of normal incidence, n is no longer directly related to the propagation velocity. The actual angle of refraction θ_t^* , see Fig. 4.1(b), can still be calculated from \tilde{n} and θ_i , albeit no longer via Snell's law, see e.g. [38, pp. 109–110]. Note that the refracted ray is strongly attenuated in metals as is evident from their exceedingly small penetration depths (order of nanometers). This justifies the treatment of the laser beam as a 'boundary' source instead of a 'volume' source in the mathematical models. A wave that is attenuated as it travels through a medium is called *evanescent*.

The *Fresnel equations*, see e.g. [5, 21, 38], relate the amplitude of the incoming wave with the amplitudes of the reflected and the refracted waves, and, furthermore, do so for both perpendicularly and parallelly polarised waves. We consider radiation incident in air or vacuum on a material with properties n and k . For the case where the \mathbf{E} -field is perpendicular to the plane of incidence, the *amplitude reflection coefficient* is given by

$$\left(\frac{E_{0r}}{E_{0i}} \right)_{\perp} = \frac{\cos \theta_i - \tilde{n} \cos \theta_t}{\cos \theta_i + \tilde{n} \cos \theta_t}, \quad (4.6)$$

and when the \mathbf{E} -field is parallel to the plane of incidence by

$$\left(\frac{E_{0r}}{E_{0i}} \right)_{\parallel} = \frac{\tilde{n} \cos \theta_i - \cos \theta_t}{\tilde{n} \cos \theta_i + \cos \theta_t}. \quad (4.7)$$

Note that for metals these coefficients are complex. For the special case of normal incidence, from Eqs. (4.6) and (4.7) we obtain, using Snell's law (4.5),

$$\left(\frac{E_{0r}}{E_{0i}} \right)_{\perp} = - \left(\frac{E_{0r}}{E_{0i}} \right)_{\parallel} = \frac{1 - \tilde{n}}{1 + \tilde{n}}. \quad (4.8)$$

The *directional reflectivity* of a material $\rho(\lambda, \theta_i)$ is defined as the ratio of the reflected to the incident intensity of an incoming wave, yielding

$$\rho(\lambda, \theta_i) = \frac{I_r}{I_i}. \quad (4.9)$$

The reflectivity depends on the wavelength λ through the index of refraction and on the angle of incidence θ_i . The portion, A say, of the incident wave that is actually absorbed by the metal is then simply

$$A(\lambda, \theta_i) := 1 - \rho(\lambda, \theta_i). \quad (4.10)$$

The reflectivity $\rho(\lambda, \theta_i)$ can be expressed in terms of the amplitude reflection coefficients

$$\rho_{\perp}(\lambda, \theta_i) = \left| \left(\frac{E_{0r}}{E_{0i}} \right)_{\perp} \right|^2 = \left(\frac{E_{0r}}{E_{0i}} \right)_{\perp} \overline{\left(\frac{E_{0r}}{E_{0i}} \right)_{\perp}} \quad (4.11a)$$

and

$$\rho_{\parallel}(\lambda, \theta_i) = \left| \left(\frac{E_{0r}}{E_{0i}} \right)_{\parallel} \right|^2 = \left(\frac{E_{0r}}{E_{0i}} \right)_{\parallel} \overline{\left(\frac{E_{0r}}{E_{0i}} \right)_{\parallel}}, \quad (4.11b)$$

where \bar{z} is the complex conjugate of z .

For an unpolarized beam we have,

$$\rho(\lambda, \theta_i) = \frac{\rho_{\perp}(\lambda, \theta_i) + \rho_{\parallel}(\lambda, \theta_i)}{2}. \quad (4.12)$$

Because the relations for the two polarization directions are the same for normal incidence, the reflectivity for normal incidence follows from (4.8) and is given by

$$\rho(\lambda, 0) = \rho_{\perp}(\lambda, 0) = \rho_{\parallel}(\lambda, 0) = \frac{(n-1)^2 + k^2}{(n+1)^2 + k^2}. \quad (4.13)$$

The reflectivities for oblique incidence can be found by substituting (4.6) and (4.7) into (4.11). A more convenient way to present the results is to use the method of *effective indices* to calculate $\rho_{\perp}(\lambda, \theta_i)$ and $\rho_{\parallel}(\lambda, \theta_i)$, see e.g. [5, 14].

In air or vacuum the effective indices $\eta_{i\perp}$ and $\eta_{i\parallel}$ for the perpendicular and parallel components are defined by

$$\eta_{i\perp} := \cos \theta_i, \quad (4.14a)$$

$$\eta_{i\parallel} := \frac{1}{\cos \theta_i}, \quad (4.14b)$$

respectively. In the absorbing material $\eta_{t\perp}$ and $\eta_{t\parallel}$ are complex and are defined by

$$\eta_{t\perp} := \tilde{n} \cos \theta_t, \quad (4.15a)$$

$$\eta_{t\parallel} := \frac{\tilde{n}}{\cos \theta_t}. \quad (4.15b)$$

Here

$$\cos \theta_t = \left(\frac{(\alpha^2 + \beta^2)^{1/2} + \alpha}{2} \right)^{\frac{1}{2}} - i \left(\frac{(\alpha^2 + \beta^2)^{1/2} - \alpha}{2} \right)^{\frac{1}{2}}, \quad (4.16a)$$

with

$$\alpha := 1 + \left(\frac{\sin \theta_i}{n^2 + k^2} \right)^2 (k^2 - n^2) \quad (4.16b)$$

and

$$\beta := -2nk \left(\frac{\sin \theta_i}{n^2 + k^2} \right)^2. \quad (4.16c)$$

Using these effective indices the amplitude reflection coefficients are given by

$$\left(\frac{E_{0r}}{E_{0i}} \right)_{\perp} = \frac{\eta_{i\perp} - \eta_{t\perp}}{\eta_{i\perp} + \eta_{t\perp}}, \quad (4.17a)$$

and

$$\left(\frac{E_{0r}}{E_{0i}} \right)_{\parallel} = \frac{\eta_{i\parallel} - \eta_{t\parallel}}{\eta_{i\parallel} + \eta_{t\parallel}}. \quad (4.17b)$$

The reflectivities can now be obtained using (4.11). Another form of these reflectivity equations is given in [38],

$$\rho_{\perp}(\lambda, \theta_i) = \frac{(n\beta - \cos \theta_i)^2 + (n^2 + k^2)\alpha - n^2\beta^2}{(n\beta + \cos \theta_i)^2 + (n^2 + k^2)\alpha - n^2\beta^2} \quad (4.18a)$$

$$\rho_{\parallel}(\lambda, \theta_i) = \frac{(n\gamma - \alpha/\cos \theta_i)^2 + (n^2 + k^2)\alpha - n^2\gamma^2}{(n\gamma + \alpha/\cos \theta_i)^2 + (n^2 + k^2)\alpha - n^2\gamma^2}, \quad (4.18b)$$

where now

$$\alpha^2 := \left(1 + \frac{\sin^2 \theta_i}{n^2 + k^2} \right)^2 - \frac{4n^2}{n^2 + k^2} \left(\frac{\sin^2 \theta_i}{n^2 + k^2} \right),$$

$$\beta^2 := \frac{n^2 + k^2}{2n^2} \left(\frac{n^2 - k^2}{n^2 + k^2} - \frac{\sin^2 \theta_i}{n^2 + k^2} + \alpha \right)$$

and

$$\gamma := \frac{n^2 - k^2}{n^2 + k^2} \beta + \frac{2nk}{n^2 + k^2} \left(\frac{n^2 + k^2}{n^2} \alpha - \beta^2 \right)^{\frac{1}{2}}.$$

Figure 4.2 shows a typical distribution of the directional reflectivity of absorbing media as a function of the angle of incidence, for light waves polarised perpendicularly or parallelly to the irradiated surface. Note the importance of the polarisation on the reflectivity. The actual reflectivity of an incoming ray is the weighed sum of the reflectivities of the perpendicular and the parallel parts and for an unpolarized beam given by (4.12). At steep sides almost all incoming energy is reflected; so if the hole exhibits some tapering, this tapering is reinforced by reflection of incoming radiation. This phenomenon is known as *channeling*. To be more general: the distribution of irradiation at the surface is strongly influenced by reflections.

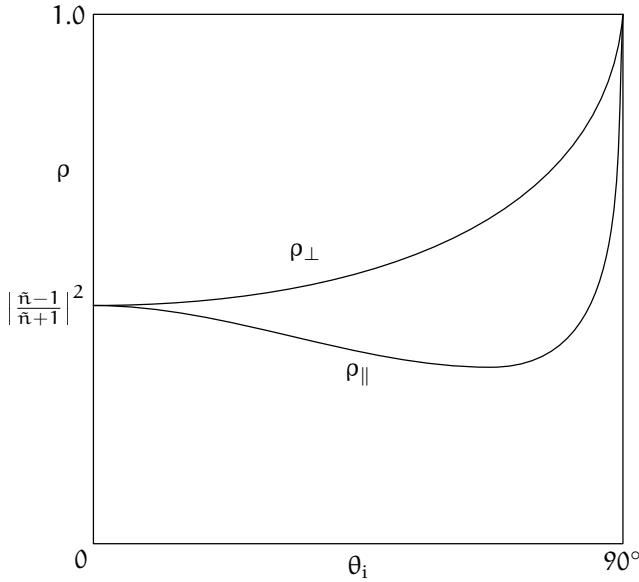


Figure 4.2: Typical reflectivity for a linearly polarized beam incident on an absorbing medium.

4.1.2 Computational method

The problem to solve is the following: given the intensity distribution supplied by the laser and the geometry of the surface it is irradiating, compute the actual flux of energy at this surface. The method that we use to solve this, is the Algebraic Ray Trace Method (ARTM), derived and described in detail in [45]. We tailor this method to employ it for our purpose. This is outlined below.

As in the previous chapters, the laser beam is assumed to be axisymmetric and for the time being the vapour is assumed not to absorb any energy nor to scatter the beam. The virtue of the ARTM is that eventual absorption and defraction of the laser beam within the vapour cloud in between the laser exit and the metal surface can be included easily. The method requires four groups of input:

The geometry The geometry of the computational problem actually consists of three parts, (i) the surface of the irradiated metal, (ii) the boundary on which the laser input is given and (iii) a closure, shown schematically in Fig. 4.3(a). These parts will be denoted by Γ_s , Γ_i and Γ_c , respectively, and we define $\Gamma := \Gamma_s \cup \Gamma_i \cup \Gamma_c$. Although we will take advantage of the fact that the beam is axisymmetric, the geometry is 3D, as in Fig. 4.3(b), because the discrete direction set is 3D. We will call the mesh $\mathcal{M} := \{x_i | i = 1, 2, \dots, M\}$ in the following.

The intensity distribution The intensity that the laser supplies for every direction is given on a certain boundary.

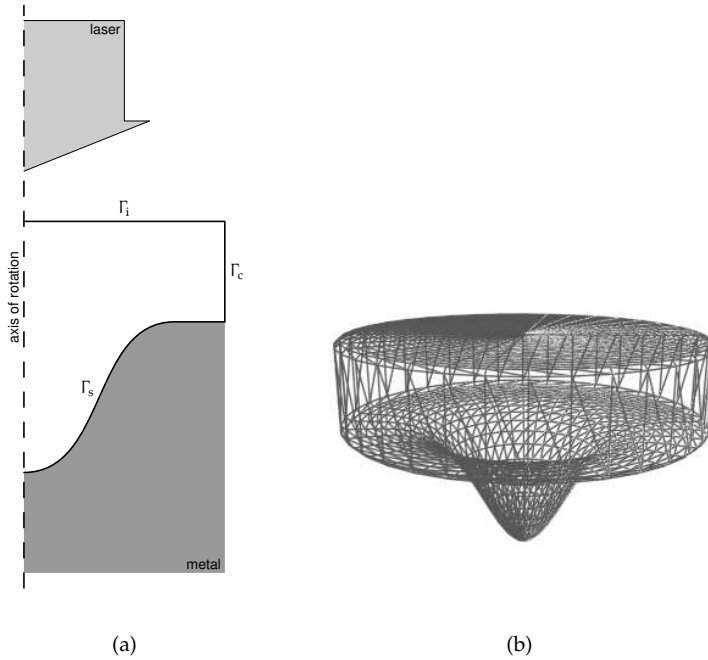


Figure 4.3: *The geometry of the computational problem for the ARTM. Schematically in (a) and an example in (b).*

A discrete direction set To limit the number of directions to a finite set $\mathcal{S} := \{\mathbf{s}_i | i = 1, 2, \dots, N\}$, we use the Discrete Ordinate Method (DOM), see [45]. The influx of energy is given in terms of this discrete set.

The reflectivity The optical behaviour of the metal under irradiation is governed by the Fresnel equations. Furthermore, the index of refraction is a function of the wavelength governed by (4.4). Complicating things further, phase of the material and even temperature affect reflectivity behaviour. The latter is not taken into account here, because there is not much data on this.

Given these four data structures, the ARTM builds the system of equations that describes the resulting irradiation at the surface of the material in terms of the intensities. This can on its turn be used as input for the simulation model. The procedure is outlined below.

The intensity has to be discretized twice: a discretization in terms of the discrete direction set, and a spatial discretization on the underlying grid. Because of the assumption that the vapour is transparent, the mesh only consists of points on the boundary, in contrast to the ARTM described in [45]. The discrete intensity is defined

as

$$h_{ij} := I(\mathbf{x}_j, \mathbf{s}_i), \quad (4.19)$$

with $\mathbf{x}_j \in \mathcal{M}$ and $\mathbf{s}_i \in \mathcal{S}$. We follow a ray starting at \mathbf{x}_j back in direction $-\mathbf{s}_i$ until the boundary is reached. Quantities related to such a ray are indicated with the superscript ij . In general the intersection with the boundary \mathbf{x}_Γ does not coincide with any of the nodes on the boundary. This means that we have to interpolate to find the proper boundary intensity:

$$I(\mathbf{x}_\Gamma^{ij}, \mathbf{s}_i) \doteq \sum_{m=1}^M v_m^{ij} h_{im}, \quad (4.20)$$

where the interpolation coefficients v_m^{ij} are determined for each ray separately. Through Eq. (4.20) the intensity h_{ij} is related to the intensities at other points. Because there is no absorption within the domain, this simply boils down to

$$h_{ij} = \sum_{m=1}^M v_m^{ij} h_{im}. \quad (4.21)$$

If we furthermore define

$$\sigma_{ikjm} := \delta_{ik} v_m^{ij}, \quad (4.22)$$

where the Kronecker delta is used to make the coefficient σ_{ikjm} operate over all directions, we can rewrite (4.21) into

$$h_{ij} = \sum_{k=1}^N \sum_{m=1}^M \sigma_{ikjm} h_{km}. \quad (4.23)$$

However, this *ray tracing* only holds for the case where rays fall onto the boundary, i.e. the inner product of \mathbf{s}_i and the inward pointing normal \mathbf{n}_j at \mathbf{x}_j is negative. For rays that leave the boundary, i.e. $(\mathbf{s}_i \cdot \mathbf{n}_j) > 0$, another relation has to be used. Then, the intensity h_{ij} is related to two contributions, see Fig. 4.4. First, it is related to the other intensities h_{*j} at point \mathbf{x}_j through reflection equations. Secondly, it is related to a possible prescribed incoming intensity r_{ij} at point \mathbf{x}_j through boundary conditions. This discretized relation is given by

$$h_{ij} = r_{ij} + \rho(\lambda, \theta_k) h_{kj}. \quad (4.24)$$

Here k refers to the direction \mathbf{s}_k related to the i -th direction \mathbf{s}_i by means of Huygens' law (4.1), that is,

$$\mathbf{s}_i = \mathbf{s}_k - 2(\mathbf{n}_j \cdot \mathbf{s}_k) \mathbf{n}_j.$$

Furthermore, $\rho(\lambda, \theta_k)$ is the reflectivity function as derived in the previous section and θ_k is the angle between the incoming direction and the local normal. If this direction is not an element of the DOM, h_{kj} and thereby h_{ij} can be obtained from other

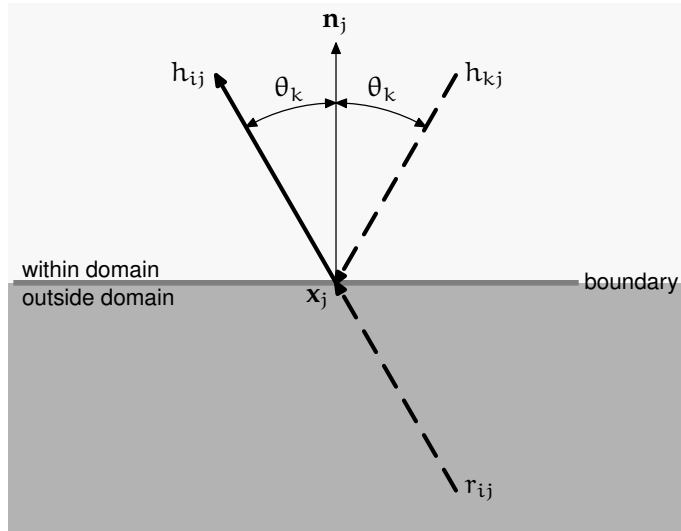


Figure 4.4: The procedure of the ARTM for rays that leave the boundary. The intensity h_{ij} of the ray in the direction \mathbf{s}_i starting from \mathbf{x}_j is related to the possible prescribed incoming intensity r_{ij} and the reflected part of h_{kj} .

directions close to this direction through either interpolation or clipping. Note that within our framework, the incoming intensity is prescribed on Γ_i . Furthermore, the boundaries Γ_i and Γ_c are fictitious and therefore transparent. These two observations lead to

$$\begin{aligned} r_{ij} &= 0, & \text{for } \mathbf{x}_j \in \Gamma_s \cup \Gamma_c, \\ \rho(\lambda, \theta_k) &= 0, & \text{for } \mathbf{x}_j \in \Gamma_i \cup \Gamma_c. \end{aligned}$$

Using a similar strategy as before to make σ_{ikjm} operate over all points, we can rewrite (4.24) to

$$h_{ij} = \sum_{k=1}^N \sum_{m=1}^M \sigma_{ikjm} h_{km} + r_{ij}. \quad (4.25)$$

For simplicity, we rewrite the intensity as a vector \mathbf{h} rather than a tensor, i.e. we place the columns of the tensor below each other. Using this scheme to reorder the tensors σ_{ikjm} into \mathbf{R} and r_{ij} into \mathbf{r} , Eqs. (4.23) and (4.25) are transformed into the system

$$(\mathbf{I} - \mathbf{R})\mathbf{h} = \mathbf{r}. \quad (4.26)$$

Note that half of the coefficients in \mathbf{R} are determined by (4.22) and the other half by (4.24). The precise assembly of the matrix is done as follows. Every ray starts from a node \mathbf{x}_j of the mesh. To find the intensity in direction \mathbf{s}_i , we test whether the inner product of the direction and the inward pointing normal is positive. If this is the case, we have to use the reflection equations to construct the $(N * j + i)$ -th row

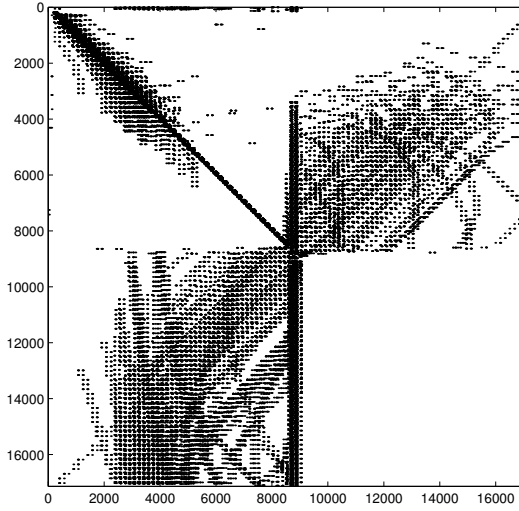


Figure 4.5: Typical plot of the sparsity structure of \mathbf{R} for a grid as in Fig. 4.3(b). The system involves 17,136 unknowns. The number of non-zeros of \mathbf{R} is only 68,418, i.e. 0.2 %.

of \mathbf{R} . Otherwise, we use the ray trace procedure to fill the $(N * j + i)$ -th row of \mathbf{R} . Although the size of \mathbf{R} is large, it is very sparse, see e.g. Fig. 4.5, and sparse solvers can be used to solve (4.26).

However, we are not so much interested in the intensities as such. The intent of this method was to predict the irradiation of the surface. To that end, we need the heat flux \mathbf{q} , which is determined by Fourier's Law:

$$\mathbf{q} = k\nabla T. \quad (4.27)$$

The heat flux \mathbf{q}_j at point \mathbf{x}_j can be found from the intensities h_{*j} as follows

$$\mathbf{q}_j = \sum_{i=1}^N w_i \mathbf{s}_i h_{ij}, \quad (4.28)$$

where the w_i 's are the weights determined by using the DOM. In the end, we are interested in the influx of energy at the boundary and we get

$$\mathbf{n}_j \cdot \mathbf{q}_j = \sum_{i=1}^N w_i (\mathbf{n}_j \cdot \mathbf{s}_i) h_{ij}. \quad (4.29)$$

So, given a geometry, the laser input and the reflectivity behaviour of the material under irradiation, we can compute the actual irradiation distribution on the surface. Some results are presented below.

4.1.3 Results

In this section we present results, obtained using the ARTM as outlined in the previous section, for several geometries and spatial beam profiles. The first results presented here have been obtained using material data of tungsten and $\lambda = 1064$ nm, the wavelength of a Nd:YAG laser. This corresponds to an index of refraction $n = 3.04$ and an extinction coefficient $k = 3.52$, see [42]. These n and k -values lead to a reflectivity of 58% for normal incidence.

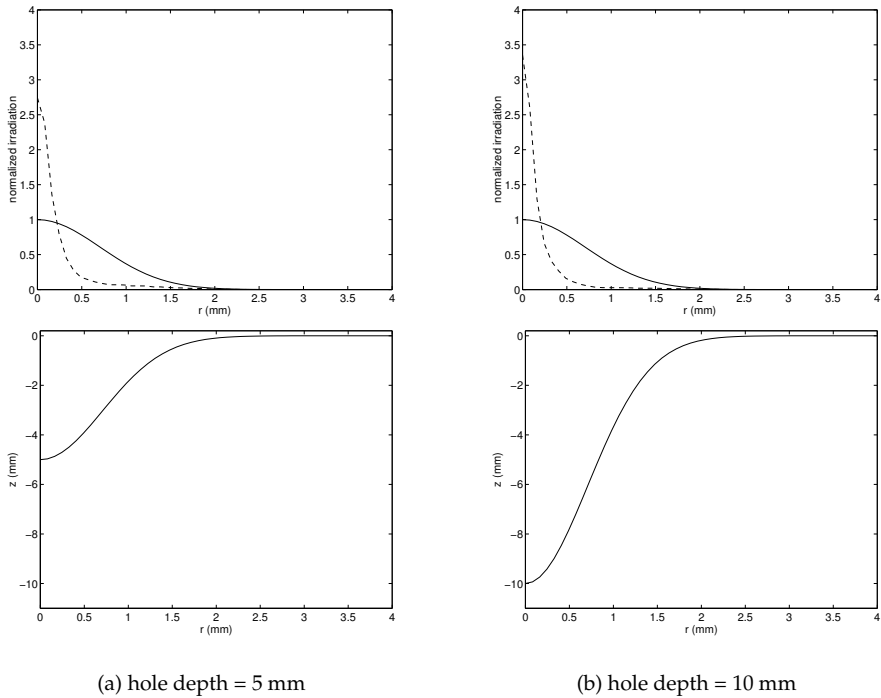


Figure 4.6: Multiple reflection simulation on a Gaussian drill hole surface. The surfaces are shown in the lower figures. The upper figures denote the irradiation. The input irradiation distribution is Gaussian and is denoted by the solid line, the actual distribution of irradiation is depicted by the dashed line.

Fig. 4.6 shows the effect that multiple reflections have on the actual distribution of irradiation on the surface of the hole. The hole surface is taken to be Gaussian and the depths are 5 and 10 mm, respectively. The lower part of both figures shows the geometry, the upper part shows the distributions of irradiation. The distribution supplied by the laser is indicated by the solid line and the actual distribution at the surface of the hole by the dashed line. At the initial situation, that is no hole has formed yet, the actual irradiation is just the non-reflected part (42%) of the input. Figs. 4.6(a) and 4.6(b) clearly show that the energy the laser supplies is focussed to

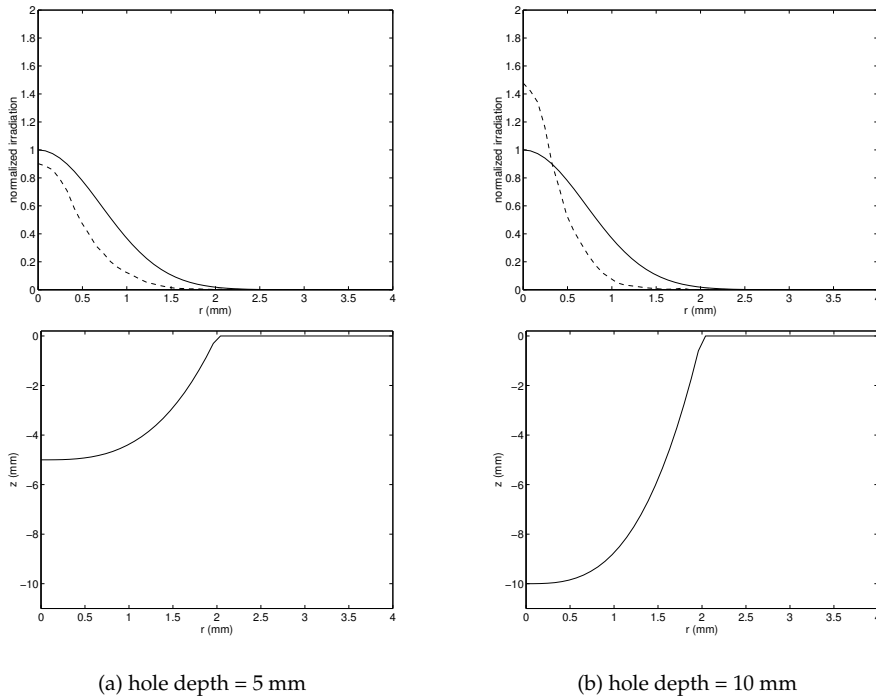


Figure 4.7: Multiple reflection simulation on a cubic drill hole surface. The surface is shown in the lower figures. The upper figures denote the irradiation. The input irradiation distribution is Gaussian and is denoted by the solid line, the actual distribution of irradiation is depicted by the dashed line.

the middle and at this center a very high energy concentration is found. Because the irradiation is directly related to the amount of material that can be liquefied and thereafter removed, tapering can easily be explained by this mechanism.

The influence multiple reflections have on the actual irradiation distribution strongly depends on the shape of the hole surface. In Fig. 4.7 the hole surface is taken to be a cubic polynomial. As can be seen by comparing Fig. 4.7 with Fig. 4.6, the incoupling of energy is far less efficient than with the Gaussian surface. Furthermore, the energy is focussed to the center of the hole, but not as strongly as for the Gaussian surface. These two examples show that multiple reflection phenomena are highly geometrically dependent and a preassumed hole shape is therefore inappropriate for simulation. Overall we see that in deeper holes multiple reflections occur and therefore a significantly bigger part of the energy supplied by the laser is coupled into the material. This enhanced incoupling of the laser beam for deeper holes is well known in industry, see e.g. [22]. In laser welding this phenomenon is referred to as *keyhole* formation in which the hole acts as a sort of blackbody, fully absorbing the incident radiation.

In order to stress the importance of multiple reflections in laser drilling, we also study multiple reflections during laser drilling on a different material (diamond / graphite) and with a different laser (excimer). During laser drilling in diamond the incoming energy causes the diamond to graphitise, and this graphite layer is heated up to its sublimation point: the actual material removal mechanism. Multiple reflections play an important role in this process. The reflectance of incoming laser light is most influential near the steep sides of the hole and it causes a typical absorbed intensity distribution at the surface. The laser used for drilling diamond is an excimer (KrF) laser which emits light at a wavelength of 248 nm (ultra violet UV-C). For this wavelength graphite has an index of refraction $n = 2.15$ and an extinction coefficient $k = 1.15$, see [9, 16]. For normal incidence this means a reflectivity of 24%. The irradiation distribution the excimer laser supplies is a top-hat distribution, and neglecting multiple reflections would imply that each pulse would remove a rectangular part. This would be the desired progress of the drilling process. However, multiple reflections cause the actual irradiation distribution to be quite different, as can be seen from Fig. 4.8. The actual irradiation distributions show a peak near the

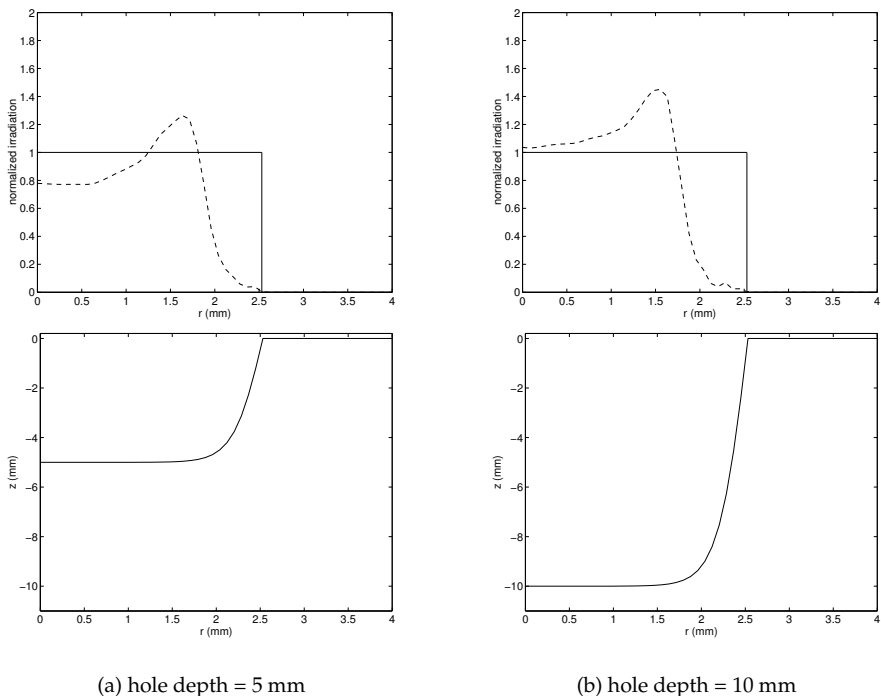


Figure 4.8: Multiple reflection simulation on a graphite surface. This surface is shown in the lower figures. The upper figures denote the irradiation. The input irradiation distribution is a top hat distribution and is denoted by the solid line, the actual distribution of irradiation is depicted by the dashed line.

sides. This is because the incoming light is for an important part reflected of the

steep sides. As the hole gets deeper, these peaks logically move towards the middle. As was the case for tungsten, the incoming radiation is coupled into the graphite more efficiently for deeper holes.

The results for both tungsten and graphite clearly show the importance of reflectivity on the irradiation distribution on the surface. In turn, it is this irradiation distribution that is directly related to the amount of material removed and therefore it dramatically influences the geometry of the hole drilled. Incorporating a model for the reflections is therefore essential in a thorough laser percussion drilling model. Not only does this reflection model properly predict the reflections but also the incoupling of energy is modelled. It is through this incoupling that the wavelength of the incoming beam comes into play. The index of refraction determines the amount of energy being coupled into the material and this index of refraction depends on the wavelength of the incoming wave, see Eq. (4.4). The influence of this dependence will be studied more thoroughly in Section 4.2.

Note that the index of refraction is highly material dependent and changes with temperature. Reliable experimental data on the reflectivity behaviour of hot metals are scarce. This has to be studied to get a more realistic model. The benefit for ARTM is that eventual absorption or scattering of radiation within a vapour cloud can be included.

4.2 Wavelength and peak intensity

Two laser related aspects that influence the outcome of a laser percussion drilling process are the wavelength of the incoming beam and its peak intensity. The wavelength mainly plays a role in the incoupling of the energy into the material. It does so through complex index of refraction which depends on wavelength, see Eq. (4.4). For aluminium and tungsten, this dependency is depicted in Fig. 4.9, data from [32]. The dotted lines are added to pinpoint the values for three typical laser wavelengths: a KrF excimer laser ($\lambda=248$ nm), a Nd:YAG-laser ($\lambda=1.064\mu\text{m}$) commonly used for laser drilling processes, and a CO₂ laser ($\lambda=10.6$ μm). It can be roughly stated that for metals the optical constants n and k increase with wavelength.

The effect the wavelength has on a laser drilling process is best illustrated through the reflectivity for perpendicular incidence onto a material. This reflectivity $\rho(\lambda)$ depends on wavelength through the optical constants $n(\lambda)$ and $k(\lambda)$ through Eq. (4.13). Its variation with wavelength for again aluminium and tungsten is shown in Fig. 4.10. In this figure, the importance of the wavelength on the reflectivity is clearly visible. Aluminium is not very suitable for laser drilling. Its reflectivity is very high from the near ultraviolet throughout the infrared, the domain in which industrial lasers are available. For tungsten the reflectivity for excimer lasers and the Nd:YAG laser is dramatically less than for the CO₂ laser, that is, the incoupling is much better; this makes the laser drilling process far more efficient. As for these two materials, the reflectivity is very high in the infrared region for most metals and therefore a CO₂ laser is not really suitable for laser drilling. Note furthermore that for the CO₂-laser

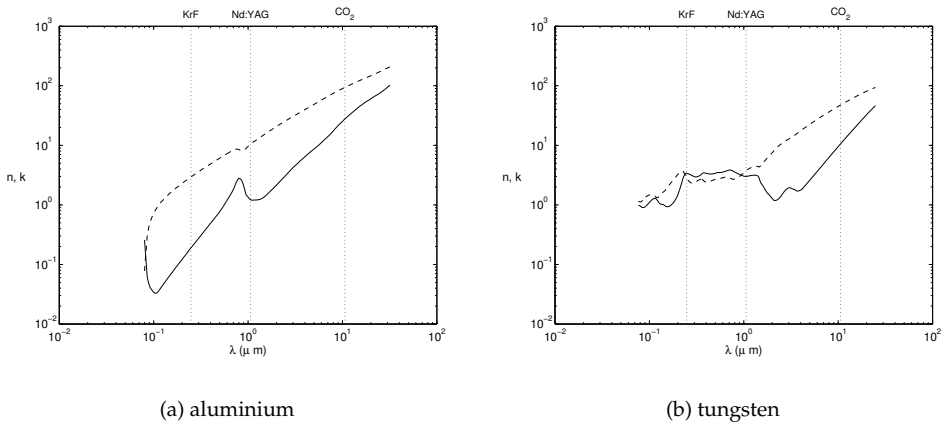


Figure 4.9: The index of refraction n (solid line) and the extinction coefficient k (dashed line) for aluminium and tungsten. The dotted lines denote the wavelengths of an excimer laser (KrF, $0.248 \mu\text{m}$), a Nd:YAG laser ($1.064 \mu\text{m}$) and a CO_2 laser ($10.6 \mu\text{m}$), respectively. (Data from [32])

as a result of the high values of $n(\lambda)$ and $k(\lambda)$ in the infrared for most materials, even a possible large variation of these optical constants with temperature produces only a small change in the reflectivity ρ , which is close to unity for these values. Summarizing, it can be stated that the optical behaviour of the metal under irradiation is of key importance to the outcome of the process. Moreover, the actual reflectivity behaviour of a material, as shown in Fig. 4.10 for aluminium and tungsten, should play an important role in the choice for a specific laser: the wavelength with the best incoupling behaviour, that is the lowest reflectivity, is favoured.

The peak intensity of the laser beam more or less determines what kind of material removal mechanism is dominant. That is, a high peak intensity will lead to more vaporisation, a lower peak intensity leads to more molten material. Furthermore, the assumption that the vapour is essentially transparent with respect to the irradiation, as we do in this thesis, holds for the irradiance régimes currently used at Eldim B.V. However, a vapour cloud does influence the process by scattering the laser beam as it travels through it, thereby distorting the wavefront. As stated previously, this scattering can be included in the ARTM context, but then more data are needed. At higher irradiances the vapour becomes partially ionized and absorbs a substantial fraction of the incoming laser energy. At a first glance one would think that this absorption would mean that the material is shielded. However, this absorption of laser energy leads to a vapour plasma which emits energy as blackbody radiation. This blackbody radiation tends to be absorbed more efficiently by the underlying metal substrate [1]. So if this plasma stays close to the surface, it may actually enhance the incoupling of energy into the material. At even higher irradiances than those leading to ionization of the hot vapour, a plasma may even occur in the cold ambient gas.

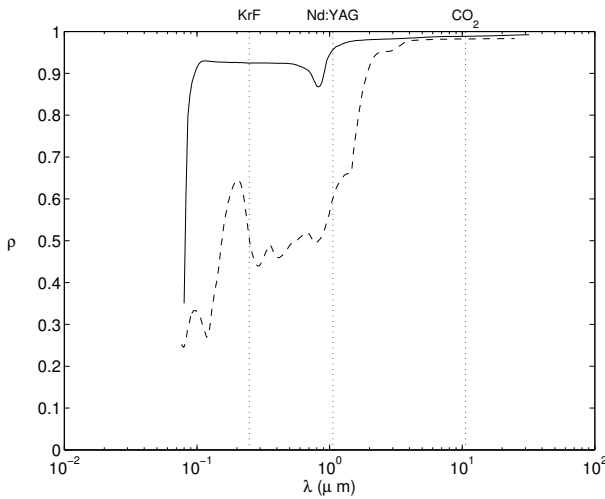


Figure 4.10: The reflectivity ρ for normal incidence of both an aluminium surface (solid line) and a tungsten surface (dashed line) in vacuum. The dotted lines denote the wavelengths of an excimer laser (KrF, $0.248 \mu\text{m}$), a Nd:YAG laser ($1.064 \mu\text{m}$) and a CO_2 laser ($10.6 \mu\text{m}$), respectively.

This plasma does not stay close to the surface, but propagates against the incident beam and shields the material completely, see [1, pp. 137–139].

Because of the fact that the interactions between laser light and the vapour only become apparent at higher irradiances than those used commonly in laser percussion drilling, this phenomenon falls outside the scope of this thesis. Yet, further research into this subject is needed if one wants to model laser percussion drilling for these higher irradiances correctly.

4.3 Spatial pulse shape

This section focusses on the importance of the spatial intensity distribution of the laser beam. For most industrial lasers this is either a Gaussian distribution or a top hat profile, see Fig. 4.11, and these two distributions will be used in the numerical simulations shown below. However, with the aid of numerical simulation we could also predict the results for different distributions. The basic laser settings used in this and subsequent sections are given in Table 4.1. Furthermore, in this Section as well as in the following, the material data of tungsten (see Table 2.1 and Section 4.1.3 for data on reflectivity) are used in the computations.

Symbol	Definition	Value
E_p	total energy per pulse	40 J
P_{av}	average power	50–100 W
t_p	pulse length	1×10^{-3} s
t_r	relaxation time	1×10^{-2} s
w	waist	1×10^{-3} m
λ	wavelength	1.064×10^{-6} m

Table 4.1: The data concerning the laser used in the simulation.

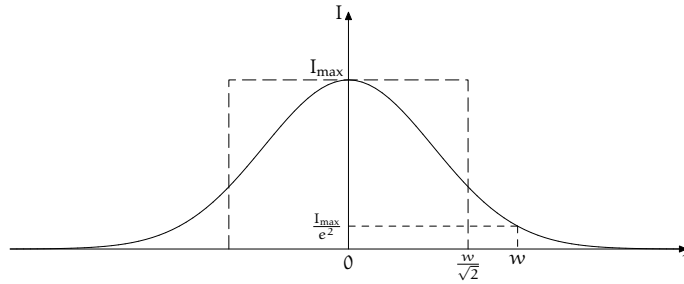


Figure 4.11: The two spatial irradiation distributions used in this section. The Gaussian distribution is denoted by the solid line and the top hat by the dashed pattern.

The intensity distributions the laser supplies are given by

$$I^G(r, t) = \begin{cases} I_{\max} e^{-\frac{2r^2}{w^2}}, & t \in [kt_r, kt_r + t_p], \quad k \in \mathbb{N}, \\ 0, & \text{elsewhere} \end{cases} \quad (4.30a)$$

and

$$I^T(r, t) = \begin{cases} I_{\max}, & r < w/\sqrt{2}, \quad t \in [kt_r, kt_r + t_p], \quad k \in \mathbb{N}, \\ 0, & \text{elsewhere,} \end{cases} \quad (4.30b)$$

for the Gaussian and the top hat profile, respectively. Here, w denotes the *waist*, that is a typical width of a Gaussian laser beam, see Section 2.2. The width of the top hat beam is adjusted so that the maximum intensity as well as the total energy per pulse is the same as for the Gaussian beam. The time distributions, also referred to as *time envelopes*, are taken to be top hat for both. The effect this time envelope has on the drilling process will be studied in the next section. Here a top hat distribution was used in order to compare results with analytical solutions for the one-dimensional model. The maximum intensity can be calculated from the total amount of energy per pulse E_p and the pulse length t_p , as done in Section 2.2. This yields

$$I_{\max} = \frac{2E_p}{\pi t_p w^2}, \quad (4.31)$$

for both the Gaussian and the top hat profile. The values of three parameters at the righthandside are equal for both set-ups and given in Table 4.1. One should bear in mind that a significant part (for tungsten: 58% for normal incidence) of the intensity the laser supplies is reflected. This leads to dimensionless scales as in Table 4.2.

Symbol	Definition	Value
I_{\max}	maximum intensity	$2.5 \times 10^{10} \text{ W m}^{-2}$
I_{ref}	maximum absorbed at surface	$1 \times 10^{10} \text{ W m}^{-2}$
t^*	equivalent of dimensionless unit	$1.0 \times 10^{-5} \text{ s}$
z^*	equivalent of dimensionless unit	$2.4 \times 10^{-5} \text{ m}$

Table 4.2: The dimensionless scales for experiments on spatial irradiation distributions.

To begin with, let us look at the first part of the initial pulse. The laser beam impinges on a flat surface and energy is converted into heat within the metal. Figure 4.12 shows the temperature distributions, together with the melting isotherm, in the metal for both settings at the time at which the surface reaches vaporization temperature. The coordinates in this figure are in dimensionless units. The melt

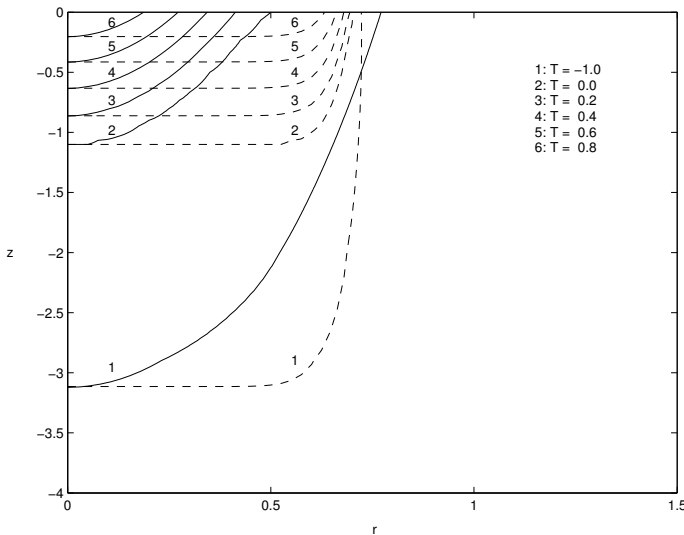


Figure 4.12: The temperature distributions within the irradiated material at the time at which the surface starts to evaporate. The dashed lines denote the contour lines caused by the top hat distribution, the solid lines denote the contour lines caused by the Gaussian distribution.

pool depth is 1.17 in dimensionless units. For tungsten this corresponds to approximately $2.84 \cdot 10^{-5} \text{ m}$. As can be seen, the contour lines follow the spatial irradiation distribution. This is in agreement with the analysis in Chapter 2, which ruled out the importance of radial diffusion. Furthermore, Fig. 4.12 shows that the energy provided in the top hat distribution is used far more efficiently. The dimensions of the

melt pool are considerably larger, allowing for more material to be removed. Note that the time at which the surface started to melt for both settings was $t = 3.35$ in dimensionless units, which is in agreement with the one-dimensional analytical model that led to (3.36), yielding $t_m = 3.34$ for tungsten. The time at which the surface starts to evaporate is $t_v = 7.6$. In dimensionless units the pulse length is $t_p = 98.2$, so if we assume the melt pool to splash out completely and instantaneously, we can expect up to 30 cycles of heating up and splashing per one millisecond pulse.

If we assume the melt pool to splash out completely and instantaneously, the melt model gives us the results for one pulse as in Figure 4.13. Note that the resulting

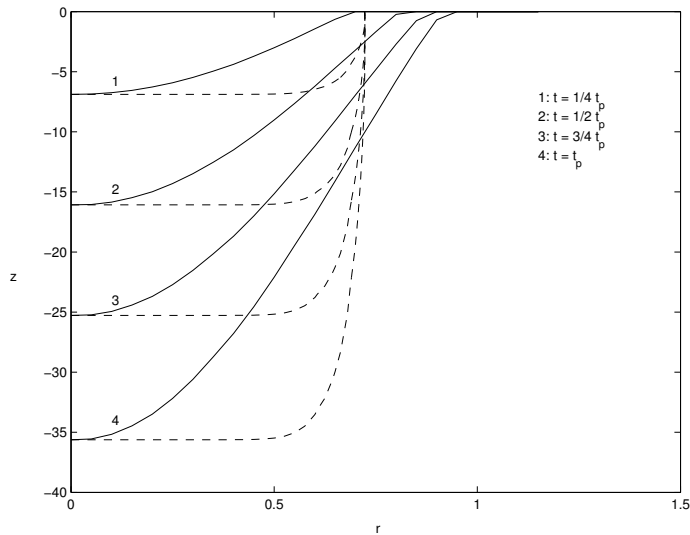


Figure 4.13: The evolution of the hole that has formed after one complete pulse. The different stages illustrate the hole geometry after a quarter, a half, three quarters of the pulse and after one complete pulse. The dashed lines show this for the top hat spatial distribution, the solid lines for the Gaussian distribution.

hole geometries for the two spatial distributions differ. As was already evident from Figure 4.12, the top hat distribution is a far more efficient distribution. The resulting hole depth is 36 in dimensionless units. For tungsten this corresponds to approximately 0.9 mm.

We conclude this section with some remarks concerning the actual spatial irradiation distribution of state-of-the-art lasers. The Gaussian beam as well as the top hat one are idealizations of the real beam. Normally, a laser beam that is said to be a Gaussian beam is far from truly Gaussian (only the TEM_{00} mode, cf. Section 2.2), but closer to the superposition of multiple TEM_{nm} modes. A method to extract these higher order contributions is presented in [47]. Furthermore, the pumping for a Nd:YAG laser is done by flash lamps. In this process the medium is heated up considerably and because of thermal effects beam distortions become noticeable. Because of a

non-axisymmetric lay-out of the laser regarding the pumping devices the thermal effects lead to a non Gaussian, more elliptically shaped laser beam. Obviously, in this case the computations should be performed on a three-dimensional grid.

4.4 Temporal pulse shape

In this section we study the importance of the time envelope of the laser pulse. The output of the laser pulse in time can be adjusted to some extent and this therefore gives us a manner to control the outcome of the process. We assume the spatial distribution to be Gaussian, as this distribution is provided by most industrial lasers. With state-of-the-art lasers, several different set-ups are possible: a top hat distribution, a sinusoidal time profile, a leading peak, a trailing peak and a pulse subdivided in several shorter pulses. In this section we look at the two most common time envelopes, namely the sinusoidal one and the top hat, see Fig. 4.14. The sinusoidal

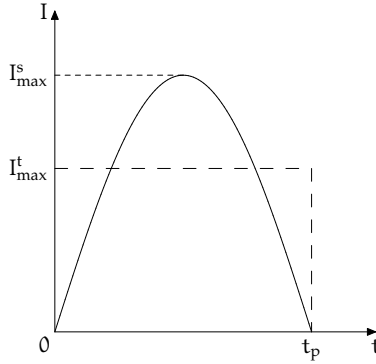


Figure 4.14: The two temporal irradiation distributions used in this section. The sinusoidal distribution is denoted by the solid line and the top hat by the dashed pattern.

distribution is denoted by the solid line and the top hat by the dashed pattern. The intensity distributions the laser supplies are given by

$$I^S(r, t) = \begin{cases} I_{\max}^s \sin\left(\frac{\pi(t-kt_r)}{t_p}\right) e^{-\frac{2r^2}{w^2}}, & t \in [kt_r, kt_r + t_p], \quad k \in \mathbb{N}, \\ 0, & \text{elsewhere} \end{cases} \quad (4.32a)$$

and

$$I^T(r, t) = \begin{cases} I_{\max}^t e^{-\frac{2r^2}{w^2}}, & t \in [kt_r, kt_r + t_p], \quad k \in \mathbb{N}, \\ 0, & \text{elsewhere,} \end{cases} \quad (4.32b)$$

for the sinusoidal and the top hat profile, respectively. The maximum intensity of the top hat distribution is chosen such that the total amount of energy per pulse is

the same as for the sinusoidal distribution, yielding

$$I_{\max}^T = \frac{2}{\pi} I_{\max}^S, \quad (4.33)$$

with I_{\max}^S as in (2.4). This leads to the dimensionless scales as in Table 4.3.

Symbol	Definition	Value
I_{\max}^S	maximum intensity	$4.0 \times 10^{10} \text{ W m}^{-2}$
I_{ref}	maximum absorbed at surface	$1.68 \times 10^{10} \text{ W m}^{-2}$
t^*	equivalent of dimensionless unit	$3.6 \times 10^{-6} \text{ s}$
z^*	equivalent of dimensionless unit	$1.4 \times 10^{-5} \text{ m}$

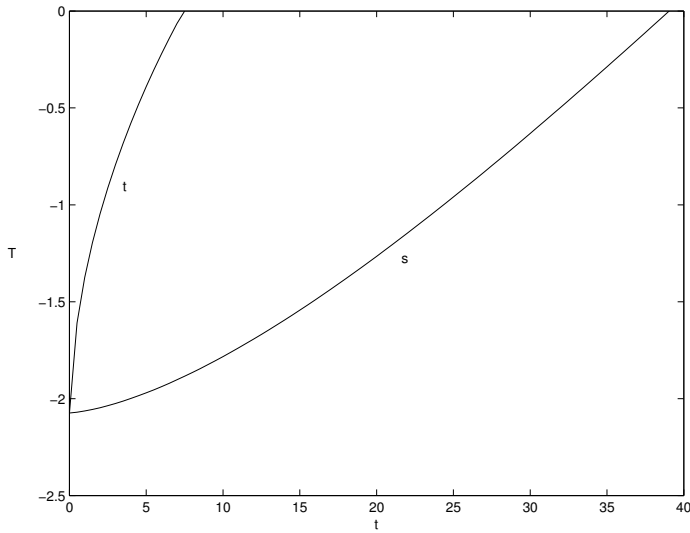
Table 4.3: *The dimensionless scales for experiments on temporal irradiation distributions.*

Some effects the different time envelope has on the melting process are illustrated in Fig. 4.15. Obviously, the heating up of the material is faster for the top hat distribution, as illustrated in Fig. 4.15(a). But, more interestingly, the subcyclic behaviour within a pulse is completely different (Fig. 4.15) for the two time envelopes, as can be expected. This figure shows the moments in time at which the central point reaches vaporization temperature (sinusoidal in the upper half, top hat in the lower half). For the top hat time envelope the intervals are more or less equidistant, for the sinusoidal time envelope, the intervals are smaller in the center.

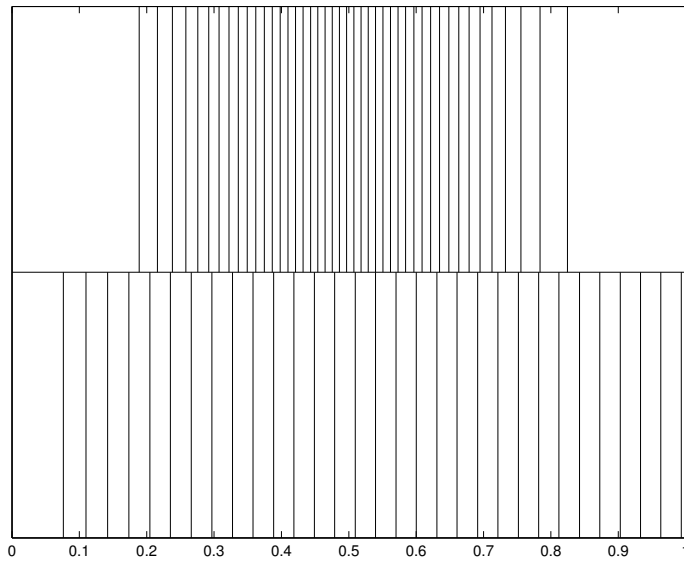
If we assume the melt pool to splash out completely and instantaneously as we did in the previous section, the melt model gives us the results for one pulse as in Figure 4.16. Note that the resulting hole geometries for the two temporal distributions do not differ that much. The subcyclic behaviour, however, is completely different and gives us much more insight in the effect the time envelope has on the process.

4.5 Simulation

In this section we perform a complete numerical simulation of a laser percussion drilling process. The material we take is tungsten and for the laser we take the settings of a Nd:YAG laser as used frequently. That is, we take the temporal pulse shape to be sinusoidal and the spatial pulse shape to be Gaussian (TEM_{00}). The simulation model uses the melting model with the results of the reflection model as input. The molten material present at the time at which the surface reaches vaporization temperature is assumed to splash out completely and instantaneously. This means that we assume that several subcycles of heating/splashing occur during one pulse. The experimentally observed reflectivity behaviour supports this subcycle theory. Furthermore, we assume that the remaining material has cooled down completely in between two subsequent pulses. This assumption is supported by the tests carried out in the previous section. Fig. 4.17 shows the results of a simulation over ten subsequent laser pulses on a tungsten sample. For clarity, the r and z values in this figure are in millimeters. The strong effect of reflectivity on the hole geometry is clear to



(a) Temperature



(b) Subcyclic behaviour

Figure 4.15: Some effects of the time envelope on the melting process. Figure (a) shows the time history plot of the temperature of the origin at the start of the pulse. Temperature and time are in dimensionless units. The lines are marked to discern the sinusoidal and the top hat irradiation distribution. Figure (b) shows the distinct subcyclic behaviour following from the different time envelopes (sinusoidal one in the upper half, top hat in the lower half).

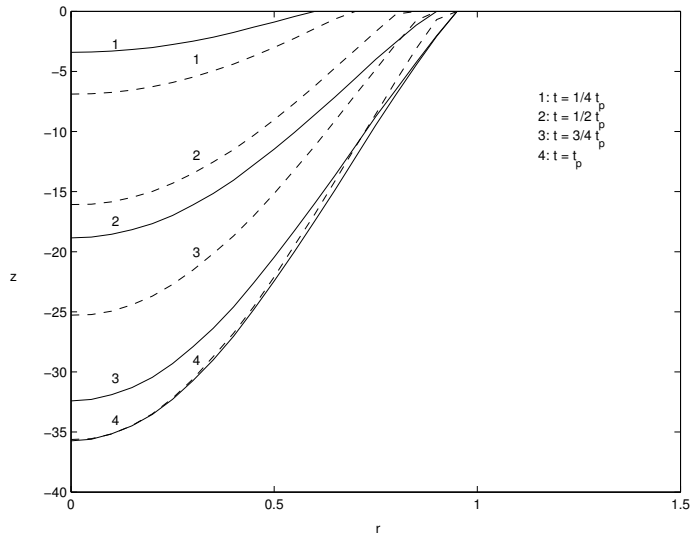


Figure 4.16: The evolution of the hole that has formed after one complete pulse. The different stages illustrate the hole geometry after a quarter, a half, three quarters of the pulse and after one complete pulse. The dashed lines show this for the top hat distribution in time, the solid lines for the sinusoidal time envelope.

see in this simulation. The tapering is enforced by the effect of reflectivity as already stated in Section 4.1.3. However, note that these results have been produced by using a parallel beam, which is not the case in practice. In practice the beam diverges while the hole grows deeper, and hereby, the reflectivity effect is reduced to some extent. With accurate data on the laser settings more accurate results can be calculated.

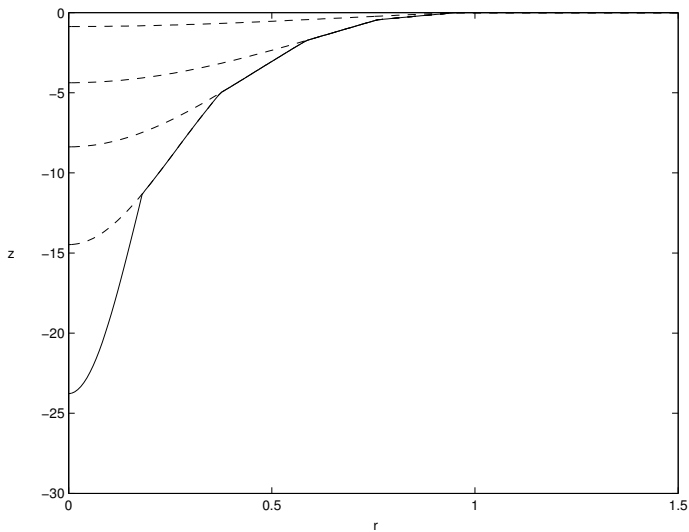


Figure 4.17: The results of a simulation consisting of ten subsequent laser pulses. The dashed lines denote the hole geometries after two, four, six and eight pulses respectively. The solid line is the final hole geometry after ten pulses.

Splashing and solidification

In this chapter we focus on the splashing and solidification models, briefly described in Chapter 2. We will derive the leading-orders for these two models in Sections 5.1 and 5.2. The splashing model contains a link to the model for the gas dynamics and this model needs to be investigated further experimentally. Therefore, we will explain a method to solve the leading-order model for solidification in Section 5.3.

5.1 Axisymmetric splashing model

In this section we derive the leading-order equations for the splashing model. For this we start of from the non-dimensional form of the equations describing the splashing mechanism as already derived in Chapter 2. These represent conservation of mass

$$\frac{\partial^2 \phi}{\partial r^2} + \frac{1}{r} \frac{\partial \phi}{\partial r} + \frac{1}{\delta^2} \frac{\partial^2 \phi}{\partial z^2} = 0 \quad (5.1a)$$

and conservation of energy

$$\frac{\partial \theta}{\partial t} + \frac{\partial \phi}{\partial r} \frac{\partial \theta}{\partial r} + \frac{1}{\delta^2} \frac{\partial \phi}{\partial z} \frac{\partial \theta}{\partial z} = D \left\{ \delta^2 \left(\frac{\partial^2 \theta}{\partial r^2} + \frac{1}{r} \frac{\partial \theta}{\partial r} \right) + \frac{\partial^2 \theta}{\partial z^2} \right\}, \quad \text{in } \Omega_l \quad (5.1b)$$

in the liquid. Conservation of energy in the solid led to

$$\frac{\partial \theta}{\partial t} = D \left\{ \delta^2 \left(\frac{\partial^2 \theta}{\partial r^2} + \frac{1}{r} \frac{\partial \theta}{\partial r} \right) + \frac{\partial^2 \theta}{\partial z^2} \right\}, \quad \text{in } \Omega_s. \quad (5.2)$$

The vaporizing isotherm is expressed by

$$\theta = \theta_v(\bar{p}). \quad (5.3a)$$

Furthermore, we have conservation of momentum

$$\frac{\partial \phi}{\partial t} + \frac{1}{2} \left(\left(\frac{\partial \phi}{\partial r} \right)^2 + \frac{1}{\delta^2} \left(\frac{\partial \phi}{\partial z} \right)^2 \right) + \bar{p} = 0, \quad (5.3b)$$

and conservation of energy

$$\frac{1}{\delta^2} \frac{\partial \phi}{\partial z} - \frac{\partial \phi}{\partial r} \frac{\partial h}{\partial r} - \frac{\partial h}{\partial t} = \bar{I} - \frac{D}{\lambda_v \bar{L}_v} \left(\frac{\partial \theta}{\partial z} - \delta^2 \frac{\partial h}{\partial r} \frac{\partial \theta}{\partial r} \right) \quad \text{on } z = h(r, t), \quad (5.3c)$$

on the vaporizing surface. The solid-liquid interface is at melting temperature

$$\theta = 0. \quad (5.4a)$$

Conservation of mass yielded

$$\frac{1}{\delta^2} \frac{\partial \phi}{\partial z} = \frac{\partial \phi}{\partial r} \frac{\partial s}{\partial r}, \quad (5.4b)$$

and the Stefan condition told us

$$\lambda_f \frac{\partial s}{\partial t} + D \left[\frac{\partial \theta}{\partial z} - \delta^2 \frac{\partial s}{\partial r} \frac{\partial \theta}{\partial r} \right]_{s^-}^{s^+} = 0 \quad \text{on } z = s(r, t). \quad (5.4c)$$

Finally, at infinity we have ambient conditions

$$\theta \rightarrow \theta_a \quad \text{as } z \rightarrow -\infty. \quad (5.5)$$

We introduce expansions of the form

$$\phi \sim \phi_0 + \delta^2 \phi_1, \quad \theta \sim \theta_0 + \delta^2 \theta_1, \quad h \sim h_0 + \delta^2 h_1, \quad s \sim s_0 + \delta^2 s_1, \quad (5.6)$$

where ϕ_* , θ_* , h_* and s_* are independent of δ . We transfer the condition from the correct boundary $z = s$ to a convenient boundary $z = s_0$ by using a Taylor series expansion, that is

$$\frac{\partial \phi}{\partial z} \Big|_{z=s} = \frac{\partial \phi_0}{\partial z} \Big|_{z=s_0} + \delta^2 \left(\frac{\partial \phi_1}{\partial z} \Big|_{z=s_0} + s_1 \frac{\partial^2 \phi_0}{\partial z^2} \Big|_{z=s_0} \right) + O(\delta^4). \quad (5.7)$$

A similar transfer takes place between $z = h$ and $z = h_0$.

Equation (5.1a) gives us

$$\frac{\partial^2 \phi_0}{\partial z^2} = 0.$$

Together with (5.4b), which tells us

$$\frac{\partial \phi_0}{\partial z} = 0, \quad \text{at } z = s_0,$$

this leads to

$$\frac{\partial \phi_0}{\partial z} = 0.$$

Thus,

$$\phi_0 = \alpha(r, t).$$

Substituting this into (5.1a) again, yields

$$\frac{\partial^2 \phi_1}{\partial z^2} = -\frac{\partial^2 \alpha}{\partial r^2} - \frac{1}{r} \frac{\partial \alpha}{\partial r} = -\frac{1}{r} \frac{\partial}{\partial r} \left(r \frac{\partial \alpha}{\partial r} \right),$$

and therefore

$$\frac{\partial \phi_1}{\partial z} = -\frac{z}{r} \frac{\partial}{\partial r} \left(r \frac{\partial \alpha}{\partial r} \right) + c(r, t).$$

Then (5.4b) gives us

$$\frac{\partial \phi_1}{\partial z} = \frac{\partial \alpha}{\partial r} \frac{\partial s_0}{\partial r}, \quad \text{on } z = s_0.$$

Thus

$$c(r, t) = \frac{\partial \alpha}{\partial r} \frac{\partial s_0}{\partial r} + \frac{s_0}{r} \frac{\partial}{\partial r} \left(r \frac{\partial \alpha}{\partial r} \right) = \frac{1}{r} \frac{\partial}{\partial r} \left(s_0 r \frac{\partial \alpha}{\partial r} \right).$$

So

$$\phi_1 = -\frac{z^2}{2r} \frac{\partial}{\partial r} \left(r \frac{\partial \alpha}{\partial r} \right) + \frac{z}{r} \frac{\partial}{\partial r} \left(s_0 r \frac{\partial \alpha}{\partial r} \right) + b(r, t).$$

Through this derivation, we obtain

$$\phi \sim \alpha + \delta^2 \left\{ b - \frac{z^2}{2r} \frac{\partial}{\partial r} \left(r \frac{\partial \alpha}{\partial r} \right) + \frac{z}{r} \frac{\partial}{\partial r} \left(s_0 r \frac{\partial \alpha}{\partial r} \right) \right\} \quad (5.8)$$

where $\alpha = \alpha(r, t)$ and $b = b(r, t)$ are unknown functions. Substituting (5.8) into (5.1b), (5.3b) and (5.3c), we find

$$\frac{\partial \theta_0}{\partial t} + \frac{\partial \alpha}{\partial r} \frac{\partial \theta_0}{\partial r} + \left\{ \frac{1}{r} \frac{\partial}{\partial r} \left(r \frac{\partial \alpha}{\partial r} s_0 \right) - \frac{z}{r} \frac{\partial}{\partial r} \left(r \frac{\partial \alpha}{\partial r} \right) \right\} \frac{\partial \theta_0}{\partial z} = D \frac{\partial^2 \theta_0}{\partial z^2},$$

$$\frac{\partial \alpha}{\partial t} + \frac{1}{2} \left(\frac{\partial \alpha}{\partial r} \right)^2 + \bar{p} = 0,$$

and

$$\frac{\partial h_0}{\partial t} + \frac{1}{r} \frac{\partial}{\partial r} \left(r \frac{\partial \alpha}{\partial r} (h_0 - s_0) \right) + \bar{I} = 0,$$

respectively. Finally, we make the substitution $u = \frac{\partial a}{\partial r}$, to give a differential equation for the temperature

$$\begin{aligned} \frac{\partial \theta_0}{\partial t} + u \frac{\partial \theta_0}{\partial r} + \left\{ \frac{1}{r} \frac{\partial}{\partial r} (ru s_0) - \frac{z}{r} \frac{\partial}{\partial r} (ru) \right\} \frac{\partial \theta_0}{\partial z} \\ = D \frac{\partial^2 \theta_0}{\partial z^2} \quad \text{for } s_0 < z < h_0, \end{aligned} \quad (5.9)$$

with two boundary conditions

$$\theta_0 = 0, \quad \text{on } z = s_0 \quad \theta_0 = \theta_v(\bar{p}) \quad \text{on } z = h_0, \quad (5.10)$$

the equation for the evolution of the velocity

$$\frac{\partial u}{\partial t} + u \frac{\partial u}{\partial r} + \frac{\partial \bar{p}}{\partial r} = 0, \quad (5.11)$$

the equations for the evolution of the free boundaries

$$\frac{\partial h_0}{\partial t} + \frac{1}{r} \frac{\partial}{\partial r} \{ru(h_0 - s_0)\} + \bar{I} = 0, \quad \lambda_f \frac{\partial s_0}{\partial t} + D \left[\frac{\partial \theta_0}{\partial z} \right]_{s_0^-}^{s_0^+} = 0, \quad (5.12)$$

the equation and the boundary condition for conduction in the solid

$$\frac{\partial \theta_0}{\partial t} = D \frac{\partial^2 \theta_0}{\partial z^2} \quad \text{for } z < s_0 \quad \text{and} \quad \theta_0 \rightarrow \theta_a \quad \text{as } z \rightarrow -\infty. \quad (5.13)$$

The leading-order equations to describe axisymmetric splashing are (5.9)-(5.13).

We rewrite this set of equations to avoid complications with subscripts in subsequent sections. Furthermore, we chose to use the film thickness $\xi := h_0 - s_0$ as a variable rather than h_0 . We also replace s_0 by ψ and omit the subscript in θ_0 in the numerical model. This leaves us with the following system of equations

$$\frac{\partial \xi}{\partial t} + \frac{1}{r} \frac{\partial}{\partial r} (ru\xi) = -\bar{I} - \frac{\partial \psi}{\partial t}, \quad (5.14)$$

$$\frac{\partial u}{\partial t} + u \frac{\partial u}{\partial r} + \frac{\partial \bar{p}}{\partial r} = 0, \quad (5.15)$$

$$\frac{\partial \theta}{\partial t} + \frac{1}{r} \frac{\partial}{\partial r} (ru\theta) + \frac{\partial}{\partial z} \left(\left\{ \frac{1}{r} \frac{\partial}{\partial r} (ru\psi) - \frac{z}{r} \frac{\partial}{\partial r} (ru) \right\} \theta - D \frac{\partial \theta}{\partial z} \right) = 0, \quad (5.16)$$

and

$$\theta = \theta_v(\bar{p}) \quad \text{on } z = \psi + \xi, \quad (5.17)$$

in the fluid,

$$\theta = 0, \quad (5.18)$$

and

$$\lambda_f \frac{\partial \psi}{\partial t} + D \left[\frac{\partial \theta}{\partial z} \right]_{\psi^-}^{\psi^+} = 0, \quad \text{on } z = \psi, \quad (5.19)$$

at the interface and

$$\frac{\partial \theta}{\partial t} = D \frac{\partial^2 \theta}{\partial z^2}, \quad \text{for } z < \psi \quad (5.20)$$

and

$$\theta \rightarrow \theta_a \quad \text{as } z \rightarrow -\infty, \quad (5.21)$$

in the solid.

5.2 Planar solidification model

The derivation of the leading-order equations for the solidification model is similar to that of the splashing model. We use the same expansions, that is (5.6), and also transfer the boundary conditions using Taylor series expansions as in (5.7).

Similar to the derivation followed in the previous section, from Eqs. (2.44a) and (2.47b) we obtain

$$\phi \sim a + \delta^2 \left\{ b - \frac{1}{2} \frac{\partial^2 a}{\partial x^2} y^2 + \frac{\partial}{\partial x} \left(\frac{\partial a}{\partial x} s_0 \right) y \right\}, \quad (5.22)$$

where $a = a(x, t)$ and $b = b(x, t)$ are unknown functions. Substituting $u = \frac{\partial a}{\partial x}$, we find, similarly to the derivation in the previous section, the following system of equations:

$$\frac{\partial \xi}{\partial t} + \frac{\partial}{\partial x} (u\xi) = -\frac{\partial \psi}{\partial t}, \quad (5.23)$$

$$\frac{\partial u}{\partial t} + u \frac{\partial u}{\partial x} = 0, \quad (5.24)$$

$$\frac{\partial \theta}{\partial t} + \frac{\partial}{\partial x} (u\theta) + \frac{\partial}{\partial y} \left(\left\{ \frac{\partial}{\partial x} (u\psi) - \frac{\partial u}{\partial x} y \right\} \theta - D \frac{\partial \theta}{\partial y} \right) = 0, \quad (5.25)$$

and

$$\frac{\partial \theta}{\partial y} = 0 \quad \text{on } y = \psi + \xi, \quad (5.26)$$

in the fluid,

$$\theta = 0, \quad (5.27)$$

and

$$\lambda_f \frac{\partial \psi}{\partial t} + D \left[\frac{\partial \theta}{\partial y} \right]_{\psi^-}^{\psi^+} = 0, \quad \text{on } y = \psi, \quad (5.28)$$

at the interface and

$$\frac{\partial \theta}{\partial t} = D \frac{\partial^2 \theta}{\partial y^2}, \quad \text{for } y < \psi \quad (5.29)$$

and

$$\theta \rightarrow \theta_a \quad \text{as } y \rightarrow -\infty, \quad (5.30)$$

in the solid.

This system of equations together with suitable initial conditions will be treated numerically in Section 5.3.

5.3 Numerical methods for solidification

We consider the leading-order problem for the solidification of an amount of molten material flowing past a relative cold solid wall. For its derivation, see Section 5.2. Here $\xi = \xi(x, t)$ represents the thickness of melt film and $\psi = \psi(x, t)$ represents the height of the solid-liquid boundary. Furthermore $\theta = \theta(x, y, t)$ represents the temperature of the material, and $u = u(x, t)$ represents the horizontal velocity of the melt film. Note that all the variables are dimensionless. The problem consists of the following equations.

Conservation of mass

$$\frac{\partial \xi}{\partial t} + \frac{\partial}{\partial x}(u\xi) = -\frac{\partial \psi}{\partial t}; \quad (5.31)$$

Burgers equation

$$\frac{\partial u}{\partial t} + u \frac{\partial u}{\partial x} = 0. \quad (5.32)$$

The combination of these two equations also gives the conservation of momentum equation

$$\frac{\partial}{\partial t}(u\xi) + \frac{\partial}{\partial x}(u^2\xi) = -u \frac{\partial \psi}{\partial t}. \quad (5.33)$$

Furthermore, we have conservation of energy in the melt

$$\frac{\partial \theta}{\partial t} + \frac{\partial}{\partial x}(u\theta) + \frac{\partial}{\partial y} \left(\left\{ \frac{\partial}{\partial x}(u\psi) - \frac{\partial u}{\partial x} y \right\} \theta - D \frac{\partial \theta}{\partial y} \right) = 0 \quad \text{for } \psi < y < \psi + \xi, \quad (5.34)$$

which may also be written as

$$\frac{\partial \theta}{\partial t} + u \frac{\partial \theta}{\partial x} + \left\{ \frac{\partial}{\partial x}(u\psi) - \frac{\partial u}{\partial x} y \right\} \frac{\partial \theta}{\partial y} - D \frac{\partial^2 \theta}{\partial y^2} = 0 \quad \text{for } \psi < y < \psi + \xi. \quad (5.35)$$

Furthermore, there is no heat flux through the top surface:

$$\frac{\partial \theta}{\partial y} = 0 \quad \text{on } y = \psi + \xi. \quad (5.36)$$

We have the Stefan condition

$$\lambda_f \frac{\partial \psi}{\partial t} + D \left[\frac{\partial \theta}{\partial y} \right]_{\psi^-}^{\psi^+} = 0, \quad (5.37)$$

and the melting isotherm

$$\theta = 0 \quad \text{on } y = \psi, \quad (5.38)$$

at the solid-liquid interface. The well-known heat equation holds in the solid

$$\frac{\partial \theta}{\partial t} = D \frac{\partial^2 \theta}{\partial y^2} \quad \text{for } y < \psi, \quad (5.39)$$

with ambient conditions at infinity

$$\theta \rightarrow \theta_a \quad \text{as } y \rightarrow -\infty. \quad (5.40)$$

The initial conditions are prescribed velocity

$$u(x, 0) = u_0(x), \quad (5.41)$$

prescribed temperature

$$\theta(x, y, 0) = \theta_0(x, y), \quad (5.42)$$

and a prescribed geometry

$$\xi(x, 0) = \xi_0(x), \quad (5.43)$$

and

$$\psi(x, 0) = \psi_0(x). \quad (5.44)$$

Here we assume

$$\theta_0(x, y) = \theta_a \quad \text{for } y < \psi_0(x), \quad \theta_0(x, \psi_0(x)) = 0 \quad \text{and} \\ \frac{\partial \theta_0}{\partial y}(x, \psi_0(x) + \xi_0(x)) = 0 \quad \text{for } \xi_0(x) > 0.$$

5.3.1 Shocks

We note that (5.32) uncouples from the system of equations. As known, this equation can exhibit shocks, see e.g. [51]. Because the melt always has compact support, shocks will occur. Let $u(x, 0) = u_0(x)$ be the initial velocity profile. Then the time of first 'breaking' is

$$t_B = -\frac{1}{u'_0(X_s)},$$

where X_s is defined by:

$$u'_0(X_s) < 0, \quad |u'_0(X_s)| \text{ is a maximum.}$$

To study the shock in detail, we use that $u_0(x)$ vanishes outside the range $[X_L, X_R]$, and $u_0(x) > 0$ in the range. Then, one can show ([51, pp. 46–47]) that for $t > t_B$ the asymptotic formulas for the position of the shock $s(t)$ and the velocity just behind the shock u are

$$s \sim \sqrt{2At}, \tag{5.45}$$

$$u \sim \sqrt{\frac{2A}{t}}, \tag{5.46}$$

respectively. Here

$$A = \int_{X_L}^{X_R} u_0(x) dx \tag{5.47}$$

is the area of the hump. The asymptotic form of the velocity profile is

$$u \sim \frac{x - X_L}{t}, \quad X_L < x < X_L + \sqrt{2At}. \tag{5.48}$$

So, the details of the initial velocity distribution are lost; only the area A is preserved.

Because the shock in the velocity distribution travels at half the speed of the velocity just behind the shock and because of conservation of mass, melt will amass behind this leading edge shock.

5.3.2 Enthalpy Method

We define $X_L(t)$ and $X_U(t)$ to be the points $X_L(t) = \inf\{x | \xi(x, t) > 0\}$ and $X_U(t) = \sup\{x | \xi(x, t) > 0\}$, that is, $X_L(t)$ and $X_U(t)$ represent the 'beginning' and 'ending' of the liquid blob, respectively. We introduce the dimensionless enthalpy, η , by

$$\eta = \begin{cases} \theta & \theta < 0 \quad (\text{solid}), \\ \theta + \lambda_f & \theta > 0 \quad (\text{liquid}), \end{cases} \tag{5.49}$$

and therefore

$$\theta = \begin{cases} \eta & \eta < 0, \\ 0 & 0 < \eta < \lambda_f, \\ \eta - \lambda_f & \eta > \lambda_f, \end{cases} \quad (5.50)$$

The Eqs. (5.34)₁, (5.37), (5.38) and (5.39)₁ can then be rewritten as

$$\frac{\partial \eta}{\partial t} + \frac{\partial}{\partial x}(\chi u \theta) + \frac{\partial}{\partial y} \left(\chi \left\{ \frac{\partial}{\partial x}(u \psi) - \frac{\partial u}{\partial x} y \right\} \theta \right) - D \frac{\partial^2 \theta}{\partial y^2} = 0, \quad (5.51)$$

where χ is the characteristic function

$$\chi = \begin{cases} 0 & \theta < 0 \quad (\text{solid}), \\ 1 & \theta > 0 \quad (\text{liquid}). \end{cases} \quad (5.52)$$

Alternatively, (5.51) can be written as

$$\frac{\partial \eta}{\partial t} + \chi u \frac{\partial \theta}{\partial x} + \chi \left\{ \frac{\partial}{\partial x}(u \psi) - \frac{\partial u}{\partial x} y \right\} \frac{\partial \theta}{\partial y} - D \frac{\partial^2 \theta}{\partial y^2} = 0. \quad (5.53)$$

We will use this enthalpy method in our numerical method as will be explained in the next section.

5.3.3 Numerical Method

The geometry that will be used throughout this section is sketched in Figure 5.1. The

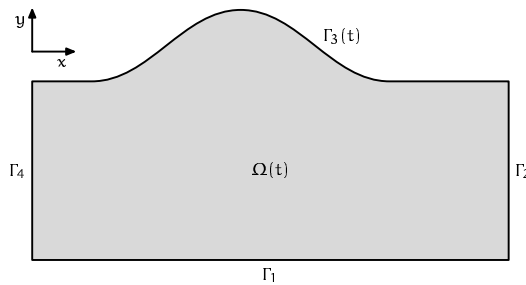


Figure 5.1: *The geometry used in the numerics for the solidification problem.*

problem to solve is comprised by (5.31), (5.33) or (5.32), and (5.51) together with the relationships between temperature and enthalpy (5.49) and (5.50) and the boundary and initial conditions (5.36) and (5.40)-(5.44).

One way of solving this system is the following. Suppose everything is known at time level t_n : E^n , θ^n , u^n , ξ^n , ψ^n , Ω^n . From the enthalpy equation (5.51) together with (5.49) and (5.50), we find E^{n+1} , θ^{n+1} and ψ^{n+1} . Now we've got a choice: we

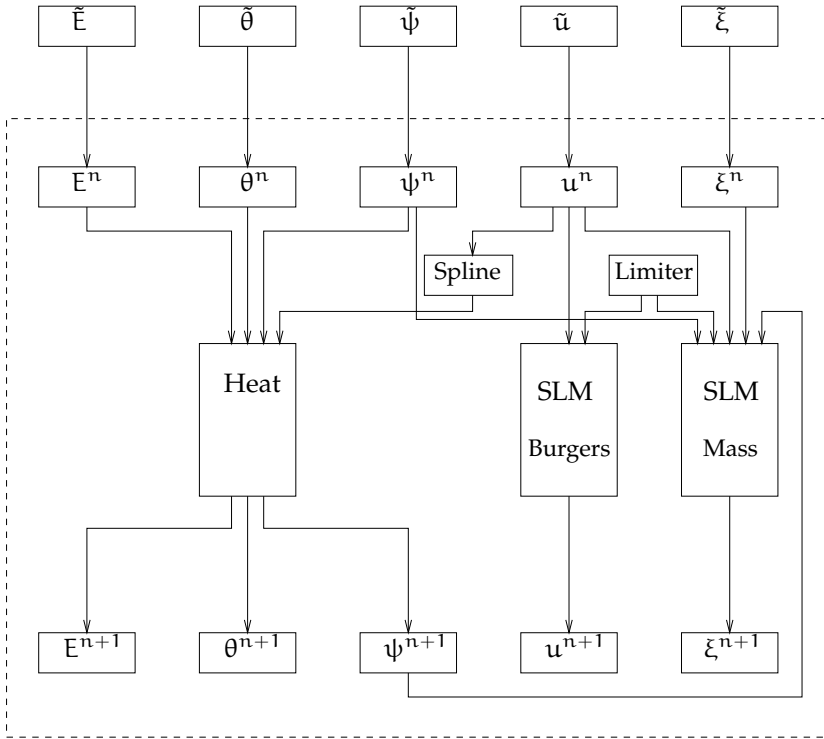


Figure 5.2: *The numerical scheme.*

could use the coupled system (5.31) and (5.33) to compute u^{n+1} and ξ^{n+1} or we could use (5.31) and (5.32) for this. The latter method has the benefit that this is a decoupled system, u^{n+1} follows from (5.32) and ξ^{n+1} then follows from (5.31). The final step is then to compute the new domain Ω^{n+1} from u^{n+1} , ξ^{n+1} and ψ^{n+1} . This numerical solving procedure is depicted in Figure 5.2. As u^n represents a vector of velocities on different coordinates, we cannot use this vector as such in the 2D enthalpy problem. Hence, the 'Spline'-block in this figure represents a possible way of dealing with this.

The slope limiter scheme

In order to solve Burgers' equation for the horizontal velocity we use a slope limiter method, see e.g. [26]. This slope limiter method is based on the Godunov scheme and is therefore a finite volume method. Consider the following initial value problem for $u(x, t)$

$$\frac{\partial u}{\partial t} + \frac{\partial f(u)}{\partial x} = 0, \quad x \in \mathbb{R}, t > 0, \quad (5.54a)$$

$$u(x, 0) = \tilde{u}(x), \quad x \in \mathbb{R}. \quad (5.54b)$$

We introduce control volumes V_j :

$$V_j := \left[x_{j-\frac{1}{2}}, x_{j+\frac{1}{2}} \right), \quad x_{j+\frac{1}{2}} = \frac{1}{2} (x_j + x_{j+1}), \quad j = 0, \pm 1, \pm 2, \dots \quad (5.55)$$

The numerical solution u_j^n has to be interpreted as an approximation of the average value of $u(x, t)$ over V_j at time level t_n . Associated with this u_j^n we define the function $U(x, t)$ by:

$$\frac{\partial U}{\partial t} + \frac{\partial f(U)}{\partial x} = 0, \quad x \in \mathbb{R}, t > t_n, \quad (5.56a)$$

$$U(x, t_n) = u_j^n + s_j^n (x - x_j), \quad x \in V_j, \quad j = 0, \pm 1, \pm 2, \dots, \quad n = 0, 1, 2, \dots \quad (5.56b)$$

Here, u_j^n and s_j^n are the average value and slope, respectively, of $U(x, t_n)$ in the control volume V_j . The 'initial' value $U(x, t_n)$ is thus piecewise linear in each V_j . The slope s_j^n is still unknown, and has to be determined such that the resulting scheme is Total Variation Diminishing (TVD), see e.g [20]. The slope limiter method is based on the integral formulation of the initial value problem (5.56).

After integration over the control volume V_j and over the time interval $[t_n, t_{n+1}]$, we obtain

$$\int_{V_j} U(x, t_{n+1}) dx - \int_{V_j} U(x, t_n) dx = -\Delta t (F(u_j^n, u_{j+1}^n) - F(u_{j-1}^n, u_j^n)), \quad (5.57)$$

where the numerical flux $F(u_j^n, u_{j+1}^n)$ is defined as

$$F(u_j^n, u_{j+1}^n) := \frac{1}{\Delta t} \int_{t_n}^{t_{n+1}} f(U(x_{j+\frac{1}{2}}, t)) dt. \quad (5.58)$$

To compute the numerical flux $F(u_j^n, u_{j+1}^n)$ we have to solve the generalized Riemann problem comprised by the conservation law (5.56a) and the piecewise linear initial condition. This is generally difficult and involving, and for that reason we replace the flux $f(u)$ by its linear interpolant $\tilde{f}(u)$, i.e.

$$\tilde{f}(u) := f(u_j^n) + \tilde{a}_{j+\frac{1}{2}}^n (u - u_j^n), \quad u \in \text{int}(u_j^n, u_{j+1}^n), \quad (5.59)$$

with $\tilde{a}_{j+\frac{1}{2}}^n$ the finite difference approximation of $f'(u(x_{j+\frac{1}{2}}, t_n))$ given by

$$\tilde{a}_{j+\frac{1}{2}}^n := \begin{cases} \frac{f(u_{j+1}^n) - f(u_j^n)}{u_{j+1}^n - u_j^n} & \text{if } u_j^n \neq u_{j+1}^n, \\ 0 & \text{if } u_j^n = u_{j+1}^n. \end{cases} \quad (5.60)$$

Replacing $f(u)$ by $\tilde{f}(u)$, the generalized Riemann problem reduces to the following initial value problem

$$\frac{\partial U}{\partial t} + \tilde{a}_{j+\frac{1}{2}}^n \frac{\partial U}{\partial x} = 0, \quad x \in \mathbb{R}, t > t_n, \quad (5.61a)$$

$$U(x, t_n) = u_j^n + s_j^n (x - x_j), \quad x \in V_j, \quad j = 0, \pm 1, \pm 2, \dots, \quad n = 0, 1, 2, \dots \quad (5.61b)$$

Analogous to (5.58), the numerical flux $F(u_j^n, u_{j+1}^n)$ is the time average of $\tilde{f}(U(x_{j+\frac{1}{2}}, t))$ over $[t_n, t_{n+1}]$, i.e.

$$F(u_j^n, u_{j+1}^n) = \frac{1}{\Delta t} \int_{t_n}^{t_{n+1}} \tilde{f}(U(x_{j+\frac{1}{2}}, t)) dt. \quad (5.62)$$

The computation of $U(x_{j+\frac{1}{2}}, t)$ from (5.61b) is straightforward, and, provided that $\tilde{a}_{j+\frac{1}{2}}^n > 0$, we obtain

$$U(x_{j+\frac{1}{2}}, t) = u_j^n + s_j^n \left(\frac{1}{2} \Delta x - \tilde{a}_{j+\frac{1}{2}}^n (t - t_n) \right), \quad (5.63)$$

and subsequently substituting this expression into (5.62), we find for the numerical flux

$$F(u_j^n, u_{j+1}^n) = f(u_j^n) + \frac{1}{2} \tilde{a}_{j+\frac{1}{2}}^n \left(1 - \frac{\Delta t}{\Delta x} \tilde{a}_{j+\frac{1}{2}}^n \right) \Delta x s_j^n. \quad (5.64)$$

Finally, we have to determine slopes s_j^n such that the resulting scheme is TVD. We do this using the technique of slope limiters. We take

$$s_j^n = \Phi_{j+\frac{1}{2}}^n \frac{1}{\Delta x} (u_{j+1}^n - u_j^n), \quad (5.65)$$

where $\Phi_{j+\frac{1}{2}}^n$ is a limiter on the slope $(u_{j+1}^n - u_j^n)/\Delta x$. Usually the limiter $\Phi_{j+\frac{1}{2}}^n$ is given by

$$\Phi_{j+\frac{1}{2}}^n = \Phi(r_{j+\frac{1}{2}}^n), \quad (5.66)$$

with $\Phi(r)$ the so-called limiter function and where $r_{j+\frac{1}{2}}^n$ is defined by

$$r_{j+\frac{1}{2}}^n := \frac{u_j^n - u_{j-1}^n}{u_{j+1}^n - u_j^n}, \quad (5.67)$$

provided that $\tilde{a}_{j+\frac{1}{2}}^n > 0$. More about these limiter functions can be found at the end of this section.

Finally, the numerical value u_j^{n+1} is defined as the average value of $U(x, t_{n+1})$ over V_j , i.e.

$$u_j^{n+1} := \frac{1}{\Delta x} \int_{V_j} U(x, t_{n+1}) dx. \quad (5.68)$$

Substituting (5.68) into (5.57) leads to the final scheme

$$u_j^{n+1} = u_j^n - \frac{\Delta t}{\Delta x} (F(u_j^n, u_{j+1}^n) - F(u_{j-1}^n, u_j^n)), \quad (5.69)$$

with the numerical flux $F(u_j^n, u_{j+1}^n)$ as in (5.64).

We conclude this derivation with mentioning three limiter functions. A smooth limiter function is due to Van Leer [46], and is given by

$$\Phi(r) = \frac{2r}{1+r}, \quad (5.70)$$

for $r > 0$. Another limiter function, especially suited for representing discontinuities, is the so-called superbee limiter function of Roe [35]. It is given by

$$\Phi(r) = \max(\min(1, 2r), \min(r, 2)), \quad (5.71)$$

for $r > 0$. The last limiter function we mention here is called the minmod limiter function (see [26]) and is given by

$$\Phi(r) = \max(0, \min(1, r)). \quad (5.72)$$

An elaborated example

We take the case of no solidification as an example. That is, we only look at the movement of the liquid blob. We use Eqs. (5.31) and (5.32) without the solidification term $\frac{\partial \psi}{\partial t}$, i.e.

$$\frac{\partial \xi}{\partial t} + \frac{\partial(u\xi)}{\partial x} = 0, \quad (5.73a)$$

and

$$\frac{\partial u}{\partial t} + \frac{\partial(\frac{1}{2}u^2)}{\partial x} = 0. \quad (5.73b)$$

The initial conditions to go with these equations are prescribed geometry and a prescribed velocity

$$\xi(x, 0) = \tilde{\xi}(x), \quad u(x, 0) = \tilde{u}(x). \quad (5.74)$$

Eqs. (5.73) are both in the form as in (5.54) and we therefore use the slope limiter method on both equations to solve this.

Burgers' equation

Following the derivation of the slope limiter scheme as in the previous section with $f(u) = \frac{1}{2}u^2$ we get the scheme

$$u_j^{n+1} = u_j^n - \frac{\Delta t}{\Delta x} (F(u_j^n, u_{j+1}^n) - F(u_{j-1}^n, u_j^n)), \quad (5.75)$$

with numerical flux $F(u_j^n, u_{j+1}^n)$ given by

$$F(u_j^n, u_{j+1}^n) = \frac{1}{2}(u_j^n)^2 + \frac{1}{2}\tilde{a}_{j+\frac{1}{2}}^n \left(1 - \frac{\Delta t}{\Delta x}\tilde{a}_{j+\frac{1}{2}}^n\right) \Delta x s_j^n, \quad (5.76)$$

where

$$\tilde{a}_{j+\frac{1}{2}}^n = \frac{\frac{1}{2}((u_{j+1}^n)^2 - (u_j^n)^2)}{u_{j+1}^n - u_j^n} = \frac{1}{2}(u_{j+1}^n + u_j^n). \quad (5.77)$$

We can employ this scheme starting from the known initial velocity distribution $u(x, 0) = \tilde{u}(x)$.

Mass balance

For the mass balance equation (5.73a) we get the scheme

$$\xi_{j+1}^n = \xi_j^n - \frac{\Delta t}{\Delta x} (F(\xi_j^n, \xi_{j+1}^n) - F(\xi_{j-1}^n, \xi_j^n)), \quad (5.78)$$

with numerical flux $F(\xi_j^n, \xi_{j+1}^n)$ given by

$$F(\xi_j^n, \xi_{j+1}^n) = u_j^n \xi_j^n + \frac{1}{2} \tilde{a}_{j+\frac{1}{2}}^n \left(1 - \frac{\Delta t}{\Delta x} \tilde{a}_{j+\frac{1}{2}}^n \right) \Delta x s_j^n, \quad (5.79)$$

where

$$\tilde{a}_{j+\frac{1}{2}}^n = u_{j+\frac{1}{2}}^n. \quad (5.80)$$

The numerical scheme for this elaborated example is depicted in Figure 5.3.

Results

The analytical results for this system of equations as stated in Section 5.3.1 are clearly visible in the numerical results. We see the asymptotic triangular profile of the velocity distributions and the corresponding melt accumulation at the leading edge shock.

We will use the finite element method for solving the heat equation (5.53)

$$\frac{\partial \eta}{\partial t} + \chi u \frac{\partial \theta}{\partial x} + \chi \left\{ \frac{\partial}{\partial x} (u\psi) - \frac{\partial u}{\partial x} \psi \right\} \frac{\partial \theta}{\partial y} - D \frac{\partial^2 \theta}{\partial y^2} = 0, \quad (5.81)$$

together with the no flux boundary condition on temperature (5.36), ambient conditions at infinity (5.40) and the initial condition (5.42). Furthermore the relationship between the enthalpy η and the temperature θ is described by (5.49) and (5.50).

We search for a weak solution of (5.81). Multiply (5.81) with a weight function p which vanishes on Γ_1 and integrate over the domain. Using the divergence theorem we get the finite element variational formulation

$$\int_{\Omega} \frac{\partial \eta}{\partial t} p + \chi u p \frac{\partial \theta}{\partial x} + \chi \left\{ \frac{\partial}{\partial x} (u\psi) - \frac{\partial u}{\partial x} \psi \right\} p \frac{\partial \theta}{\partial y} + D \frac{\partial p}{\partial y} \frac{\partial \theta}{\partial y} d\sigma = \int_{\Gamma} D p \frac{\partial \theta}{\partial y} n_y ds = 0 \quad \text{for all } p \in H_0^1. \quad (5.82)$$

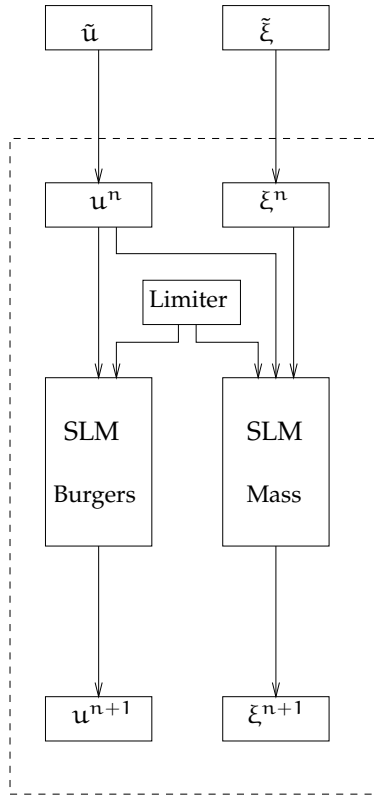


Figure 5.3: The numerical scheme for the elaborated example. The dashed box stands for the loop.

Here the last equality comes from the boundary condition of θ on Γ_3 (5.36) and the fact that $p|_{\Gamma_1} \equiv 0$.

Next, we consider a finite element discretization of Ω with a finite element space $V_h \subset H_0^1(\Omega)$ spanned by the basis $\{\varphi_i\}_{i=1}^N$. A typical choice for the basis functions would be the hat functions. We look for finite element solutions

$$\tilde{\eta}(\mathbf{x}, t) = \eta^{\Gamma_1} + \eta^{\overline{\Omega} \setminus \Gamma_1} = \eta^{\Gamma_1} + \sum_{i=1}^N \eta_i(t) \varphi_i(\mathbf{x}) \quad (5.83)$$

and

$$\tilde{\theta}(\mathbf{x}, t) = \theta^{\Gamma_1} + \theta^{\overline{\Omega} \setminus \Gamma_1} = \theta^{\Gamma_1} + \sum_{i=1}^N \theta_i(t) \varphi_i(\mathbf{x}). \quad (5.84)$$

The superscript Γ_1 is used to indicate that the inhomogeneous Dirichlet boundary conditions at Γ_1 are fulfilled by this term.

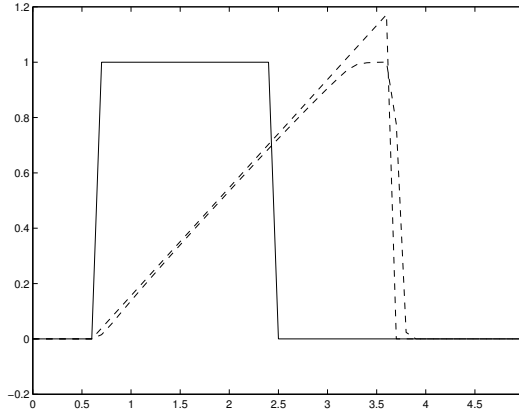


Figure 5.4: *The evolution of the velocity profile*

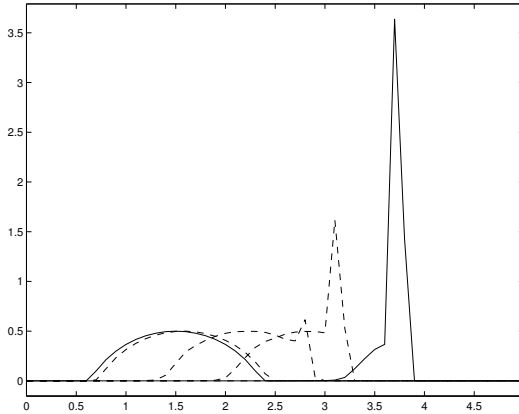


Figure 5.5: *The evolution of the melt drop*

The computational problem is to determine the time dependent coefficients $\eta_i(t)$ and $\theta_i(t)$ for $i = 1, \dots, N$. Substituting the approximations into the variational formulation and taking the weight functions to be the basis functions φ_j , $j = 1, \dots, N$ we obtain the set of equations in matrix form

$$\mathbf{M} \frac{d\boldsymbol{\eta}}{dt} + \mathbf{C}(\mathbf{u}, \boldsymbol{\psi}) \boldsymbol{\theta} + \mathbf{D}\mathbf{S}\boldsymbol{\theta} = \mathbf{b}. \quad (5.85)$$

We use the bold face characters for matrices and vectors. So, $\boldsymbol{\eta} = [\eta_i(t)]$ and $\boldsymbol{\theta} = [\theta_i(t)]$. The mass matrix \mathbf{M} , the convection matrix \mathbf{C} , the stiffness matrix \mathbf{S} and the right-hand side \mathbf{b} are defined as follows:

$$[\mathbf{M}]_{ij} = \int_{\Omega} \varphi_i \varphi_j d\sigma, \quad (5.86a)$$

$$[\mathbf{C}]_{ij} = \int_{\Omega} \chi u \varphi_i \frac{\partial \varphi_j}{\partial x} + \chi \left\{ \frac{\partial}{\partial x} (u\boldsymbol{\psi}) - \frac{\partial u}{\partial x} \mathbf{y} \right\} \varphi_i \frac{\partial \varphi_j}{\partial y} d\sigma, \quad (5.86b)$$

$$[\mathbf{S}]_{ij} = \int_{\Omega} \frac{\partial \varphi_i}{\partial y} \frac{\partial \varphi_j}{\partial y} d\sigma, \quad (5.86c)$$

$$[\mathbf{b}]_i = - \int_{\Omega} \chi u \varphi_i \frac{\partial \theta^{\Gamma_1}}{\partial x} + \chi \left\{ \frac{\partial}{\partial x} (u\psi) - \frac{\partial u}{\partial x} y \right\} \varphi_i \frac{\partial \theta^{\Gamma_1}}{\partial y} + D \frac{\partial \theta^{\Gamma_1}}{\partial y} \frac{\partial \varphi_i}{\partial y} d\sigma. \quad (5.86d)$$

Together with the initial conditions on temperature (5.42) and hence via the relationship also on enthalpy, we have a set of initial value problems which can be solved numerically.

In order to show how we solve (5.85) by the ϑ -method, we rewrite it as

$$\mathbf{M} \frac{d\boldsymbol{\eta}}{dt} = \mathcal{F}(u, \psi, \boldsymbol{\eta}, t) := \mathbf{b} - \mathbf{C}(u, \psi)\boldsymbol{\theta}(\boldsymbol{\eta}) - D\mathbf{S}\boldsymbol{\theta}(\boldsymbol{\eta}). \quad (5.87)$$

Suppose everything is known at $t = t^k$. The enthalpy distribution and temperature distributions in the material at time $t = t^{k+1}$ are then computed by the ϑ -method. We obtain

$$\begin{aligned} \mathcal{G}(\boldsymbol{\eta}^{k+1}) &:= \mathbf{M}(\boldsymbol{\eta}^{k+1} - \boldsymbol{\eta}^k) \\ &\quad - \Delta t (\vartheta \mathcal{F}(u^{k+1}, \psi^{k+1}, \boldsymbol{\eta}^{k+1}, t^{k+1}) + (1 - \vartheta) \mathcal{F}(u^k, \psi^k, \boldsymbol{\eta}^k, t^k)) = 0. \end{aligned} \quad (5.88)$$

In order to solve (5.88) for $\vartheta \neq 0$, the occurrence of $\boldsymbol{\eta}^{k+1}$ does not cause problems; this could be dealt with in a similar way as in the melting model, see the previous chapter. The problem for $\vartheta \neq 0$ lies in the ψ^{k+1} and u^{k+1} terms.

For $\vartheta = 0$ the procedure is simply the following. Compute the enthalpy distribution in the material at time $t = t^{k+1}$ via

$$\mathbf{M}\boldsymbol{\eta}^{k+1} = \mathbf{M}\boldsymbol{\eta}^k + \Delta t \mathcal{F}(u^k, \psi^k, \boldsymbol{\eta}^k, t^k), \quad (5.89)$$

and then update the temperature via (5.49) to get

$$\theta_i^{k+1} = \theta(\eta_i^{k+1}). \quad (5.90)$$

The position of the solid-liquid boundary ψ at time level $t = t^{k+1}$ is simply the melting isotherm.

For $\vartheta \neq 0$ we can use a quasi Newton method. That is, we freeze the u and ψ terms

$$\tilde{\mathcal{G}}(\boldsymbol{\eta}^{k+1}) := \mathbf{M}(\boldsymbol{\eta}^{k+1} - \boldsymbol{\eta}^k) - \Delta t (\vartheta \mathcal{F}(u^k, \psi^k, \boldsymbol{\eta}^{k+1}, t^{k+1}) + (1 - \vartheta) \mathcal{F}(u^k, \psi^k, \boldsymbol{\eta}^k, t^k)) = 0. \quad (5.91)$$

The iteration to obtain the solution at $t = t^{k+1}$ is as follows

$$\begin{cases} \boldsymbol{\eta}^{k+1, l} = \boldsymbol{\eta}^{k+1, l-1} - (\partial \tilde{\mathcal{G}}(\boldsymbol{\eta}^{k+1, l-1}))^{-1} \tilde{\mathcal{G}}(\boldsymbol{\eta}^{k+1, l-1}), & l = 1, 2, \dots, \\ \boldsymbol{\eta}^{k+1, 0} = \boldsymbol{\eta}^k. \end{cases} \quad (5.92)$$

This is similar to the method used in the previous chapter in solving the enthalpy problem for laser induced melting. The difference lies in the operator \mathcal{G} . Here, the Jacobian $\partial\tilde{\mathcal{G}}(\boldsymbol{\eta})$ is given by

$$\partial\tilde{\mathcal{G}}(\boldsymbol{\eta}^{k+1,*}) = \mathbf{M} + \Delta t \vartheta (\mathbf{C}(\mathbf{u}^k, \psi^k) - \mathbf{DS}) \frac{\partial\theta}{\partial\boldsymbol{\eta}}(\boldsymbol{\eta}^{k+1,*}). \quad (5.93)$$

The iteration in (5.92) is stopped when a given accuracy is reached.

After one complete time step for both the enthalpy problem and the two slope limiter schemes has been calculated, we will need to adapt the domain of computation. One has to be aware of the fact that as the liquid moves and the solid obviously does not, interpolating the old solution on the new domain is a point of attention.

Computational platforms

In the numerical procedures outlined in the previous chapters, several solution algorithms are used. Each algorithm consists of a sequence of operations on specific data. Most of these operations are available as part of public domain or commercial *libraries* (collections of operations) or as operating system commands. However, different libraries tend to use different data structures and most computational libraries were not written with visualization in mind. The same holds for the visualization of the results, which is a very important aspect in simulation. Several user friendly and extensive libraries for visualization are available. Preferably we want to use these existing and often well documented libraries together. This chapter shows how this is achieved by adorning existing libraries with an interface within the NumLab visual programming environment (see [28]). Section 6.1 shows how the to be introduced interface can be used to implement complex numerical algorithms in a convenient manner. The setup of such an interface is treated in Section 6.2 using the example of the Piecewise Polynomial Package, PPPack [10].

6.1 Scientific computing

The focus for the implementation of complex numerical algorithms must be on the reuse of existing unaltered libraries. Most libraries use own (i.e. non-standard) data structures so that they cannot be used jointly. Therefore, these libraries do not seem to aid to the implementation of complex numerical problems. In order to use libraries within a broader framework, these libraries need to communicate with each other in some way. Basically, a library is a collection of operations on a specific data type and normally different libraries use different data types. Within the NumLab visual programming environment communication between different libraries is achieved by equipping all "outside" libraries with an interface ensuring that the library accepts the same (common) data type, as depicted in Fig. 6.1 for the solidification problem of Section 5.3. The outer circles denote the used existing "outside"

libraries, the grey shells denoting their interfaces. The arrows denote the data flow between the libraries and the solidification program. The inner circle is the numerical solution procedure for the solidification problem encoded within NumLab. The

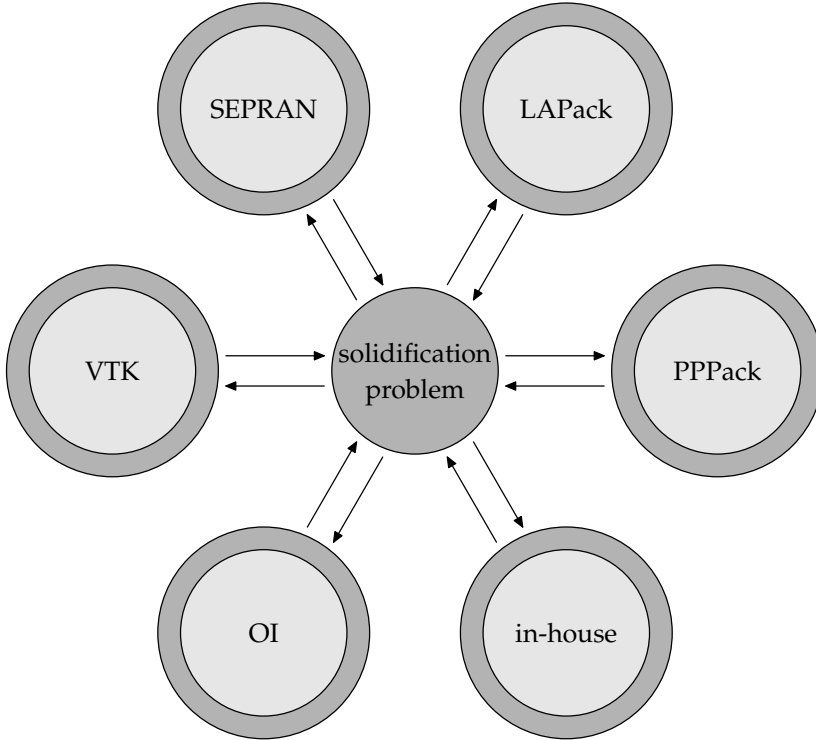


Figure 6.1: Schematic overview of the numerical procedure of the solidification problem within NumLab.

transformation of the generic NumLab data type to the library specific data type is provided within the library interface. This interface provides additional functionality, see [13], which is beyond the scope of this thesis. The interface enables us to use the existing libraries in an unaltered way and, furthermore, within a visual programming environment.

For each of the solidification's subproblems, numerical solution procedures exist. Thus, the problem can be solved with a combination of the operations, which reside in different libraries, as shown in Fig. 6.1. The finite element package SEPRAN [37] builds the system of equations resulting from the finite element formulation of the problem, see Section 5.3. The Linear Algebra Package LAPack [2] routines are then used to solve the system. On the other hand, the solid-liquid interface as well as the surface are represented by smooth splines using the Piecewise Polynomial Package PPPack [10] and the positions of these moving boundaries are calculated using in-house written finite volume codes, see Section 5.3. The results are visualized using

the Visualization ToolKit (VTK) [36] and Open Inventor (OI) [50] libraries. The need for some sort of communication between these different packages and libraries is obvious.

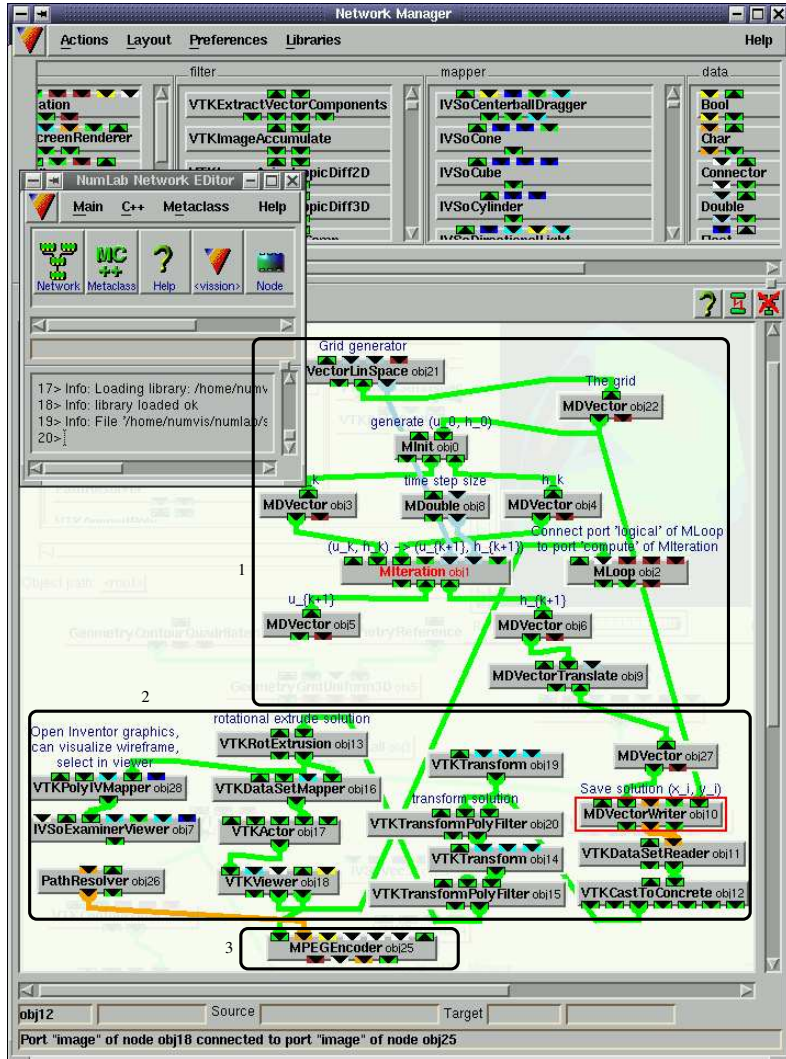


Figure 6.2: The program which solves a part of the solidification problem and visualizes the output.

Figure 6.2 shows the implementation of the problem described by Eq. (5.73) as derived in Section 5.3, loaded into the NumLab visual programming environment, see [28]. The implementation uses *modules* (we use the word module for both operations and data structures) from different libraries including LAPack, PPPack, VTK, OI, etc., as well as operating system commands: the `mpeg` module. Most numerical programs, like the one in Fig. 6.2, can be divided into three parts:

1. the part which reads the input and performs the numerical computations,
2. the part which visualizes the computed results and
3. the post-processing part which writes the output.

Figure 6.2 needs further explanation. Each rectangle such as `MIteration` is a graphical representation of an operation belonging to a certain library. For the sake of convenience, this representation is also called a *module*. Within each module, we discern a bottom and a top area. Modules may have both input and output arguments. Each of its arguments made available via the interface description, is mapped onto a small coloured rectangular area at the bottom or top of the module, the input arguments being related to the top, the output arguments to the bottom. These small rectangular regions are called *ports*. Different built-in data types are coloured in a different manner, all pointers and derived types are coloured using a default. Each port is either connected, or behind the scenes a default value is used. Output is connected to input using the mouse by clicking on the bottom output port, dragging to the top input port and releasing. The connection is established when the data types concur, and refused when this is not the case. Default values can be altered using a graphical user interface, called the *interactor* (Fig. 6.3), which is automatically generated from the function's interface, and which pops up when selected. This automatically built editor can be used to enter the values of arguments which are not connected. As

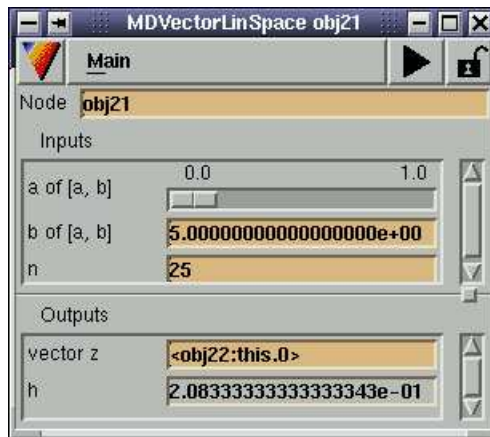


Figure 6.3: The user provides default values to the modules using an automatically built editor.

an example, see Fig. 6.3, which shows the equivalent of the Matlab `linspace` functionality. We can prescribe an interval $[a, b] \subset \mathbb{R}$ and a number of points $n \in \mathbb{N}$ and the module generates a vector $z \in \mathbb{R}^n$ of n points linearly spaced between, and including, a and b , as well as the spacing h .

Figure 6.4 depicts a VTK Viewer, belonging to a VTK Viewer module, which shows the initial shape of the melt blob flowing along the walls, superimposed with graph-

ical operations onto the inside of a cylinder wall. This VTK viewer as well as the OI viewer offers solid, hidden-line, wire-frame and other representations, as well as interactive 3D manipulation of the visualized objects.

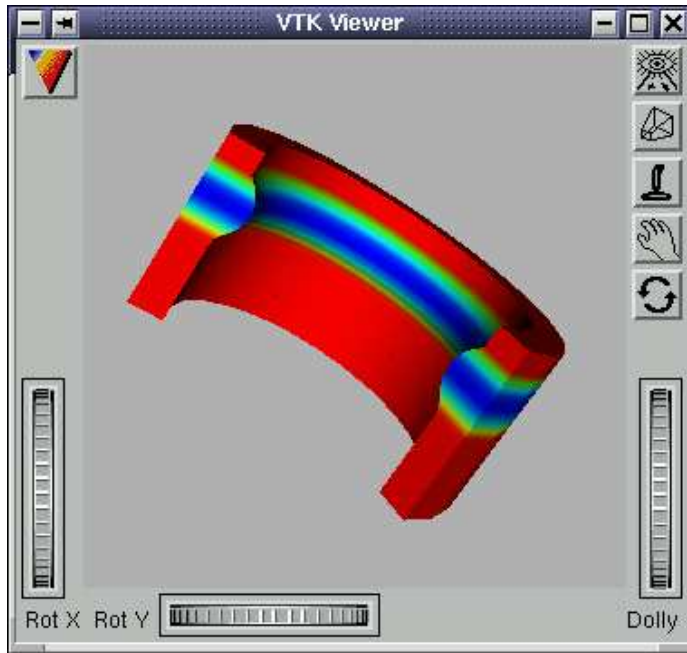


Figure 6.4: *Visualization of the solidification process.*

Building complex numerical algorithms with NumLab is convenient because of a number of reasons. Firstly, the libraries LAPack, EigPack, SEPRAN, PPPack, VTK, OI, etc. have been interfaced and can therefore be used together without restrictions and explicit user data type conversions. In the example discussed in this section, we used SEPRAN and PPPack to build the equations, LAPack to solve them and VTK to visualize the results. Secondly, several methods have been added to the NumLab computational platform, like new data-types, data-exchange in MATLAB / Mathematica / Open-Math / LaTeX / VTK / other formats, and discretized ordinary and partial differential related operators. Furthermore, programming in a visual environment aids to the reusability of complex numerical algorithms.

6.2 Example

For this NumLab environment as sketched above, we show how to interface an existing library. For a more thorough explanation of this technique, see [27] and references therein. Interfacing a library means interfacing all operations to be exposed for usage. In this example we show how to interface the PPPack [10] to generate an interpolating cubic spline (see e.g. [11]). The language in which the interface is

Function	Description
dcubspl	computes polynomial coefficients of cubic spline
dppvalu	computes function or derivative value of cubic spline
dinterv	function used in dppvalu

Table 6.1: The operations from the PPPack library needed for NumLab spline operations.

implemented is C++, for reasons that are outlined in [27]. The interface consists of three layers, the *source-layer*, the *class-layer* and the *module-layer*.

The source-layer contains the operations from the libraries which the user wants to use, i.e. it is closest to the "white" inner region of the library in Fig. 6.1. For the cubic spline, these are given in Table 6.1. The `dcubspl` routine computes the polynomial coefficients describing the interpolating cubic spline and writes these to a matrix `C`. For this it basically needs three groups of input, the first and second being the abscissae and ordinates of the data points, respectively, and the third describing the boundary conditions in terms of type and value. Once the spline has been built, its function or derivative value at a point x can be computed from the matrix `C` using the `dppvalu` routine. The `dinterv` routine is merely an operation used repeatedly within `dppvalu`. Because Fortran generates function names according to a different rule than C++, we need to provide each Fortran function we want to use within our C++-interface with a shell that ensures that the Fortran function is called.

The class-layer contains the C++ class version of a cubic spline. Its constructor calls back to the `dcubspl` routine in the source-layer and checks whether this went correctly. The function value or j -th derivative value of the cubic spline can be obtained using the `operator()`. If `spline` is an instance of the spline class, then `spline(x)` and `spline(x, j)` return the function value and the value of the j -th derivative of the spline in point x , respectively. This `operator()` calls back to the `dppvalu` routine.

Finally, the module-layer contains a class. This so called *module* delegates all operations to the class-level and, moreover, is adorned with a few standard data-flow operations for use in a visual programming environment. This module-layer makes the spline class accessible within a visual programming environment through the graphical representation as depicted in Fig. 6.5. This module has eight ports on the

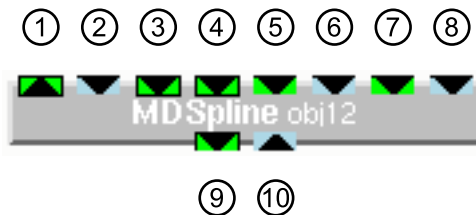


Figure 6.5: The spline module. Please consult the text for further explanation.

top and two at the bottom. The first port on both the top ① and the bottom ⑨ is a pointer to the instance of the class itself. The other top ports represent the input arguments: the point x at which the spline should be evaluated ②, the abscissae ③ and ordinates ④ of the data points and the type and value of the left (⑤ and ⑥) and right (⑦ and ⑧) boundary conditions. The second port at the bottom ⑩ is the function value of the cubic interpolating spline at point x .

Figure 6.6 shows a network in which a spline through three data points is generated. The boundary conditions used to generate the cubic spline are shown in the interactor. This interactor also shows the benefit visual programming environments have over non-graphical ones: all required input data is shown in a clear way. The type of boundary condition is chosen through a pull-down menu with enumerative types with descriptive names such as `Dx` converted to an integer for the Fortran routine `dcubspl`, which needs an integer describing the type. The resulting spline is visualized using the `MDFxSampler` module, which input arguments are a function, in this case the cubic spline function, and a vector, in this case a uniform gridding of the interval $[-1, 1]$. The output of the sampler module is a vector containing the function values at these abscissae. These two vectors can be visualized using VTK operations resulting in the VTK Viewer window as shown in the figure.

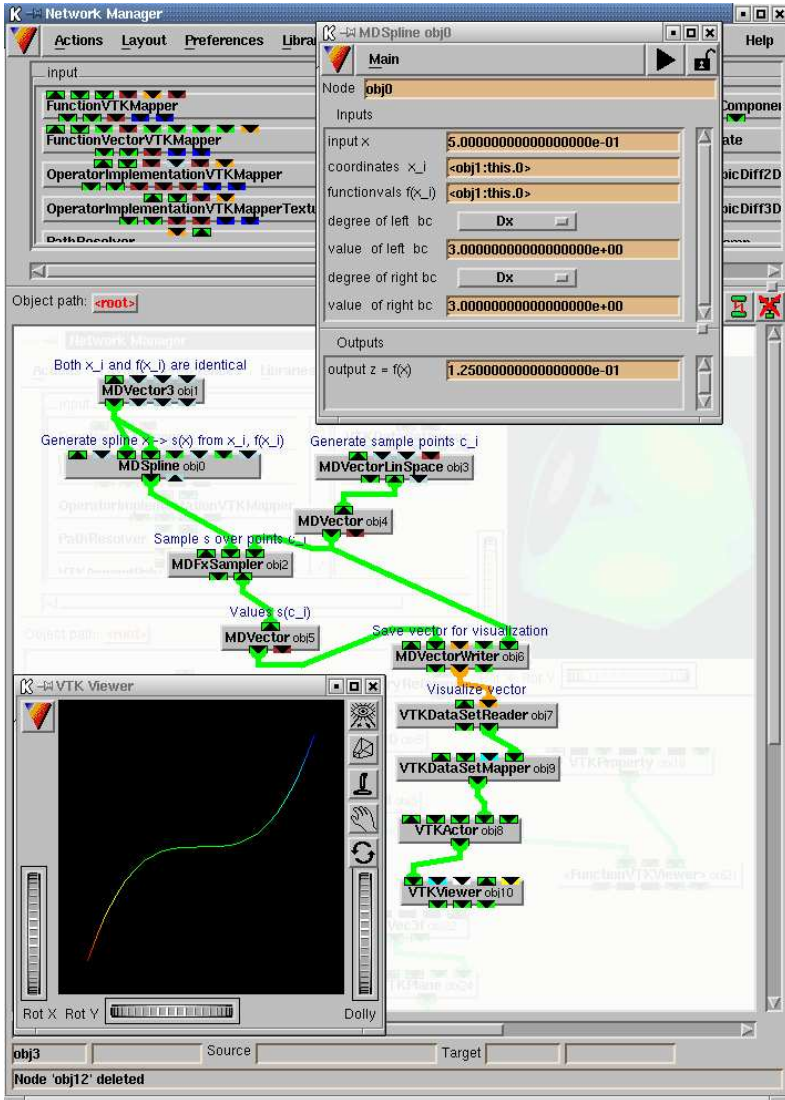


Figure 6.6: The spline module within a network.

Conclusions and Recommendations

Numerous experiments show that most of the material removed during a laser percussion drilling process is in liquid state. This observation leads to the conclusion that modelling laser induced melting is essential in a thorough understanding of the drilling process. In this thesis the melting is investigated intensively and, moreover, also the resolidification of this molten material during splashing is studied. One of the main conclusions of this thesis is that the melting model reveals a small time scale in which the material reaches vaporisation temperature. Taking the scales for the gas dynamics and the splashing into consideration, multiple cycles of heating-splashing per pulse may be expected. The number of cycles per pulse depends on material properties and laser settings. Furthermore, the velocities for the expelled melt predicted from a simplified gas dynamics model are already in good agreement with observations.

From the analysis of the two mathematical formulations of melting investigated in this thesis, it follows that the enthalpy method is far more suitable for more dimensional problems. Due to the fact that tracking the solid-liquid interface is an essential part of the formulation that makes use of the Stefan condition, this poses severe problems in implementation for more-dimensional problems. Moreover, the enthalpy method is also more suited for one-dimensional methods when initially only one of the phases is present. The main advantage of the enthalpy method over the method employing the Stefan condition is that the position of the interface is known a posteriori; it is merely an isotherm. Although this enthalpy method is known since the early eighties we did not find papers concerning modelling of the laser drilling process that use this method.

The understanding of the incoupling of energy is essential in modelling laser percussion drilling. The total amount of energy absorbed by the material is the key

parameter in the process. The incoupling of energy is governed by the reflectivity behaviour of the material under irradiation. However, most publications on modelling the laser-drilling process either do not use a reflection model or use an oversimplified reflection model. In this thesis we use the Algebraic Ray Trace Method (ARTM) to give the actual incoupling of laser energy into the material. This reflectivity model easily explains the role the wavelength of the laser has on the outcome of the process, e.g. a different wavelength can easily increase the incoupling of laser energy from only 5% to over 50%. It is therefore obvious, that the optical behaviour of the material should be investigated thoroughly to get a more efficient laser drilling process. Furthermore, the reflection model easily explains both tapering of holes due to reflections of steep sides and better incoupling of energy in deeper holes.

Using the results of the reflection model as input of the laser-induced melting model a relatively simple simulation model has been built. By this simulation model one can investigate the influence of different laser settings to the process. These laser settings do not have to be conform to existing laser settings. Indeed, one can try to find the optimal laser together with its settings for a specific desirable result. Instead of expensive testing, one can thus get a better understanding of the role of the various laser parameters.

The solidification model derived in this thesis tells us that a shock may be expected within the melt flowing along the relatively cold sides. This study explains why experimentally observed local clumps of resolidified material may arise in the drilled hole during the laser percussion drilling process. With reliable experimental and material data, it may even predict a typical length at which such a clump can be expected. The versatility of the model is shown by the fact that with only a few modifications the solidification model can also be used to predict the solidification of a lava flow.

Another conclusion that can be drawn from this thesis is that it is very helpful to use existing and unaltered libraries to implement complex numerical algorithms. The software package NumLab is very instrumental in this and, moreover, offers this within a visual programming environment thereby enhancing the reuseability as well as the user-friendliness of the program. To be able to use "outside" libraries in an unaltered way, these libraries are equipped with an interface in which, amongst others, the translation of the NumLab datatype to the library-own datatype and vice versa is provided.

Evidently, because of the complexity of the process, although many phenomena are treated in this thesis, a simulation model will never be covering all aspects. However, we will make some recommendations to enhance the modelling of laser percussion drilling in the following. A first recommendation is based upon an assumption made in the beginning of this thesis. From a computational point of view we have restricted ourselves to axisymmetric geometries. However, the pumping for a Nd:YAG laser is done by flash lamps. In this process the medium is heated up considerably and because of thermal effects beam distortions become serious. Because of a non-axisymmetric lay-out of the laser the thermal effects lead to a non-Gaussian

laser beam. This beam is essentially non-axisymmetric and therefore computations should be performed on a three-dimensional mesh to get better results.

The splashing mechanism is an extremely interesting and complex subject on itself. It was beyond the scope of this thesis to study this subject into all its details. However, a thorough study is needed to get a full understanding of the process of recasting. For this, experiments would be needed to acquire qualitative and quantitative information about the behaviour of the material under consideration in all its phases. This last remark also leads to a third and final recommendation. We have neglected the absorption of laser energy by the vapour cloud for laser settings in the range we studied. However, as lasers are becoming more and more powerful energy sources, in the near future it may very well be not negligible any more for industrial lasers. A thorough understanding of this absorption is needed and furthermore, a plasma may even be used to achieve a better incoupling of energy into the material. The ARTM will prove to be an instrumental tool for this, because, in contrast to normal ray trace methods, absorption of energy within the medium can be incorporated into the model easily. In fact, it was derived to do just that for radiation in glass.

Bibliography

- [1] M. von Allmen and A. Blatter. *Laser-beam interactions with materials*. Springer-Verlag, 1995.
- [2] E. Anderson, Z. Bai, C. Bischof, et al. *LAPACK user's guide*. SIAM Philadelphia, 1995.
- [3] S. Anisimov. Vaporization of metal absorbing laser radiation. *Soviet Physics JETP*, 27:182–183, 1968.
- [4] N.S. Asaithambi. A Galerkin method for Stefan problems. *Appl. Math. Comp.*, 52:239–250, 1992.
- [5] M. Born and E. Wolf. *Principles of optics*. Pergamon Press, fifth edition, 1975.
- [6] J. Crank. *Free and moving boundary problems*. Clarendon Press, 1984.
- [7] A.J. Dalhuijsen and A. Segal. Comparison of finite element techniques for solidification problems. *Internat. J. Numer. Methods Engrg.*, 23:1807–1829, 1986.
- [8] B.N. Datta. *Numerical linear algebra and applications*. Brooks/Cole, 1995.
- [9] G. Davies, editor. *Properties and Growth of Diamond*. Number 9 in EMIS Datareview series. INSPEC, 1994.
- [10] C. de Boor. *Piecewise polynomial package*. <http://www.netlib.org/pppack>.
- [11] C. de Boor. *A practical guide to splines*. Number 27 in Applied Mathematical Sciences. Springer-Verlag, 1978.
- [12] J. Dowden, M. Davis, and P. Kapadia. Some aspects of fluid mechanics of laser welding. *J. Fluid Mech.*, 126:123–146, 1983.
- [13] W. Drenth. *A platform for numerical computations with special application to preconditioners*. PhD thesis, Eindhoven University of Technology, to appear 2003.
- [14] W.G. Driscoll and W. Vaughn, editors. *Handbook of Optics*. McGraw-Hill, New York, 1978. pp. 10-9–10-10.

- [15] C.M. Elliot and J.R. Ockendon. *Weak and variational methods for moving boundary problems*. Research notes in mathematics. Pitman, 1981.
- [16] J.E. Field, editor. *The Properties of Diamond*. Academic Press, London, 1979.
- [17] M.C. Fowler and D.C. Smith. Ignition and maintenance of subsonic plasma waves in atmospheric pressure air by CW CO₂ laser radiation and their effect on laser beam propagation. *J. Appl. Phys.*, 46:138–150, 1975.
- [18] R.K. Ganesh and A. Faghri. A generalized thermal modeling for laser drilling process–I. Mathematical modeling and numerical methodology. *International Journal of Heat Mass Transfer*, 40(14):3351–3360, 1997.
- [19] R.K. Ganesh and A. Faghri. A generalized thermal modeling for laser drilling process–II. Numerical simulation and results. *International Journal of Heat Mass Transfer*, 40(14):3361–3373, 1997.
- [20] A. Harten. High resolution schemes for hyperbolic conservation laws. *J. Comput. Phys.*, 49:357–393, 1983.
- [21] E. Hecht. *Optics*. Addison-Wesley, 1998.
- [22] H. Ki, P.S. Mohanty, and J. Mazumder. Multiple reflection and its influence on keyhole evolution. *Journal of laser applications*, pages 39–45, 2002.
- [23] C.J. Knight. Theoretical modeling of rapid surface vaporization with back pressure. *AIAA Journal*, 17(5):519–523, 1979.
- [24] L.D. Landau and E.M. Lifschitz. *Statistical Mechanics*. Pergamon, New York, 1980.
- [25] H.W. Liepmann and A. Roshko. *Elements of gasdynamics*. John Wiley & Sons, inc., 1960.
- [26] R.M.M. Mattheij, S.W. Rienstra, and J.H.M ten Thije Boonkamp. *Partial differential equations Modelling, Analysis, Computing*. SIAM, Philadelphia, to appear in 2003.
- [27] J. Maubach and W. Drenth. Data-flow oriented visual programming libraries for scientific computing. Rana 01-30, Eindhoven University of Technology, 2001.
- [28] J. Maubach and A. Telea. The NUMLAB numerical laboratory for computation and visualisation. *Computing and Visualization in Science*, 2001. accepted.
- [29] M. Mori. *The finite element method and its applications*. Macmillan publishing company, New York, 1986.
- [30] M.J. Noot. *Numerical analysis of turbine blade cooling ducts*. PhD thesis, Eindhoven University of Technology, 1997.
- [31] H. Ockendon and A.B. Tayler. *Inviscid fluid flows*. Springer-Verlag, 1983.
- [32] E.D. Palik, editor. *Handbook of optical constants of solids*. Academic Press, New York, 1998.

- [33] P.D. Patel. Interface conditions in heat-conduction problems with change of phase. *AIAA Journal*, 6:2454, 1968.
- [34] K. Ražnjević. *Handbook of thermodynamic tables and charts*. McGraw-Hill, 1976.
- [35] P.L. Roe. Some contributions to the modeling of discontinuous flows. *Lect. Notes Appl. Math.*, 22:163–193, 1985.
- [36] W. Schroeder, K. Martin, and B. Lorenzen. *The visualization toolkit: an object-oriented approach to 3D graphics*. Prentice Hall, 1995.
- [37] G. Segal. *The SEPRAN finite element package*. <http://ta.twi.tudelft.nl/sepran/sepran.html>.
- [38] R. Siegel and J.R. Howell. *Thermal radiation heat transfer*. Taylor & Francis, third edition, 1992.
- [39] A.E. Siegman. *An introduction to lasers and masers*. McGraw-Hill, 1971.
- [40] A.E. Siegman. *Lasers*. Oxford University Press, 1986.
- [41] W.R. Smith. Models for solidification and spalling in laser percussion drilling. Rana 00-09, Eindhoven University of Technology, 2000.
- [42] W.M. Steen. *Laser material processing*. Springer-Verlag, 1991.
- [43] J. Stefan. Über die Theorie der Eisbildung, insbesondere über die Eisbildung im Polarmeere. *Annalen der Physik und Chemie*, 42:269, 1891.
- [44] K.H. Tacke. Discretization of the explicit enthalpy method for planar phase change. *Internat. J. Numer. Methods Engrg.*, 21:543–554, 1985.
- [45] Bas J. van der Linden. *The algebraic ray trace method*. PhD thesis, Eindhoven University of Technology, 2002.
- [46] B. van Leer. Towards the ultimate conservative difference scheme ii. monotonicity and conservation combined in a second order accurate scheme. *J. Comput. Phys.*, 14:361–370, 1974.
- [47] J.C.J. Verhoeven. Modelling of a laser percussion drilling process. Master's thesis, Eindhoven University of Technology, 1998.
- [48] V. Voller and M. Cross. Accurate solutions of moving boundary problems using the enthalpy method. *International Journal of Heat Mass Transfer*, 24:545–556, 1981.
- [49] V. Voller and M. Cross. An explicit method to track a moving phase change front. *International Journal of Heat Mass Transfer*, 26:147–150, 1983.
- [50] J. Wernecke. *The inventor mentor: programming object-oriented 3D graphics with Open Inventor*. Addison-Wesley, 1993.
- [51] G.B. Whitham. *Linear and Nonlinear Waves*. John Wiley, New York, 1974.
- [52] M. Zerroukat and C.R. Chatwin. *Computational Moving Boundary Problems*. Applied and Engineering Mathematics Series 8. John Wiley, New York, 1994.

Index

- airfoil, 1
- algebraic ray trace method, *see* ARTM
- amplitude reflection coefficient, 53
- ARTM, 51, 56–60
- barreling, 7
- bellow shape, 7
- blade, 2
- Brinkman number, 23
- channeling, 55
- class-layer, 98
- Clausius-Clapeyron equation, 20
- discrete ordinate method, *see* DOM
- DOM, 57
- dross, 7
- effective indices
 - method of –, 54
- enthalpy, 33
 - problem, 31, 33–35, 41–43
- evanescent wave, 53
- extinction coefficient, 52
- fan, 1
- Fresnel equations, 53
- Froude number, 23
- index of refraction
 - complex –, 52
 - simple –, 52
- interactor, 96
- keyhole, 62
- laser drilling
 - diamond, 63
 - percussion, 6
 - single pulse, 6
 - trepanning, 6
- latent heat, 33
 - of fusion, 32, 33
- library, 93
- liquidus, 33
- module, 96, 98
- module-layer, 98
- modules, 95
- mushy region, 33
- Nd:YAG, 13
- NumLab, 93
- Peclet number, 23
- ports, 96
- Prandtl number, 23
- Rankine-Hugoniot, 19
- Rankine-Kirchhoff equation, 20
- ray tracing, 58
- recast layer, 7, 12
- recoil pressure, 11
- reflection
 - coefficient, 53
 - Huygens’ law of –, 52
 - specular –, 52
- reflectivity, 53–55
 - directional –, 53
- relaxation time, 13
- Reynolds number, 22
- sensible heat, 33
- Snell’s Law, 52
- solidus, 33
- source-layer, 98

spatter, 7

Stefan, 31

 condition, 31–33, 35–41

 problem, 31

tapering, 7

TEM₀₀-mode, 13

time envelope, 67

time scales, 12

TIT, 2

turbine inlet temperature, *see* TIT

vane, 2

VSM-number, 14

waist, 13, 67

Weber number, 23

Summary

Since the first demonstrations of the ruby laser in 1960, lasers quickly found their way into different application areas. These applications range from the laser used in a CD-player via lasers used in surgery, to lasers that operate as a material processing tool. In this last area, the laser owes its success a great deal on its concentrated and contactless energy supply. It is for these reasons that the laser can be used for drilling when conventional techniques fail, as is the case for drilling holes in parts of gas turbine engines. Drilling these cooling holes is necessary because the gas from the combustion chamber flows along these parts thus exposing them to extremely high temperatures. Overheating these blades leads to damage. The desired cooling is comes from relatively cold air flowing through the drilled holes. For drilling these cooling holes, conventional drilling techniques fail for two reasons: the diameter of the holes is very small (± 1 mm) and the hard superalloy material the parts are made of. A promising alternative is therefore laser percussion drilling.

In laser percussion drilling multiple laser pulses are fired at the material. The drilling is achieved via two material removal mechanisms. Material is evaporated due to the laser energy and molten material is pushed out by the vaporization pressure, the so-called recoil pressure. First, the material is heated up by the laser energy. At some point the surface reaches the melting temperature. To achieve the phase change of the material, an extra amount of energy, the so-called latent heat of fusion, has to be supplied. The surface of the growing melt pool is constantly heated up further and eventually reaches vaporization temperature. From this moment on, the greater part of the incoming energy is used for the phase change to vapour. Because of this vaporization, the recoil pressure increases and, eventually, the molten material is pushed out. This effect is commonly referred to as the splashing mechanism. During this splashing the molten material flows along the relatively cold walls, partly resolidifying on its way. The vapour may have a second (negative) effect. Depending on the laser settings, a part of the incoming beam can be absorbed to such an extent that a plasma forms. This plasma, in turn, can shield the material completely. At this moment several drilling experiments are performed to improve the drilling technique. Rather than performing drilling experiments on the expensive superalloy the parts are made of one can use numerical simulations as a cheap and useful alternative.

In this thesis the physical phenomena playing a role in the drilling process are stud-

ied. Concluding from the time scales of the various processes, a subpulse behaviour can be expected. Multiple cycles of heating/splashing will occur during a pulse. The melting is studied extensively both analytically and numerically. Two mathematical formulations of phase change problems, also called Stefan problems, are discussed. The first formulation makes use of a boundary condition (the Stefan condition) to describe the evolution of the solid-liquid interface. The second is based on enthalpy formulation of the problem. These two methods are assessed numerically. A next essential part of this thesis treats the incoupling of energy into the material. This incoupling is described in terms of reflection. This reflection strongly depends upon both the laser, via its wavelength, and the irradiated material, via its index of refraction. In this thesis the reflection is dealt with using the Algebraic Ray Trace Method (ARTM). The importance of this phenomenon is illustrated by some examples. With the aid of both the melting model and the reflection model the influence of the settings of the laser beam is investigated. Both the spatial and the temporal pulse shape are assessed. Furthermore, a complete numerical simulation is presented.

The splashing and solidification is described mathematically and leading-order analytical systems are derived through asymptotic analysis. The numerics for the solidification model are studied extensively. Our study explains why local clumps of material may arise in the drilled hole during the laser percussion drilling process. Finally, NumLab, a computational platform on which all computations are carried out, is briefly described. The advantage of NumLab is lying in the fact that it uses existing and often well documented libraries. One merely needs to write an interface for each library translating the NumLab datatype to the library datatype and vice versa. This usage is illustrated by an example.

Samenvatting

Ondanks zijn prille bestaan, de eerste demonstraties van een laser vonden plaats in 1960, heeft de laser al snel zijn weg gevonden naar verschillende toepassingen in evenzovele toepassingsgebieden. Denk hierbij bijvoorbeeld aan de laser in CD-spelers, lasers die gebruikt worden om chirurgische operaties uit te voeren en de laser als materiaalbewerkingsgereedschap. De laser heeft zijn succes in dit laatste gebied, de materiaalbewerking (bijvoorbeeld lassen, harden en boren), voornamelijk te danken aan zijn geconcentreerde en contactloze energie-overdracht. Het is om deze reden dat de laser gebruikt kan worden om te boren als conventionele manieren het af laten weten, zoals bijvoorbeeld het geval is bij het boren van gaten in een rotorblad van een gasturbine. Het boren van gaten in deze bladen is nodig, omdat rotorbladen blootgesteld worden aan een zeer grote thermische belasting ten gevolge van de hitte van het gas uit de verbrandingskamer van de turbine. Dit leidt tot ongewenst hoge materiaalspanningen. De benodigde koeling wordt verkregen doordat de lucht die door de gaten stroomt een relatief lage temperatuur heeft. Bij het boren in de rotorbladen laten conventionele boortechnieken het afweten om twee redenen: enerzijds is de diameter van de gaten erg klein (± 1 millimeter) en anderzijds zijn de rotorbladen gemaakt van een (zeer harde) superlegering. Een veelbelovend alternatief voor bovengenoemde conventionele technieken is daarom het laser percussieboren.

Laser percussieboren is een boorproces waarbij meerdere laserschoten (pulsen) op het materiaal worden afgevuurd waardoor er een gat ontstaat. Dit gat ontstaat door twee factoren, te weten verdamping van het materiaal onder invloed van de laserstraling alsmede uitstoting van gesmolten materiaal onder invloed van de verdampingsdruk. In het begin van een puls wordt het materiaal opgewarmd, waardoor het op een gegeven moment de smelttemperatuur bereikt. Om de fase-overgang te bewerkstelligen moet een extra hoeveelheid energie, de zogenaamde latente warmte, worden toegevoegd. De toplaag van het aldus groeiende smeltbad wordt voortdurend verder verhit en bereikt daardoor op een gegeven moment de verdampings-temperatuur. Vanaf dit moment wordt een groot deel van de inkomende energie gebruikt voor de overgang naar de gasfase. Door de verdamping stijgt de druk aanzienlijk, waardoor uiteindelijk het smeltbad weg wordt geperst. Dit effect wordt wel het spatmechanisme genoemd. Tijdens dit spatten stroomt het gesmolten materiaal langs de relatief koude wanden naar buiten. Gedurende dit proces kan een gedeelte van dit materiaal weer stollen. De damp heeft nog een tweede (negatief)

effect: afhankelijk van de instellingen van de laser kan een deel van de inkomende laserstraal ook geabsorbeerd worden, hetgeen zelfs kan resulteren in het ontstaan van een plasma in de damp. Dit plasma kan dan op zijn beurt gaan werken als een scherm met als resultaat dat de energie van de laserstraal het materiaal niet bereikt. Op dit moment zijn verschillende boorexperimenten nodig om de bestaande boortechniek te verbeteren. Dit is een kostbare zaak omdat de superlegering waarvan het materiaal vervaardigd is erg duur is. Numerieke simulaties kunnen echter een goedkoop en vruchtbaar alternatief zijn.

In deze dissertatie zijn alle fysische fenomenen die een rol spelen tijdens het boorproces onder de loep genomen. Uit de tijdsschalen van de verschillende deelprocessen kan worden geconcludeerd dat er een subpulsgedrag kan worden verwacht. Meerdere cycli van smelten-spatten komen tijdens een puls voor. Het smelten wordt zowel wiskundig als numeriek uitvoerig bestudeerd. Zo worden twee mathematische voorstellingen van problemen met een fase-overgang, de zogenaamde Stefanproblemen, besproken. In de eerste wordt gebruik gemaakt van een randvoorwaarde (de Stefanconditie) om de positie van het scheidingsvlak tussen vast en vloeibaar te bepalen. De tweede behelst een enthalpie formulering van het probleem. Deze twee methoden worden naast elkaar gezet en numerieke oplossingsstrategieën worden afgeleid en gebruikt om tot resultaten te komen. Een volgend essentieel onderdeel van deze dissertatie behandelt de inkoppeling van laserenergie in het materiaal. Dit wordt beschreven in termen van reflectie. Deze reflectie is sterk afhankelijk van zowel de laser (via de golflengte) als het materiaal (via de brekingsindex). De modellering hiervan wordt gedaan aan de hand van de Algebraïsche Ray Trace Methode (ARTM). Het belang van deze laatstgenoemde studie wordt geïllustreerd aan de hand van enkele sprekende voorbeelden. Met behulp van het smeltmodel alsmede het reflectiemodel wordt vervolgens de invloed van de instellingen van de laserbundel onderzocht. Zowel de ruimtelijke als de tijdsafhankelijke vorm van de bundel komen aan bod. Ook wordt een volledige simulatie gepresenteerd.

Het spatten en stollen wordt wiskundig beschreven en hiervoor worden eerste orde vergelijkingen afgeleid. Het stolmodel wordt vervolgens ook numeriek verder uitgediept. Ons model levert daarmee een verklaring voor de experimenteel geobserveerde plaatselijke verdikkingen van de stollaag. Tenslotte wordt ingegaan op NumLab, een numeriek platform waarop alle benodigde berekeningen uitgevoerd worden. Het grote voordeel van NumLab is het feit dat zoveel mogelijk gebruik wordt gemaakt van bestaande en goed gedocumentarierde software. Dit wordt bereikt door een schil te schrijven rond elke bibliotheek die de bibliotheekeigen datatypen omzet naar NumLab datatypen en vice versa. Dit principe wordt geïllustreerd aan de hand van een voorbeeld.

Acknowledgements

The thesis that lies in front of you obviously is not only the work of myself. Many people have made contributions to it, and I would like to thank them in the following.

First, I would like to thank prof.dr. R.M.M. Mattheij for his advice on any subject discussed in this thesis and many, many more. And, maybe even more importantly, when things did not look too good, he was always positive.

Secondly, I owe many thanks to Eldim B.V. and Rolls Royce plc. for financially supporting this project. Furthermore, I would like to thank Martien van Dijk for the constant reality-check and for his help in writing the introductory chapter.

The preliminary versions of this work let much to be improved upon and I am grateful to prof.dr. M. Rumpf, prof.dr. H. van Duijn and dr.ir. A.A.F. van der Ven for their careful reading. This has led to great improvements of this thesis.

Special thanks also to dr.ir. Jos Jansen and dr. Warren Smith for their support during the first two years of my PhD, and to dr. Jos Maubach who has helped me intensively during the remainder of my PhD. Many thanks as well to dr.ir. Bas van der Linden for his help in implementing the reflectivity model.

Finally, I owe many thanks to Annemiek, my parents and everyone else in my personal surroundings for all the support and distraction they gave me.

C V R R I C V L V M V I T Æ

The author was born in Eindhoven, The Netherlands on September 2nd 1975. He completed his pre-university schooling at the Pius X College in Bladel in 1993 and started studying mathematics at the Eindhoven University of Technology in the same year. In the Master's phase of this education, Kees specialised in Scientific Computing. In 1998, he graduated cum laude. His master's thesis, written under the supervision of prof.dr. R.M.M. Mattheij, was titled *Modelling a laser percussion drilling process* and was a pilot study for the research that has led to this thesis. His master's thesis won the second Mignot prize in 1998. In August 1998 he started working as a PhD student in the Scientific Computing Group of prof.dr. R.M.M. Mattheij at the Eindhoven University of Technology. Since November 2002, Kees works as a consultant at Be Value.